Karlsruhe Institute of Technology

Finite element simulation of a highly water-saturated gas reservoir in northwestern Argentina to forecast its Geothermal potential

Finite-Elemente-Simulation eines hoch wassergesättigte Gas Reservoir im nordwestlichen Argentinien, um sein geothermisches Potenzial zu prognostizieren

Master Thesis
presented by

Emiliano R. Sosa Massaro

December 2017

Institute of Applied Geosciences
Department of Civil Engineering, Geo and Environmental Sciences
Karlsruhe Institute of Technology

First Supervisor: Prof. Dr. Thomas Kohl
Prof. Dr. Martin Gabi

Second Supervisor: Dr. Jörg Meixner
Dr. Silvia Barredo

I declare that I have authored this thesis independently, that I have not used other than the declared sources / resources, and that I have explicitly marked all material which has been quoted either literally or by content from the used sources.

Emiliano R. Sosa Massaro (Karlsruhe, February 9, 2018)

Contents

List of Figures

List of Tables

1 Abstract

A wide availability of in field Oil & Gas facilities which still have a marginal productive life can be a good opportunity to produce geothermal energy. The challenge is to make good decisions about the company's assets to include geothermal energy as a candidate in their project portfolio. The self-sustainability of this type of energy production must be ensured by accurate forecasts of the net-energy balance.
A geothermal energy production cycle must ensure the best selection of production and injection wells saving energy during their productive lives of the project.
A first approach to the simulation of geological faults,lithological heterogeneities of rocks and their interaction with the wells is the basis for the later detailed understanding of the geothermal water cycle.
Finite element simulation (FEM) it is a fast tool to understand how the key variables such as "injection and production flow rates", "well-to-well interference" and "well-to-reservoir heterogeneities interactions" can change the energy consumption needed for geothermal energy production. The role of the key parameters can be easily adjusted to make quick comparisons between different prospects before any detailed engineering is performed.
The simulation performed in this thesis has shown a geothermal harvest gain of 58%, when a combination of the more advantageous properties of the geothermal system were used, in comparison with the case represented by the less efficient properties combination.Thanks to the FEM simulation, a detailed interpretation of the peculiarities of production and temperature development shows that not always the more productive case is the most efficient one.
The present work presents a method to get a preliminar model of the energy production potential in a water-flooded hydrocarbon reservoir.

2 Introduction

2.1 Recent Oil and Gas Activities

The oil and gas industry is leaving behind a lot of infrastructure e information everywhere it had the commitment to develop different kinds of hydrocarbon reserves. From the exploratory drilling to the abandon of the well, many concepts try to maximize the profit margin of the wells. The risk assumed after the decision to drill a well with the objective to produce hydrocarbons, will not later allow managers to give the company's scientists and engineers the opportunity to study it as a prospect for geothermal uses. The human resources of the company have to moves fast trying to make profitable business.

Some small companies have not a large budget and they invest thinking on optimize the lifting cost. Marginal gas and oil fields are increasing in number day after day, in the same sense operating companies had to become more and more imaginative, in order to maximize the value of the asset they have.

In Argentina, the speeded up hydrocarbon production declination is in part because of lack of investment and in part because of the advanced stage of field maturity. In the last ten years, the investment has a clear target which is the Shale Gas, Shale Oil and the Gas Tight Sands in the productive Neuquina Basin. In mature Basins like Cuyana and San Jorge Gulf, meanwhile, exist lots of small companies who are concentrated on developing new concepts for mature fields. So, part of Neuquina basin, almost all Golfo San Jorge Basin, Austral Basin, and mostly all North-West Argentinian basins are marginal or near to became marginal gas and oil fields.

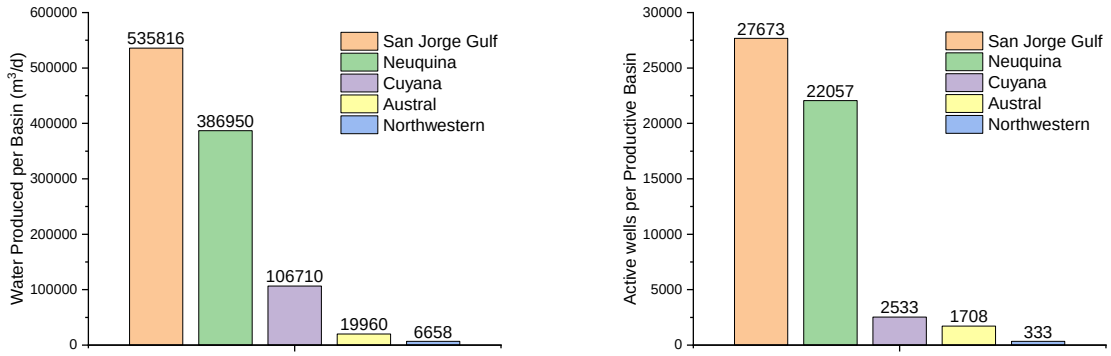

(a) Water production per productive basin in m^3/d

(b) Available wells per productive basin

Figure 1 – Argentinian available wells and water production per productive basin (MinEM, 2017)

The Macueta gas and condensate field is the southernmost tip of an elongated anticlinal structure which is parallel to the Andean Belt in the so-called Sub-Andean thrust and fold belt, which extends from northwest Argentina to southern Peru. These anticlines are the trap of a large amount of gas and condensate extensively explored and drilled.

In Figure 2, two typical gas production profiles of this basin. In Figure 2a this well has suffered a strong decrease in their production potential because of it large amount of liquid (water and condensate), thus pushing its productivity to depend on future workover interventions. On the other hand, in Fig. 2b, this well can continue producing even with a high water / gas ratio. With regard to the latter case, it can be expected that it becomes a productive water producer at the end of its productive life.

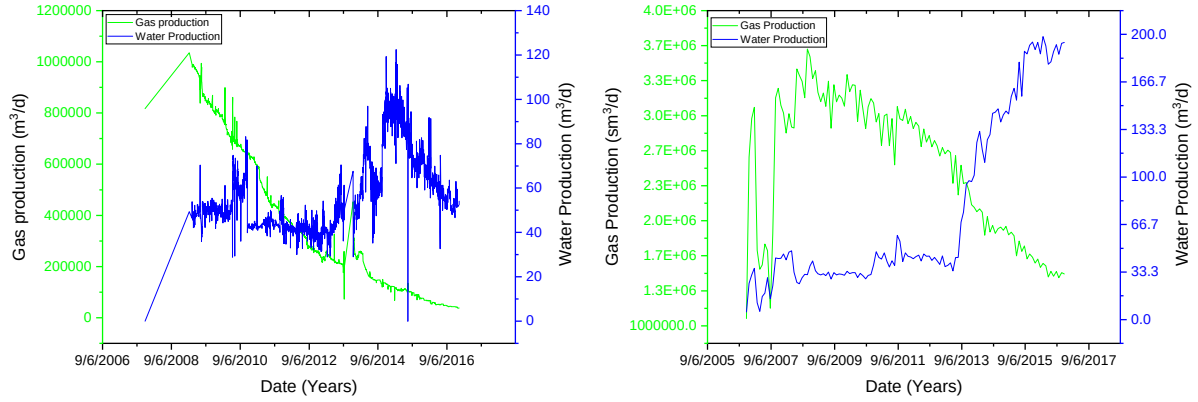

(a) Average production gas profile in Northwestern Basin.

(b) High capacity gas well in Northwetern Basin.

Figure 2 – Two different production profiles for gas wells in the Northwestern Basin (MinEM, 2017)

2.2 Geothermal Potential

The potential of geothermal production in Argentina lies partly in the places where oil and gas are produced.

Continental rift basin (Cuyana), compound rift-aulacogenic-foreland (Golfo de San Jorge), and the passive margin stage in Cretaceus ans Paleozoic Basins in Northwester Argentina, are the type of basins where Oil and gas activity is developed. Some of these basins in the western part of the country were built due to the recent Andean orogenesis. The most interesting geothermal volcanic systems are located on the Ring of Fire of the Andes. Convective hydrothermal systems depend on faults, and as well as conductive hydrothermal systems, these shares their placement with some hydrocarbon basins, as can be seen in Figure 3.

Main attention is given to high enthalpy projects linked to volcanism (Copahue, Domuyo, Tuzgle-Tocomar, Los Despoblados and Los Molles) or associated with geothermal anomalies (Rio Hondo). Low enthalpy convective and conductive systems associated with the hydrocarbon-producing basins are not part of the geothermal agenda of the Argentine private or public organism. On the other hand, non-hydrocarbon basins such as Chaco-Paranaense and Salado Basin (central and north-eastern Argentina) are active in hot water production for thermal baths and agricultural applications (Pesce, 2015).

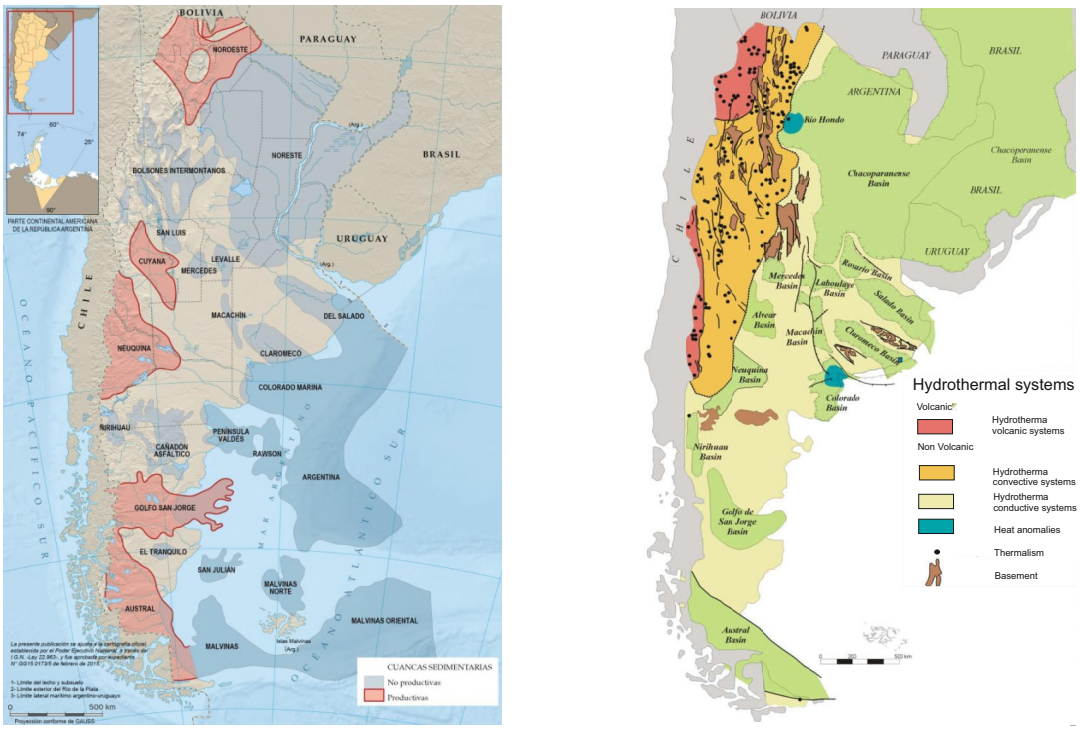

(a) Hydrocarbon productive basins map of Argentina

(b) Geothermal map of Argentina.

Figure 3 – Hydrocarbon exploitations and geothermal potential maps of Argentina. Modified from Secretaria de Energia y Mineria de la Argentina.

2.3 Motivation

Typically, Oil and Gas companies fights against the premature breakthrough of water into the production interval. When a second or third immiscible phase begins to flow to the completion of the well, productivity tends to decrease. Oil production usually involves a large amount of produced water that is later re-injected into the reservoir. On the contrary, gas production is heavily affected by the production of liquids. It's a big challenge to keep the production interval free of unwanted water.

The gas and condensate reservoirs in the Paleozoic fields in Northwestern Argentina are the deepest in their class. With an average true vertical depth of more than 5000 meters and wells with head temperatures that can reach 110 °C. Under the fact that water gets into the reservoir and floods it, I wonder myself if this gas and condensate reservoir can be candidates for their conversion into a middle-temperature geothermal reservoir. Since the wells were not drilled with the aim of being converted and disregarding the possibility of a re-completion, it becomes necessary to find a well production and injector pattern that maximizes the potential of geothermal production, and whether it is possible to identify the relative variations in energy consumption between the different patterns.

This thesis will attempt to develop a method to better understand the geothermal potential of the Macueta Field, which could later be replicated in other gas and oil fields. A quick and consistent assessment of the geothermal potential of the reservoir could help integrate geothermal production with the other existing projects into the company's business portfolio.

3 Geological Setting

3.1 Location

Acambuco Block is located in the northern area of the province of Salta in the Department of General San Martin. This block consists of two gas fields, Macueta and San Pedrito, located in the biosphere reserve Yungas Rainforest. The Macueta Field is in the binacionalborder with Bolivia. The location of the anticlinal containing the structural trap studied here is located in the Sierras de San Antonio, inside 21°57'28" and 22°10'0.2" South latitude and 63°59'56" and 63°49'59" West longitude. Landscape is very irregular, including stepped "v" shape valleys. This field is located at about 1100 m.a.s.l. Annual precipitation is around 1200 mm/yr. The average daily maximum temperature is about 29.9ºC, and the average daily minimum is 15.9° C Amengual (2009).

In a more general context, the Macueta field belongs to Sub-Andean thrust and fold belt, which is a narrow belt made of orographic meridian and subparallel anticlinal alignments. This is the eastern border of the Andes in northern Argentina and southern Bolivia. This part of the sub-Andean thrust and fold belt is located in the Tarija Basin (Figure 4). The Tarija Basin (According to the bolivian nomenclature) lies between 18°30' and 23°30' south latitude, between eastern Cordillera (west) and Chaco Plain to the east. The area is divided into different regions according to the effect of the thrust on the overlying layers to the main decollement (Starck et al., 2002). The present thesis focuses on the southern Sub-Andean Zone and the South Chaco Plain Zone.

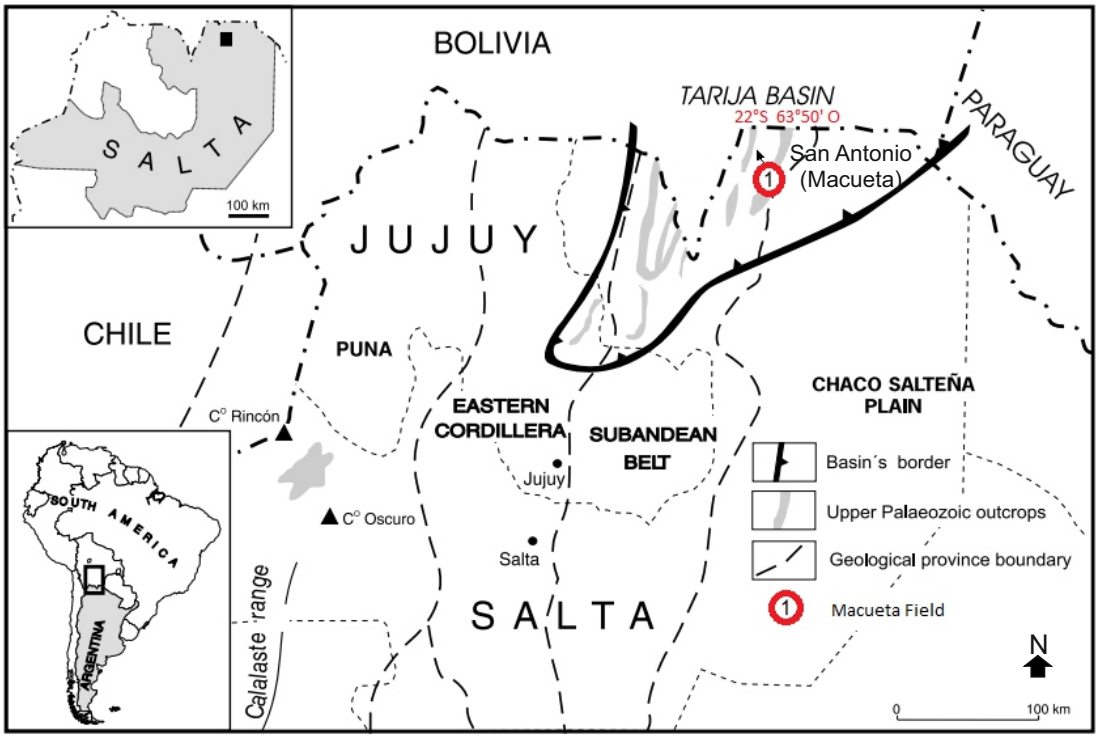

Figure 4 – North Argentinean and South Bolivian map. Macueta Field location Modified from Di Pasquo (2002)

In Figure 4, Point 1 (in red) indicates the position of the Macueta field in the Tarija Basin, which is located in between the southern Sub-Andean Zone and the Chaco Plain border.

3.2 Tectonic framework

The Andean range started to be uplifted in late Cenozoic times (Gonzalez, 1950) but the main deFormational stage took place during the Upper Miocene (Ramos, 2009). Marshall and Sempere (1991) claim that the development of the Neogene foreland started during the Late Oligocene (27 My ago) when the deFormation front began to migrate eastward from the current Altiplano position. This episode is linked to a horizontalization process (Isaac, 1988), which was followed by an increase of the tilt of the Nazca´s Plate, which is subducting below the Sudamericana Plate. This phenomenon has induced the development of the lower crust delamination, which had been responsible for the strong orogenic shortening and the notorious development of the structures structures created in the Sub-Andean Zone.
Today, this folded and thrust belt has a shortening rate of about 8 mm/year (Hernandez et al., 2002); and the deFormation boundary is located at the east of Campo Durán, which is almost the easternmost well-developed anticline. The actual deFormation front can be located at a distance of 750 km from the trench. This could be due to the high age of the subducted oceanic crust at this latitude, assuming that this cold crust can easily transmit the thrust, allowing an increase of the shortening strengths in the orthogonal direction. The present foreland basin, in connection with the folded and thrust belt, can be placed in the easternmost position. This is characterized by Cenozoic deposits, which reaches a thickness of about 4000 m at the foot of the Sierra de Agueragüe 20 km to the east of Macueta Field. (Moretti et al., 2002).

3.3 Structural geology framework

From the structural point of view, the sub-Andean zone is defined as the frontal zone of the thin-skinned fold-and-thrust belt Rodgers (1971), which is composed of folds and shiftings with east vergence Ramos (1999). This configuration has a Silurian basal décollement, located in Kirusillas Formation. Furthermore, a second décollement level into the Devonian Los Monos Formation, it has been proposed by Kley et al. (1999).

According to Moretti et al. (2002) the position and extent of the various décollement levels, can explain the shortening of the southern sub-Andean Zone in the range of 60–90 km (Figure 5). Nowadays, in the same place, a cross section ranges in about 85 Km.
The main decollement level in the Macueta field is located in the Silurian shales, a second decollement occurs in the Middle Devonian (Los Monos Formation). Another small decollement could be expected in the Carboniferous diamictites. The switching from one decollement level to the other may be due to lateral facies variations (especially in the Devonian) and/or change of the shale thickness. In the easternmost outcrops of the Los Monos Formation duplexes were identified. Cumulated thickness of these shales in anticline positions can reach up to 2000 m, three times their initial thickness (e.g. Camiri, San Antonio, San Alberto (Macueta)) (Starck et al., 2002). The western portion of Los Monos Formation becomes sandier and does not act

as a decollement level (Moretti et al., 2002). Some small inverse faults related to detachment levels in the Middle Devonian or Carboniferous shales may affect the hinge of the anticlines (e.g. Camiri, Aguarague, San Antonio, and also possible in San Alberto (Macueta)) Moretti et al. (2002) suggest that this young and shallow faulting is late and superficial.
In Figure 5 a cross section and palinspastic reconstruction at the level of Villamontes 80 km in direction to the north of Macueta field, into the same positive structure, is sketched.

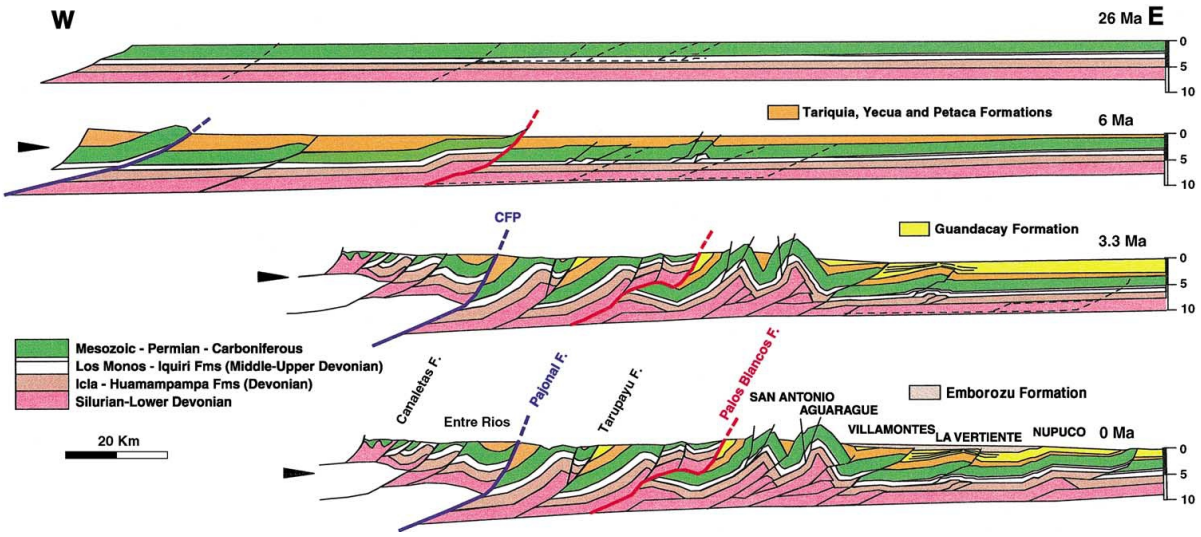

Figure 5 – Cross section and palinspastic reconstruction near to Macueta field. Modified from Moretti et al. (1996) and Colletta et al. (1999)

3.4 Stratigraphy

The stratigraphical sequence extracted here will help to better understand the stratigraphy of the geothermal system. For a more comprehensive description reader may refer Starck et al. (2002).

Porongal (Santa Rosa) Formation

The (Porongal) Santa Rosa Formation switches gradually to the Baritú Formation. The rocks of this Formation are correlated with the Santa Rosa Formation in Bolivia, which is an important reservoir rock. This unit comprises quarcites, conglomeratic sandstones and oligomictic conglomerates. This conglomeratic facies shows evidence of a fan-delta environment, where sediments had been redistributed by the waves, tides and marine currents (Vistalli, 1999). The palynologic analysis permitted to establishing the Lokovian age to the Formation (Suarez Soruco and Diaz Martinez (1996), Diaz Martinez (1996)).

Las Pavas Sequence

This sequence reaches the early to the middle Devonian is composed of the Icla and Huamampampa Formation (Starck, 1995). This pile is limited on the upper and lower part by flooding surfaces, which are coincident respectively with the bases of Icla and Los Monos Formations.

The thickness of this Formations are 800 to 900 meters and internally has a grain and strata coarsening upward, which corresponds to the depositional sedimentary sequence, controlled by the proximal porgradational facies over the distal facies. (Starck et al., 1992).

Icla Formation

It is placed concordantly over the Porongal Formation. It has a thickness of around 500 meters and is composed of primarily by massive black mudstones, which locally presents high content of organic matter ((Suarez Soruco and Diaz Martinez, 1996), (Diaz Martinez, 1996)). Inside this shaly packet it is possible to recognize quartzitic sandstone bodies and not well developed silicified sandstones (Luquez et al., 2002). The deposits of the base of this unit correspond to the distal platform environment, that upwards it changes to a proximal platform environment (Vistalli, 1999). The mudstone level has a high content of brachiopods, crinoids, and trilobites like Scaphiocoelia bolivensis, australostrophia clarkei and australostrophia hawkinsi. The fossil content allowed to assign this Formation to an inferior Siegenian-Emisian age (Suarez Soruco and Diaz Martinez (1996), Diaz Martinez (1996)).

Huamampampa Formation

This Formation was originally characterized by Ulrich (see reference in (Suarez Soruco and Diaz Martinez, 1996) and (Diaz Martinez, 1996)),. it is composed of well-defined interfinguering of quartzite and limolite layers, which overlie conformable the Icla deposits (Luquez et al., 2002), and reaches a maximum thickness of 600 meters. This unit comprises depositional sequences. The lower part correspond to a distal platform environment, which grades progressively upward to a proximal platform. The cross stratified sandstones located in the upper part corresponds to a coastal environment; the upper part of the sequence corresponds to a continental to a mixed environment (Luquez et al., 2002). This unit has an Emsian age because palynologic data suggest that fossil content is scarce (Suarez Soruco and Diaz Martinez (1996), Diaz Martinez (1996)).

Supersequence Aguaragüe

This sequences was deposited from the middle to the superior Devonian and include the deposits of Los Monos and Iquiri formations. The higher development of this Formation occurs in the Bolivian side (Diaz Martinez, 1996). Their inferior limit is a flooding surface, and the deposits which composed of it are characteristic of a distal platform environment, that grades progressively upward to a proximal platform and a coastal shore (Vistalli, 1999). In the zones where this pile reaches the maximum development has a thickness of around 1000 meters. Nevertheless this unit was affected by pre-carboniferous unconformity, and thus it can be much thinner or even disappear (Starck et al., 2002).

Los Monos Formation

This Formation overlays Huamampampa concordantly and has thicknesses of around 600 meters (Luquez et al., 2002). It is composed of by black shales which correspond to a distal platform environment and moreover present slim sandstone intercalation, corresponding to sporadic storm events, which are more frequent in direction of the Formation top (Starck et al., 2002). The presence of fossils like Nuculites sp, Australocoelia sp, Tentaculites sp, and Braquispirifer audaculus allows assigning this unit to the Eifelian-Givetian age (Inigo et al., 2012).

<table>
<tr><td></td><td></td><td>BASEMENT</td><td>GROUP OR SUPERSEQ.</td><td colspan="2">FORMATION</td><td>LITHOLOGY</td></tr>
<tr><td></td><td></td><td></td><td></td><td>Bolivia</td><td>Argentina</td><td></td></tr>
<tr><td rowspan="5">Paleozoic</td><td rowspan="5">Devonian</td><td>Givetian</td><td rowspan="2">Agueragüe Supersequence</td><td rowspan="2">Los Monos</td><td rowspan="2">Los Monos</td><td rowspan="2">Black mudstone belonging to a distal platform environment, fine sandy interbeds associated with storm events.</td></tr>
<tr><td>Eifelian</td></tr>
<tr><td>Emisian</td><td rowspan="3">Las Pavas Supersequence</td><td>Humampampa</td><td>Humampampa</td><td>Well defined intercalations of clean sand with siltstone bodies.</td></tr>
<tr><td>Siegenian</td><td>Icla</td><td>Icla</td><td>Black shale with a high content of organic material and sandy bodies of clean sand with silica cement but in less proportion.</td></tr>
<tr><td>Lokovian</td><td>Cinco Picachos Supersequence</td><td>Santa Rosa</td><td>Porongal</td><td>Quartzite, sandy conglomerate, and polymictic conglomerates</td></tr>
</table>

Figure 6 – Stratigraphic column of Los Monos, Huamampampa, Icla and (Santa Rosa) Porongal formations.

4 Reservoir characterization

4.1 Petrophysical properties

Los Monos Formation

Los Monos Formation, in the Macueta field, is a highly folded anticline, with a thickness in its axis of about 2500m. In Appendix A the well-log of the SAL-x10 (San Alberto) is presented. This well is located 7 km to the north of the Macueta field. In this well-log the transition from the Los Monos Formation (siltstone) to Huamampampa Formation (matrix supported sandstone) is indicated by the gamma ray (GR) response. The induction log confirms the absence of permeability in Los Monos Formation. The superposition of the resistive curves indicates a low penetration of the fluid during the drilling phase.

Huamampampa and Icla Formation

The most important reservoir rocks are located in the lower Devonian. Huamampampa Formation consists of an alternating sanstones and silstones. In the sandy part, fine to very fine sandstone was deposited in a marine platform environment Disalvo (1999). This reservoir can be divided into several sections: Huamampampa 1 (“Dirty”), Huamampampa 2B (“clean”), Huamampampa 3, and Huamampampa 4. The maximum thickness is located in the northern part of Macuenta, southern San Alberto (500 m thick). About 50% can be considered net pay.
The Icla Formation is a shaley unit with major sandstone participation at the intermediate level. In their 70 m thickness, high fracture makes of this rock a good reservoir.

Porongal (Santa Rosa) Formation

The Santa Rosa Formation consists of a fine to medium grained sandstone. This sandstone would been deposited in a tide dominated delta environment. In the studied area, this formation averages 400 m in thickness, of which 230 m could be expected to correspond to proven productive units.
The upper part of this unit constitutes the sealeant basement of the Huamampampa and Icla reservoir interval. For a more detailed reservoir description reader can refer to Disalvo (1999).

Reservoir porosity - Near fault petrophysical properties

Properties close to the faults were measured by Moretti et al. (2002). Thin-section images confirm the variety of visual porosity in the Devonian samples which depends on its relative position respect to the faults. This measurements were complemented by mercury injection permeability measurements. Measurements show that the porosity decreases with the depth, from more than 20% in the Tertiary and Mesozoic formations to less than 2% in the Lower Devonian Huamampampa Formation. (Figure 7) to the right, show the petrographic characteristics of the rocks taken close to two different faults (faults from the hanging wall). At the left their corresponding mercury injection porosity measurements.

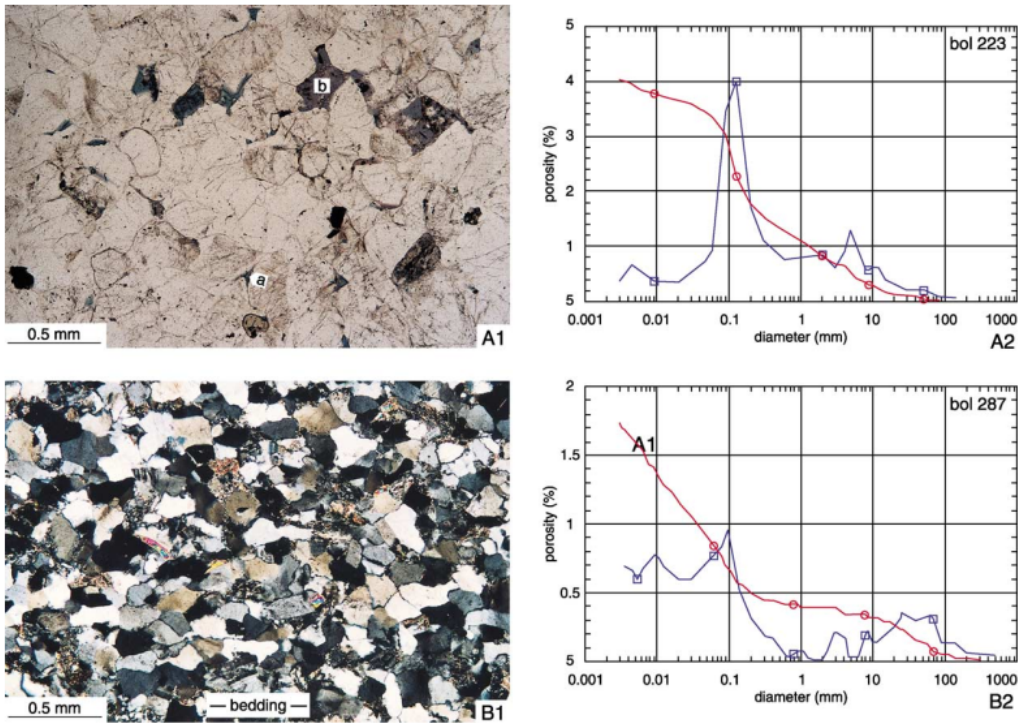

Figure 7 – Thin-sections corresponding to faulted zones inside the reservoir interval (San Alberto field_Bolivia)(Rebay et al., 2001)

Moretti et al. (2002) have reported porosities of about $< 5\%$ in the reservoir interval. Figures in Figure 7 belongs to the mentioned work. In the upper-right image the injection curve (in red) shows the cumulated connected porosity (4%), and the derived curve (in blue) gives the diameters of access thresholds to pores, with a main diameter of access threshold between 0.1 and 0.2 A (highest peak) and minor ones of higher and lower diameters (small peaks). In the image below, for the Lower Devonian Huamampampa Formation porosity cannot be seen. A cumulated connected porosity of 1.7% was measured, and the main diameters of access threshold between 0.01 and 0.1 A, and also minor ones between 1 and 60 A.
Other autors also suggest that matrix porosity ranges from 1% to 4% at the Huamampampa and Icla reservoir depth. Thin-sections of drilled cores shows micro and mesofractures created by diastrofism (Girardi et al., 2002). This porosity and the intergranular moldic porosity constitutes the 90 % of the total porosity. Big scale fractures represents 10% of the total porosity (Rebay et al., 2001).

Definition of naturally fractured systems.

A characterization of the fracture system in San Pedrito and Macueta fields was performed by Cohen (2002).
The Devonian reservoirs are Naturally Fractured Reservoirs, NFR. Those reservoirs hold natural fractures which significative influence their dynamic behavior (augmented permeability) Cohen (2002).

Fracture definition, clasification and flow characteristics.

Fractures can be defined as discontinuity surfaces, where rocks or minerals have lost cohesion. Generally the relative displacement between two adjacent points of originally adjacent points is small compared to their length. The term joint is used to define fractures that exhibit small displacement perpendicular to their surfaces.

Acoustic image log interpretation, core data, and field studies have evidenced the presence of Type I and Type II fold-related fractures in Macueta field. Production logs show Type I i.e. E-W fractures whose productivity is bigger than Type II, which are N-S oriented. A Type III also can be included at 45° with respect to the elongation of the structure, which is not also easily distinguishable into the others groups. A conceptual model was presented by Iñigo (2009) in Figure 8.

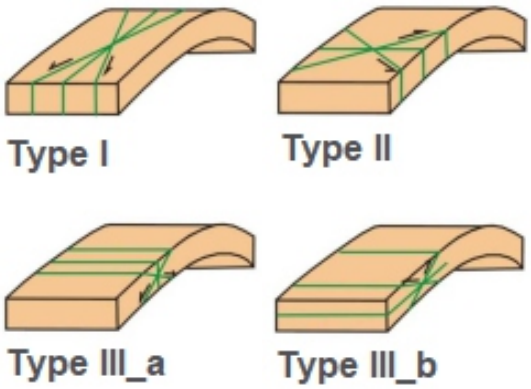

Figure 8 – Clasification of fractures based on Sterns (1968). Adapted from Copules et. al. (1998), taken from Iñigo (2009).

The existence of N-S breakouts and E-W induced fractures in the image logs suggest that the maximum horizontal stress (SH) is oriented E-W. This fact controls the productivity of the fractures. Therefore, those wells which are oriented perpendicular to SH should be more productive than the ones which are parallel to the SH.
Cohen (2002) proposed that in Macueta field, in flank positions, only E-W fractures would be productive, while in crestal positions N-S fractures would be also additionally productive due to an increase in intensity and curvature.
In the same work, Cohen proposed that the main mechanism of folding is flexural slip along bedding planes. In this context, N-S joints are associated to fold bending faults, as well as, the fractures E-W are related to shear faults.
Two Production Log Test (PLT) were run while the testing of Huamampampa and one Icla Formation A correlation between flowrate, fracture density and orientation was performed. A good correlation between the fracture intensity observed on image logs, gas flow spinner response and gas flow cooling was observed. Higher flow rates correlate with high density E-W type I fractures, while lower flow rates correlate with high density N-S fracture (Girardi et al., 2002). The confirmation of the above mentioned fracture orientation was finally observed in the failure of former horizontal well drilled in Macueta field. In Mac.x-1002 an horizontal side

track was performed in Huamampampa Formation This side track was designed with an azimuth of 110°, perpendicular to the axis of the structure, trying to reach the crest along the shortest distance. After drilling, a DST was performed and flow rate was much lower than expected. As a result, most of the intersected N-S fractures seen in the image log of this borehole were low productive.

4.2 Fault characterization

Fault zone definition

Macroscopically, faulted zones are defined by the high concentration of fractures observed around the fault planes, relative to the low fracture density of their background. Fault zone thicknesses vary from a few meters to tens of meters thick, without any clear relationship with fault offset. Sandstone is the most frequent lithology involved in fault zones but shaly intervals may be present, in particular in those faults where meter-thick horizons of alternating shales and sandstones form a hanging wall basal detachment level (Girardi et al., 2002).

Fault flow characteristics

Faults play a major role on the migration pathways in the Sub-Andean Zone. The hydraulic behavior of faults changes with depth in relation with sandstone diagenesis. Moretti et al. (2002) had proved from microstructural analyses of fault zones, that the main controlling factor was temperature, which facilitates or inhibits quartz precipitation. This result implies that the same fault is a barrier for lateral and transversal migration at depths $>$ 3 km, due to the sealing of fractures by authigenic quartz at T$>$80 ℃, but the same fault constitutes a lateral drain at shallower depths (Figure 9). A complete study of fault behavior in the Sub-Andean Zone was made by Husson and Moretti (2002).

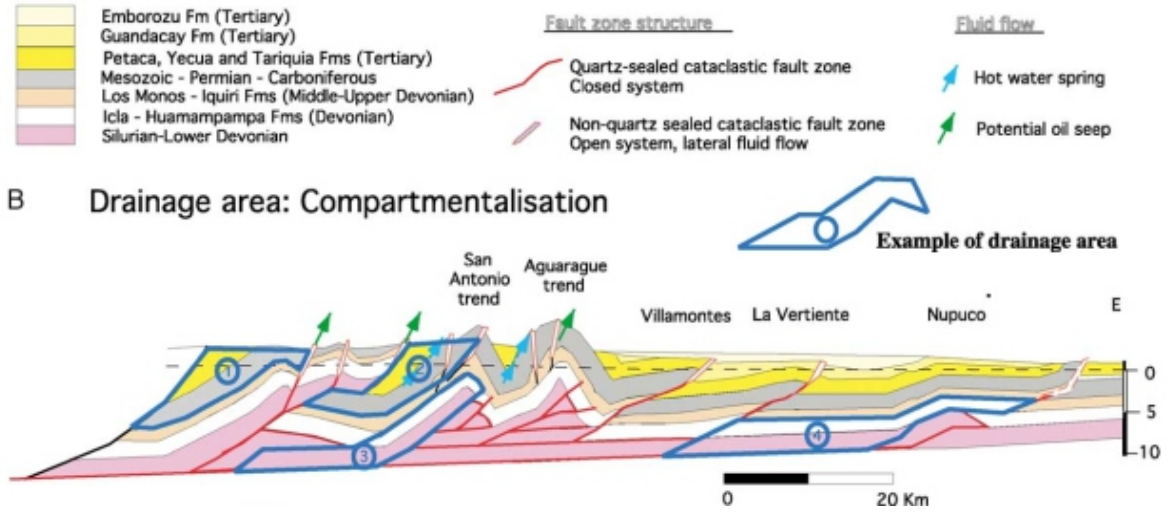

Figure 9 – Compartmentalisation of fluid flow by faults and low permeability stratigraphic intervals (Los Monos Formation), resulting in small drainage area of the structures. Taken from Moretti et al. (2002)

4.3 Thermal regime

The thermal regime has been measured in south sub-Andean wells by Moretti et al. (2002). They have identified thermal gradients in the Macueta region which comprehends The Macueta field. In Figure 10 the South Sub Andean zone (SSAZ) foothills and South Sub Andean zone (SSAZ) Llanura are indicated. The data was collected from different well locations, which normally are anticlines. Red star in Figure 10 indicates measured heat flux density value in San Alberto field (Foothills). The green star is the thermal regime in the Llanura region.

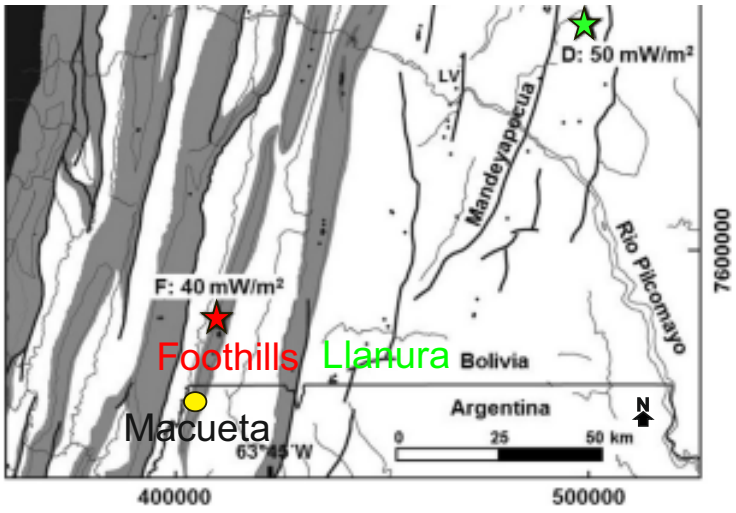

Figure 10 – Thermal regime in the south sub-Andean zone. Modified from Husson and Moretti (2002).

The South-SAZ foothills

In South-SAZ foothills (where San Alberto/Macueta anticline is located) the thermal gradient varies from 19 to 27 ℃/km and has 23 ℃/km in average (Figure 11).
The warmer values correspond to the measurements of eroded anticlines near the surface. In the hinges of some anticlines, the Los Monos Formation has been shortened in a disharmonic way and now achieves an apparent thickness of up to 2000 m whereas the stratigraphic thickness would not be more than 700 m. This is the case of the San Alberto anticline Moretti et al. (2002). Inside this region a difference of the computed gradient was observed. In southern foothills thermal gradient is 20 ℃/km, lower than the value calculated in the north. It fits with a basal heat flow (at the bottom of the Silurian) of about 40 mW/m^2, whereas a basal heat flow of 50 mW/mm^2 was compatible with data from almost all other wells in the north of the south SAZ foothills.

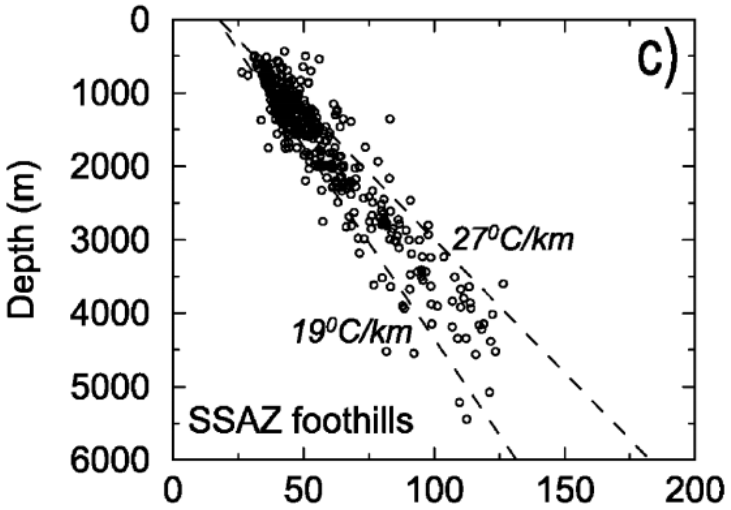

Figure 11 – Thermal gradient profile along the S-SAZ Foothills. From Husson and Moretti (2002).

The South-SAZ Llanura

Figure 12 shows the thermal gradient profile in Tertiary deposits in the eastern position with respect to the Macueta field. The mean values for the gradient range from 21 to 27 ℃/km (average is 25℃/km). The best fit in this case is found with a basal heat flow of 55 mW/mm^2.

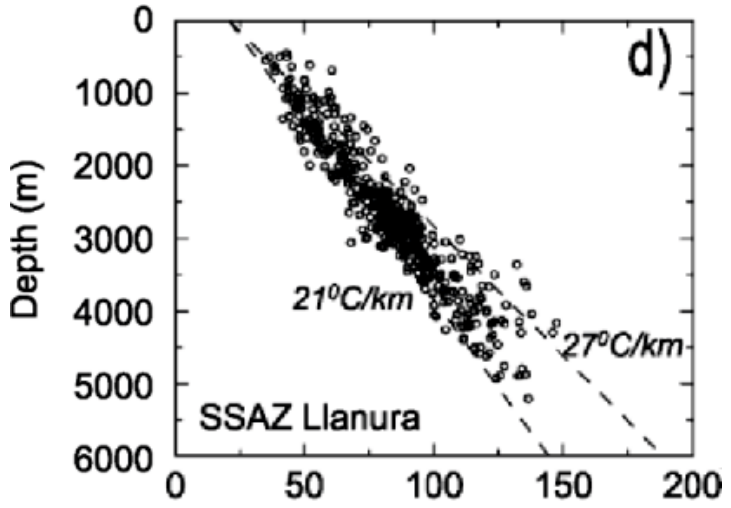

Figure 12 – Thermal gradient profile along the S-SAZ Llanura. From Husson and Moretti (2002).

5 Geological Modelling

5.1 Existing models

Macueta Model _ Argentinian side

Pan American Energy (PAE) is the concessionary of the Acambuco block that includes the Macueta Field. This block started their exploitation in 1982. Five wells were drilled, Mac.x-1001, Mac.x-1002 (original and re-entry), Mac.x-1001 bis(two sidetracks), Mac.e-1003, Mac-1006 and Mac-1004. The Mac-1004 has a dual completion over Huamampampa and Icla Formation. Three wells navigated with a high angle into reservoir intervals to take advantage of the heterogeneities given the best flux capacity of types I and II fractures.

From the Argentinian model the following elements were taken into account.

- Well production histories.
- Pressure, Volume, Temperature fluid behaviour data (PVT).
- Build Up well test data.
- Digital surface of the ”Transition Zone” between Huamampampa and Los Monos Fm.
- Well Tops.
- Well Correlations.
- Directional drilling surveys
- Well Mud and Petrophisical Logs.

Interpreted well log

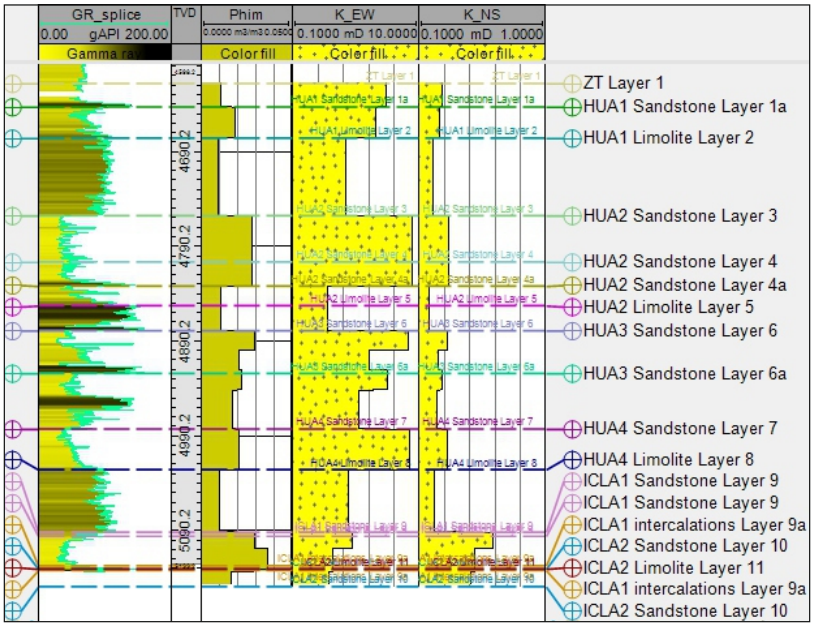

Figure 13 – Rock typing of Mac.x-1001 bis. K−NS and K−EW were described.

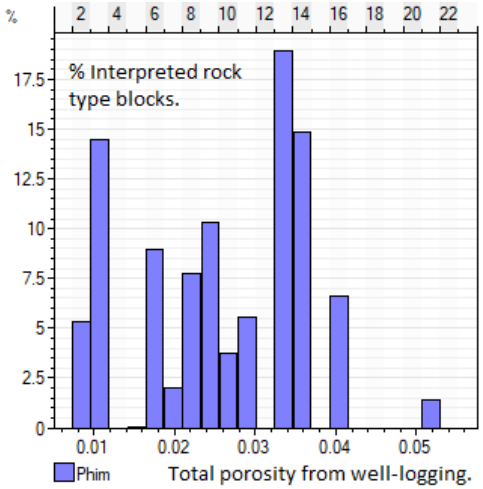

Figure 14 – Averaged porosity values (mixture of matrix and fractures) from Figure 13.

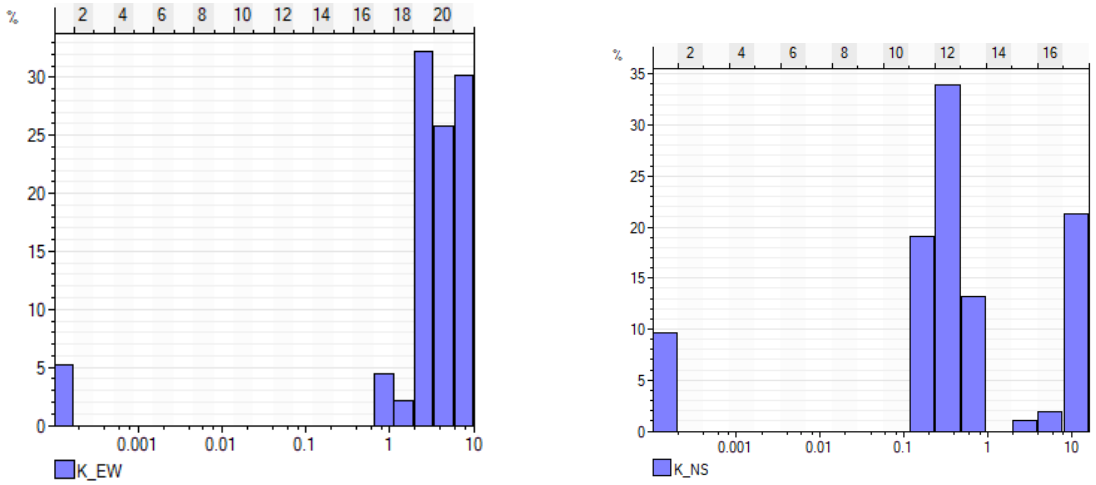

(a) Averaged East to West absolute permeabilities

(b) Averaged North to South absolute permeabilities.

Figure 15 – Bulk permeability (matrix and fractures) from Figure 13.

San Alberto Model _ Bolivian side

The structural model of San Alberto field in exploitation by ”Yacimientos Petrolíferos Fiscales Bolivianos” (YPFB) since 1992 was consulted.
From this model special attention was payed to the ”Small Fault” existence located at the hinge of the anticline. The name ”Small Fault” was given here to the mentioned fault to distinguish it to the others.
From the Bolivian model the following elements were taken into account.

- Water/Gas Contact depth location.
- Petrophysical properties: porosity and permeability of the bulk rock measured in laboratory.

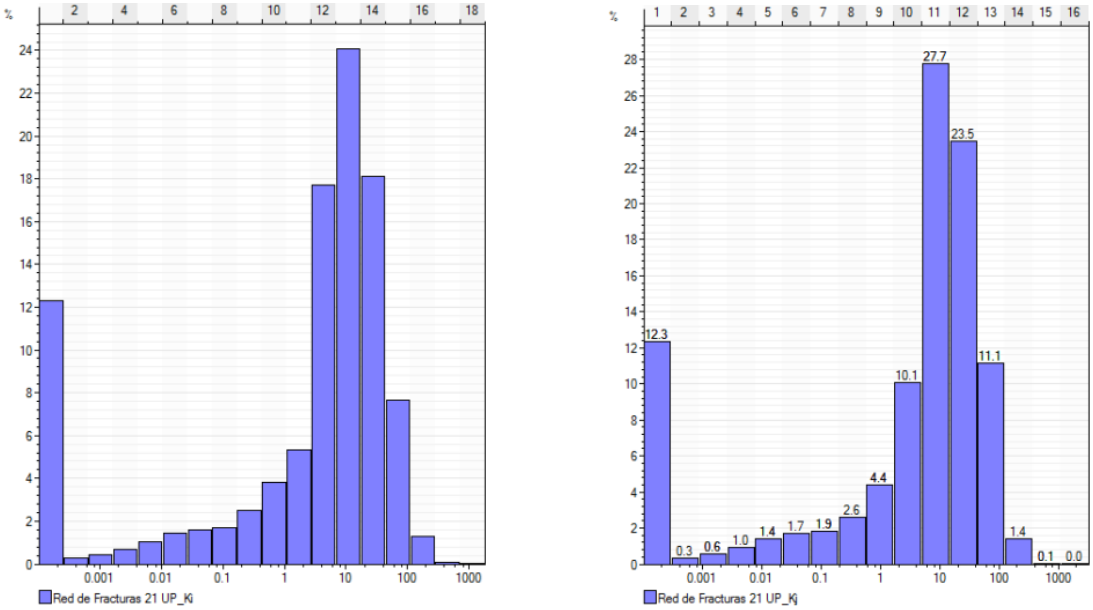

(a) Absolute permeability of oriented plugs i direction.

(b) Absolute permeability of oriented plugs j direction.

Figure 16 – Absolute permeability measured in plugs taken from oriented cores (San Alberto field). (Huanca Pongo et al., 2017).

5.2 Model set-up

The structural model in Petrel started from the digital surface called ”Transition Zone” (ZT - Layer 1), which was described by the exploratory team of PAE. This digital surface was the seed to later assemble the model. Afterwards, well-tops formation were used to set-up the offset in between the formations.
The main elements of the structure are listed as follows.

1. Faults (Refences in Fig 18)
    - Acheral-Fault: A fault propagation fold that crosses over the entire model.
    - Fault-1: It is a big fault parallel to Acheral fault, which accommodates the shortening after the folding. This structure cuts and disconnects the eastern flank of the anticlinal.
    - Small-Fault: This is a antithetic fault which intercepts the reservoir interval in the hinge of the structure. This fault accommodates the needed shortening to stand the thrust, and it can be followed from the San Alberto Field model in the direction to the south, despite the repetition of formations, as an indicator, cannot be assured.

2. Formations

Top	Base	Rock Type	Unit
4643	4672	Dirty Sandstone	H1
4672	4758	Dirty Sandstone	H1
4758	4850	Clean Sandstone	H2
4850	4879	Shale	H2
4879	4892	Clean Sandstone	H3
4892	4948	Dirty Sandstone	H3
4948	4964	Shale	H3
4964	4985	Dirty Sandstone	H4
4985	5022	Clean Sandstone	H4
5022	5062	Dirty Sandstone	I1
5062	5095	Shale	I1
5095	5129	Clean Sandstone	I2

Table 1 – list of the modeled formation layers in TVD _ X: 4406306 m Y: 7566896 m.

Table 1 is the result of the new geological model adapted for this study. Later, this separate Rock Type have been merged in a unique reservoir interval. Los Monos Fm. is the Cap Rock of the system and Top Santa Rosa is the basement. The first part of Santa Rosa Fm. hydraulically disconnects the two reservoirs Huamampampa+Icla from the Santa Rosa sandstones.

1. Wells

Well	Pseud.	Top	Base	Formation	TD	TVD
Mac.x-1001 bis	Well A	4674.42	5350.72	Hua+Icla	5524	5147.13
Mac.x-1002	1002	4649.66	4880.33	Hua	4975	4845.68
Mac.e-1003	Well C	4661.66	4885.66	Hua	5080	5047.03
Mac-1004	Well B	N/A	N/A	Hua+Icla	5173	4764.53
Mac-1006	1006	N/A	N/A	Hua+Icla	5430	4716.76

Table 2 – List of drilled wells in Macueta field (North).

Well-completions were made over Huamampampa and in other cases Huamampampa together with Icla Fm. From this point the wells named with Pseud. in Table 2 will be used for the simulation cases.

The resulting model made in Petrel can be seen in Figure 17. In Figure 18 a close look of the inner parts of the structure. Figures 19a and 19b shows the location of Well A (Mac-x.1001(bis)) with respect to the reservoir intervals and the location of the Small-Fault.

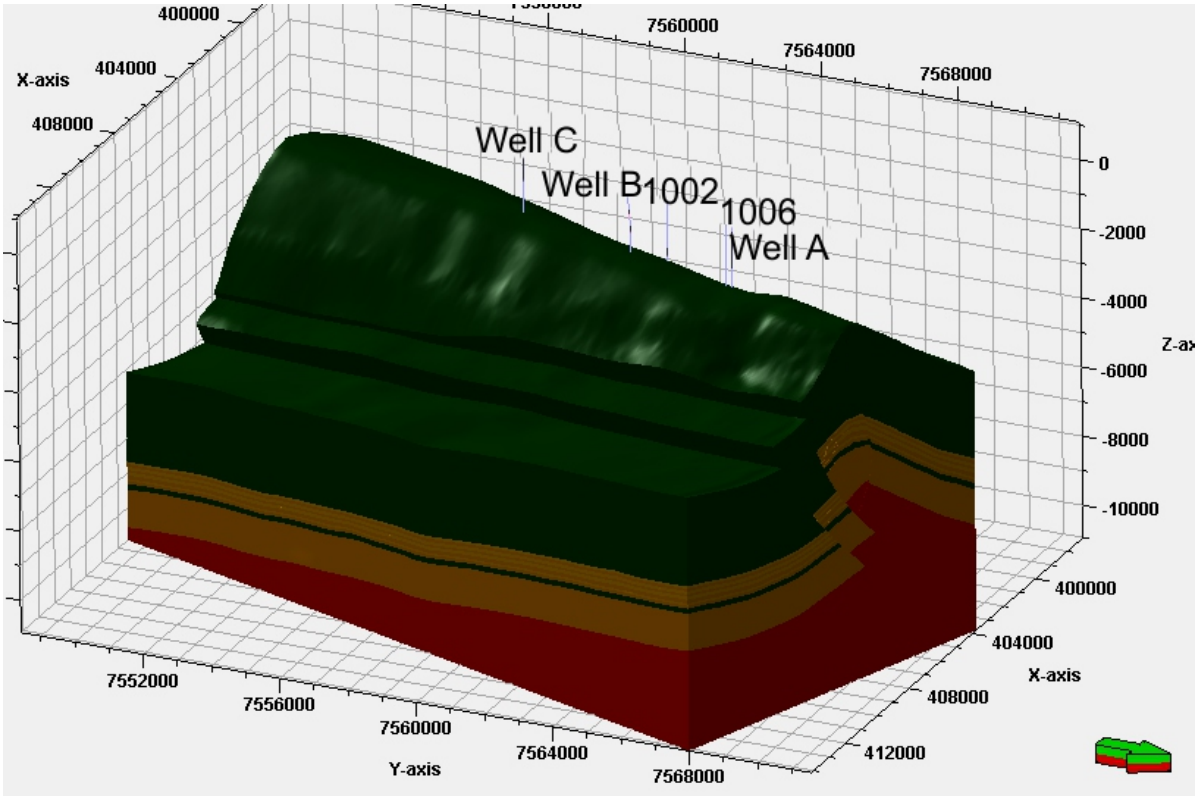

Figure 17 – Final geological model in Petrel.

There is an approximate alignment of the structure axis with the South-North direction. The five existing wells in the block are plotted here. The structure dips southwards.

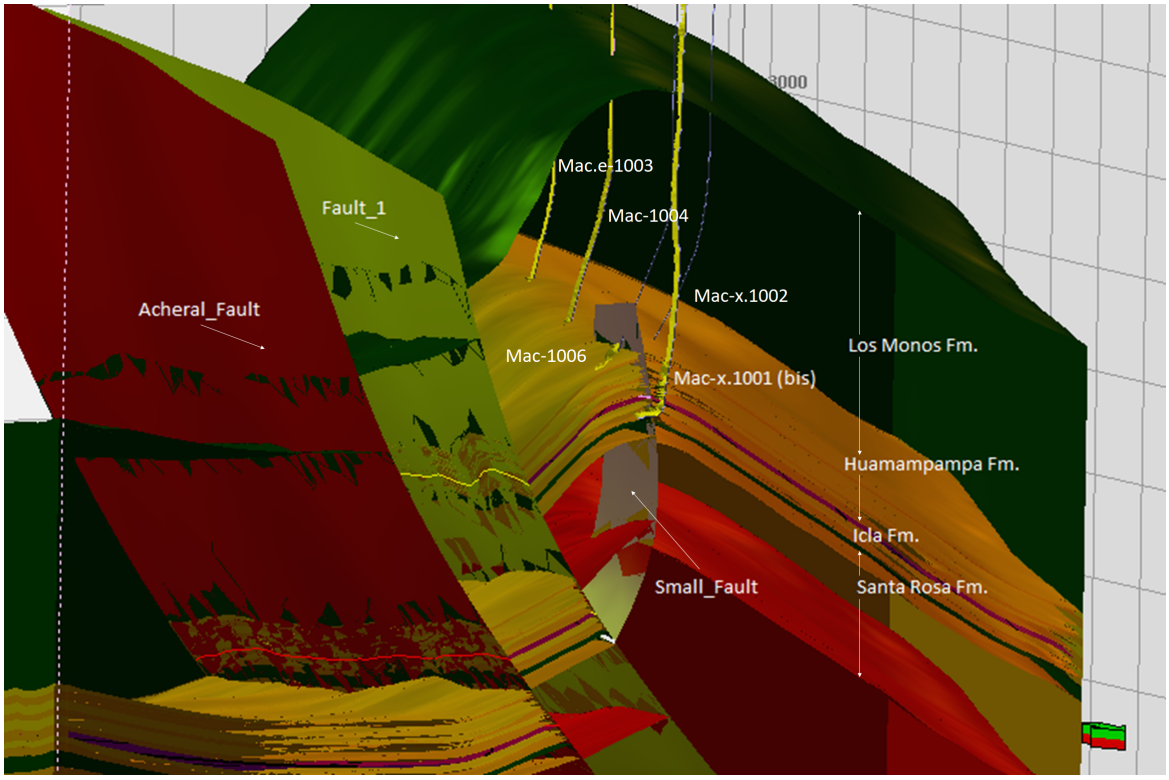

Figure 18 – Internal components of the Petrel's model viewed from the north.

Major faults affect the reservoir interval. The Small Fault, corresponds to an interpretation made by geoscientists of the San Alberto Field, and is supported by a 3D seismic Navia Vargas (2017). This fault has been proposed because of the behaviour of the Well A, which is a high-prolific gas producer in comparison with the rest of the wells in the same block.

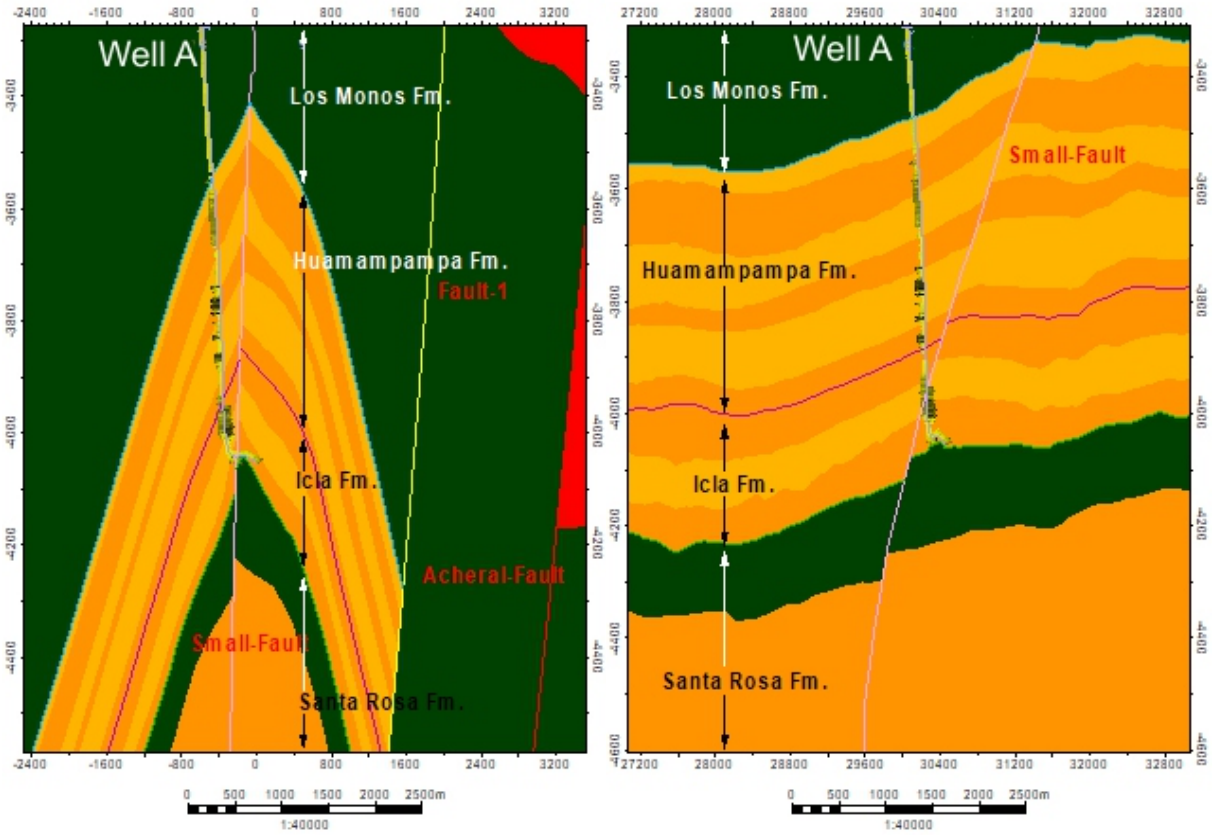

(a) Cross section of the Macueta anticline in the vicinity of Mac.x-1001. South to North vision.

(b) Cross section of the Macueta anticline in the vicinity of Mac.x-1001. East to West vision.

Figure 19 – In Fig 19a and Fig 19b are depicted the cross section of the model showing the relative position of the Small Fault and the Well A.

Porosities and permeabilities for the finite elements model

A unique reservoir block will be considered with a homogeneous distribution of the properties. The permeability of the reservoir and the Small Fault will be found later iteratively during the calibration stage.

Matrix	K [mD]			Phi [%]
	x	y	z	
	6	2,4	6	4

Fracture	K [mD]			Phi [%]
	x	y	z	
	20	16	11	6

Table 3 – Averaged values of porosity and permeability needed to initialize the FEM.

5.3 Model to mesh

The software used to mesh was the open-source MeshIt. Meshit is a three-dimensions software to generate high-quality boundary conforming Delaunay tetrahedral meshes, for Finite Element of complex faulted reservoir applications, (Cacace and Blöcher, 2016).

Dimensions

In the numerical model a domain with extensions of 10770.3 m (E-W), 20880.6 m (N-S) and 7200 m in vertical direction was considered (Figure17). Northern limit is 1500 m to the north of Well A (Mac-x.1001 bis) in the border with Bolivia. In the south of Well C (Mac.e-1003) there is a margin of 10000 m where the reservoir deepens. Laterally, to the east the alignment of the wells strike (in between 2000m to 4000m), there is the Acheral-Fault which will be considered as an impermeable limit. To the west the reservoir dips down. Thus a margin of 4000 m (respect to the alignment of the wells) is given catching convective effects. No interactions between the wells and the impermeable sediments above and below the reservoir are expected in the numerical modelling.

Discretization

The model to mesh consist of the units described in Table 4. The geological units have been constrained by two surfaces defining the geological interfaces, four additional surfaces defining laterals boundaries, and two more for the top and base of the model. Figure 20 shows the constrained lines to create volumes. Figure 21 depicts the final stage of meshing process.

Type	Name	Material	Size
Unit	ZT Layer 1	0	384
Unit	Icla2 Limolite Layer 11	0	384
Unit	Upper Limit	1	1024
Unit	Lower Limit	2	1024
Fault	Small-Fault	3	128
Fault	Acheral-Fault	4	384
Fault	Fault-1	5	1024
Border	East	6	1024
Border	North	7	1024
Border	West	8	1024
Border	South	9	1024
Well	1001 bis	10	32
Well	1002	11	32
Well	1003	12	32
Well	1004 (d)	13	32
Well	1006 (d)	14	32

Table 4 – Input for the meshing procedure. Type, name, material and mesh size of 11 surfaces and five polylines.

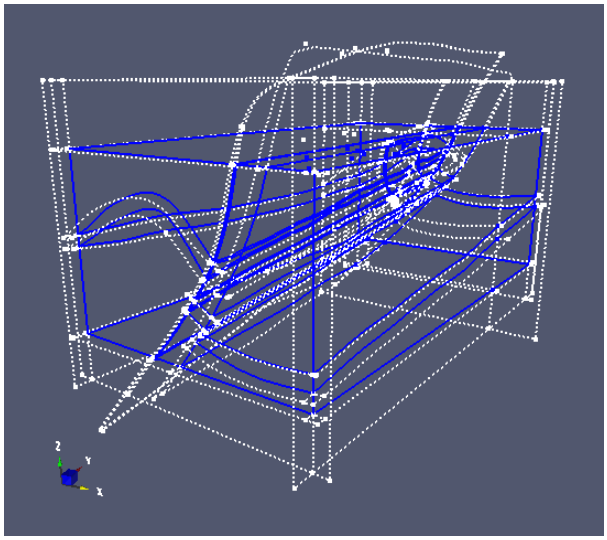

Figure 20 – Selected constraints (in blue) for meshing surfaces and volumes of the model.

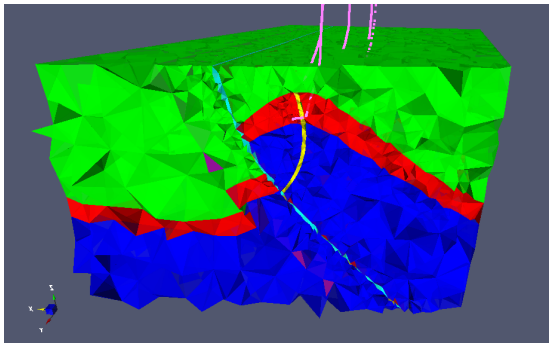

(a) View of the model from the north. Cross section showing Well A crossing the Small Fault.

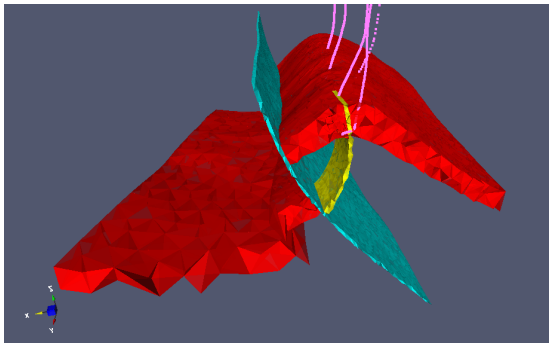

(b) Reservoir interval, main faults, and wells represented by their materials.

Figure 21 – Final result of the meshing procedure, indicating the difference of each material refinement sizes.

6 Numerical modeling

6.1 Numerical equations

In Böttcher et al. (2015), the differential equations and the solving method are explained in detail. Here is a resume of the main concepts for understanding the method to solve the equations that govern fluid flow, heat and mass transfer from basic conservation principles.

Heat balance

Flow rates of heat (energy) in porous media can be described by balance equations. The heat balance equation is expressing an equilibrium of thermal processes, i.e. heat storage, diffusive and advective fluxes as well as heat sources and sinks.

$$c\rho\frac{\partial T}{\partial t} + \nabla.\left(j_{diff} + j_{adv} + j_{disp}\right) = Q_T \tag{1}$$

where Q_T is the heat production term in $\left[J.m^{-3}.s^{-1}\right]$].
The following are the governing equations of heat transport in porous media

Energy balance

The equation of energy conservation is derived from the first law of thermodynamics which states that the variation of the total energy of a system is due to the work of acting forces and heat transmitted to the system.
The total energy per unit mass e (specific energy) can be defined as the sum of internal (thermal) energy u and specific kinetic energy $v^2/2$. Internal energy is due to molecular movement. Gravitation is considered as an energy source term. The conservation quantity for energy balance is total energy density

$$\psi^e = \rho.e = \rho\left(u + v^2/2\right) \tag{2}$$

Using mass and momentum conservation we can derive the following balance equation for the internal energy.

$$\rho\frac{du}{dt} = \rho.q^u - \nabla.\left(j_{diff} + j_{disp}\right) + \sigma : \nabla v \tag{3}$$

where q^u is the internal energy (heat) source, j_{diff} and j_{disp} are the diffusive and dispersive heat fluxes, respectively. Utilizing the definition of the material derivative

$$\frac{dT}{dt} = \frac{\partial T}{\partial t} + v.\nabla T \tag{4}$$

and neglecting stress power, we obtain the heat energy balance equation for an arbitrary phase

$$\rho c\frac{\partial T}{\partial t} + \rho cv.\nabla T - \nabla.\lambda\nabla T = \rho qT \tag{5}$$

where λ contains both the diffusive and dispersive heat conduction parts.

Porous medium

The heat balance equation for the porous medium consisting of several solid and fluid phases is given by:

$$\sum_{\alpha} \epsilon^{\alpha} c^{\alpha} \rho^{\alpha} \frac{\partial T}{\partial t} + \nabla . \left(\sum_{\gamma} n S^{\gamma} \rho^{\gamma} c^{\gamma} v^{\gamma} T - \sum_{\alpha} \epsilon^{\alpha} \lambda^{\alpha} \nabla T \right) = \sum_{\alpha} \epsilon^{\alpha} \rho^{\alpha} q_{th} \tag{6}$$

where α is all phases and γ is fluid phases, and ϵ^{α} is the volume fraction of the phase α. Most important is the assumption of local thermodynamic equilibrium, meaning that all phase temperatures are equal and, therefore, phase contributions can be superposed. The phase change terms are cancelled out with the addition of the individual phases.
With the following assumptions:

- local thermal equilibrium
- fully saturated porous medium
- neglecting viscous dissipation effects

the governing equations for heat transport in a porous medium can be further simplified.

$$(c\rho)^{eff} \frac{\partial T}{\partial t} + (c\rho)^{fluid} v . \nabla T - \nabla . \left(\lambda^{eff} \nabla T \right) = qT \tag{7}$$

with

$$(c\rho)^{eff} = \sum_{\alpha} \epsilon^{\alpha} c^{\alpha} \rho^{\alpha} \tag{8}$$

$$(c\rho)^{fluid} = n \sum_{\gamma} S^{\gamma} c^{\gamma} \rho^{\gamma} \tag{9}$$

$$\lambda^{eff} = \sum_{\alpha} \epsilon^{\alpha} \lambda^{\alpha} \tag{10}$$

For isotropic heat conduction without heat sources and we have the following classic diffusion equation

$$\frac{\partial T}{\partial t} = \nabla . \left(\alpha^{eff} \nabla T \right) \tag{11}$$

with heat diffusivity $\alpha^{eff} = \frac{\lambda^{eff}}{c\rho^{eff}}$

Boundary Conditions

In order to specify the solution for the heat balance equation 1 we need to prescribe boundary conditions along all boundaries. The following boundary conditions are used:

1. Prescribed Temperatures (Dirichlet conditions)

$$T = \overline{T} \; on \; \Gamma_T \tag{12}$$

2. Prescribed heat fluxes (Neumann Conditions)

$$q_n = j_{diff}.n \; on \; \Gamma_q \tag{13}$$

Darcy's law

For linear momentum conservation in porous media with a rigid solid phase it is possible to assume that, in general, inertial forces can be neglected (i.e. $\frac{\mathrm{d}v}{\mathrm{d}t} \approx 0$) and body forces are gravity at all. Furthermore and taking into account that fluid friction on the fluid-solid interface and that turbulence effects can be neglected we obtain the Darcy law for each fluid phase Γ in multiphase flow.

$$q^\gamma = nS^\gamma v^\gamma = -nS^\gamma \left(\frac{k_r^\gamma}{\mu^\gamma} \left(\nabla p^\gamma - \rho \gamma g \right) \right) \tag{14}$$

Resolution of the numerical equation

For this nonlinear equations problem, an approximate solutions must be obtained. Finite Difference Method was used to approximate time derivatives. The Finite Element Method are employed for spatial discretization of the region. The Galerkin weighted residual approach is used to provide a weak formulation of the Partial Difference Equations (PDE).
The procedure of obtaining the approximate solution consists of two steps. The first step converts the continuous partial differential equations and auxiliary conditions (IC and BC) into a discrete system of algebraic equations in a finite difference method (FEM). This first step is named discretization. The replacement of PDE by algebraic expressions introduces a defined truncation error. The second step of the solution procedure requires the solution of the resulting algebraic equations. This process can also introduce an error but this is usually small compared with those involved in the above mentioned discretization step.
In the present thesis, a non-linear solver is employed. The iterative method employed to solve this non-linear problem is the Picard method (fixpoint iteration). More details about the Picard method can be found in Böttcher et al. (2015) page 26.

6.2 Model set-up

Steady-state pressure and temperature distribution have to be simulated. Dirichlet boundary conditions for the laterals of the model have been imposed representing hydrostatic conditions. The top and base of the model were constrained by Dirichlet temperature boundary conditions. Unperturbed initial pressure and temperature conditions for the steady-state simulation were the hydrostatical water gradient and the temperature of the synthetic temperature profile calculated later for Well A.

The simulated cases will consider a withdrawal of -20 lt/s of reservoir fluids and a reinjection of cooled fluid of 20 l/s injection. This total fluid withdrawal keeps constant in spite of the chosen scenario. Some cases splits the flow injection/production rate into two wells (10 l/s each). The fluid after withdrawal of heat inside the power plant has a temperature of 50 ℃ used as injection temperature. Production and injection rates are implemented with Neumann-type

boundary conditions at the uppermost node of each well. At the same node a temperature Dirichlet-type boundary condition is set to resemble the re-injection of cooled fluid. Both viscosity and density contrasts, and turbulent flow are not considered in this simulations.

Reservoir temperature profile estimation

With the Fourier's Law, a temperature profile was calculated for the specific location of Well A. Available temperature data was collected from wells logs (mostly Dip-Logs) after the corresponding drilling stages in Well A (original and sidetrack). Aditionally, was necesary to use averaged thermal conductivities of the different type of drilled rocks in Well A. A value of heat flux density of this region was extracted from the paper of Husson and Moretti (2002).

A detailed mud-log of Well A was used. The lithological profile contents the percentage abundance of different type of rocks described every two meters while drilling. A list of the different types of rock along the well is given in Table 16 in Appendix A with their respective thermal conductivity values.
A heat flux density of 45.75 [mW/m^2] was used. This value averages in between heat flux densities registered at SAZ_Foothills 50[mW/m^2] and SAZ_Chaco-plain 40[mW/m^2], where Macueta field locates see Fig 10. The criteria behind this option lies on the fact that Bottom Hole Temperature (BHT) seems not to be highly affected during different stages of the well test. By this reason could be expected a small change of temperature along the time this well was in production. On the other hand, dip-log temperatures (acquired after drilling each stage) have been affected in fact, by reason of the open hole circulation some meters above the bottom of the hole, which is the case normally before well logging, see Fig 22.

The solution of the heat transport equation with finite differences method is as follows. First the heat transport equation is presented.

$$\frac{dq}{dx} = -\frac{d^2T}{dx^2} = A \tag{15}$$

Assuming that marine sediments have largely filled this basin, a slightly lower level of radioactive contribution is expected. So that, the radioactive term A on this equation will be consider as 0. Finally the expression to obtain 1D temperature increments along the vertical section is as follows.

$$T(z) - T_o = \Delta T = -\frac{q_o.(-z)}{\lambda_{geom}} \tag{16}$$

Thermal conductivity was corrected by a Geometrical Mean model, which considers the porosity of every formation, the thermal conductivity of the solid phase and the mentioned fluid phase.

$$\lambda = (\lambda)_f^{\phi}.(\lambda)_s^{1-\phi} \tag{17}$$

In Figure 22 the sinthetic Temperature Profile is plotted together with the temperature registered at the bottom of the well two and a half years after production started in Well A. These values were acquired during an extended build-up test (communications with PAE, 2017). More details

about Build-Up Test in Appendix A.

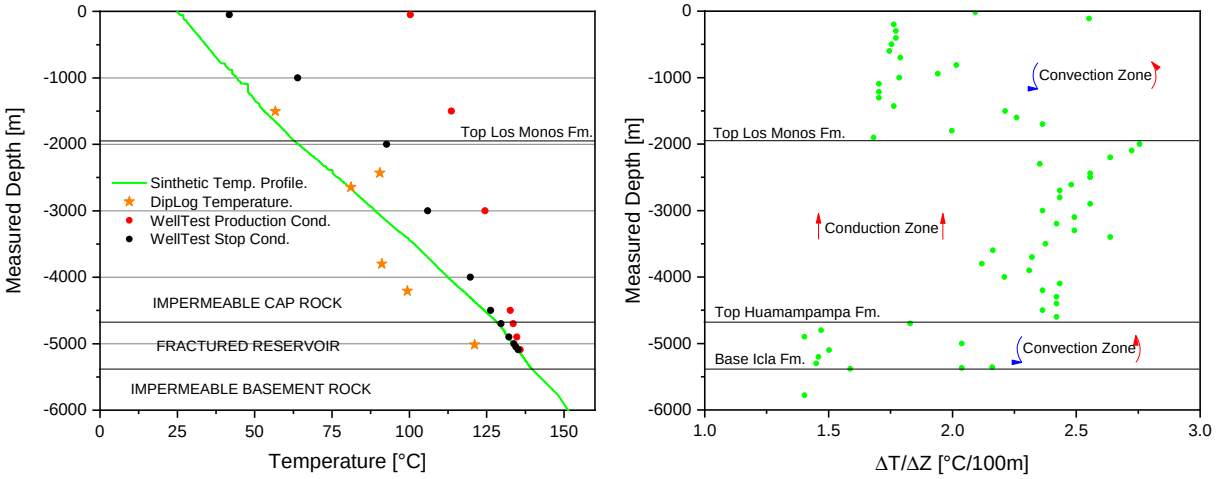

(a) Synthetic temperature profile. Changes of slope are represented in the next figure.

(b) Green dots represents changes in the temperature gradient. The isolating properties of Los Monos Fm. can be seen here, as well as convectives zones inside the reservoir interval.

Figure 22 – Synthetic temperature profile development for Well A in Macueta field.

Parameters and boundary condition values for the Thermo-Hydraulic model are listed in Tables 5 to 8.

Mat. ID		0	1	2
Formations	Units	Huamampampa+Icla	Los Monos	Top Santa Rosa
Porosity	[%]	0.03	0.01	0.01
Permeability [x]	$[m^2]$	2.55E-14	1E-18	1E-18
Permeability [y]	$[m^2]$	7E-16	1E-18	1E-18
Permeability [z]	$[m^2]$	2.55E-14	1.00E-18	1.00E-18
Density	[kg/m^3]	2650	2650	2650
Specific heat cap.	[J/kg.k]	920	920	920
Thermal conduc.*	[W/m.k]	3	1.96	2.6

Table 5 – Formation properties. *Thermal conductivity calculated as average value for each separated interval. Mean Geometric correction was applied to λ values.

Mat. ID		3	4	5
Faults	Units	Acheral	Small	01
Porosity	[%]	0.01	0.01	0.01
Permeability [x]	[m^2]	1.00E-18	1.00E-17	1.00E-18
Permeability [y]	[m^2]	1.00E-18	3.00E-15	1.00E-18
Permeability [z]	[m^2]	1.00E-18	3.00E-15	1.00E-18
Density	[kg/m^3]	2650	2650	2650
Specific heat capacity	[J/kg.K]	920.00	920.00	920.00
Thermal conductivity*	[W/m.K]	3.00	3.00	3.00

Table 6 – Fault parameters. *Faults have an increased thermal conductivity due to thermal properties of silicate cement.

Mat. ID		6	7	8
Well	Units	Mac-x.1001 bis	Mac-1004	Mac-x.1003
Cross sectional area	[m]	0.22	0.22	0.22
Porosity	[%]	1	1	1
Permeability	[m^2]	1.00E-06	1.00E-06	1.00E-06

Table 7 – Well parameters. Completion of the wells are open hole.

General Model Properties	Units	Values
Production Rate*[1]	[lt/s]	-10/-20
Injection rate*[2]	[lt/s]	10/20
Injection temperature*[3]	[℃]	50
Fluid density	[kg/m^3]	1000
Fluid viscosity*[4]	[kg/(m·s)]	Modeled
Fluid specific heat capacity	[J/(kg.K)]	4200
Fluid thermal conductivity	[W/(m.K)]	0.65
Approx. temperature @ the top	[℃]	78.0
Approx. temperature @ the bottom	[℃]	188.0
Approx. pore pressure @ the top	[MPa]	45.0
Approx. pore pressure @ the bottom	[MPa]	108.5

Table 8 – Model parameters. *[1,2] Production and injection are splited in case of more than one producer or injector well. *[3] Injection temperature after ORC-Process. *[4] Water Viscosity was considered in the OpenGeosSys Liquid model

6.3 Sensitivity Analisys

An approximation to the convergence and stability of the select model was done. In Tables 9, 10, 11 the refinement sizes of the selected models are presented. The refinement was done over

the most sensitive elements of the model. Refinement over the reservoir material was splited in two. The ”Connected Reservoir” is defined as part of the reservoir in the same block the wells are located. The ”Well” material and the ”Small Fault” material has been also tested. The model 512b. was set as the ”Base Case” (Table 9).

Figures 25 to 30 compare the different models made for one Injector and one Producer Well, where pressure and Temperature were measured vertically and horizontally across the model. Figures 31a and 31b include the final temperature and pressure values at the production or injection point, for every single simulated model after 1.e^8 seconds.

As increases the number of tetrahedrons increases the simulation time exponentially. The optimum model (Final Model) was developed increasing the Reservoir, Small Fault, and Well refinement, ensuring that the accuracy and calculation time are acceptable. As acceptability criteria was considered the inclusion of the Final Model into the trend of the rest of the simulated models (Figures 31a and 31b). The Final Model is presented in Table 12.

Model Name	Connected Res.	Isolated Res.	Faults	Borders	Tops	Well	N° Tetrahedrons
512b. m	512	1024	512	1024	1024	32	83514
256 m	256	1024	512	1024	1024	32	182712
128 m	128	1024	512	1024	1024	32	652190
64 m	64	1024	512	1024	1024	32	2682509

Table 9 – Reservoir refinement. Case 512b. is used to compare the rest of the models.

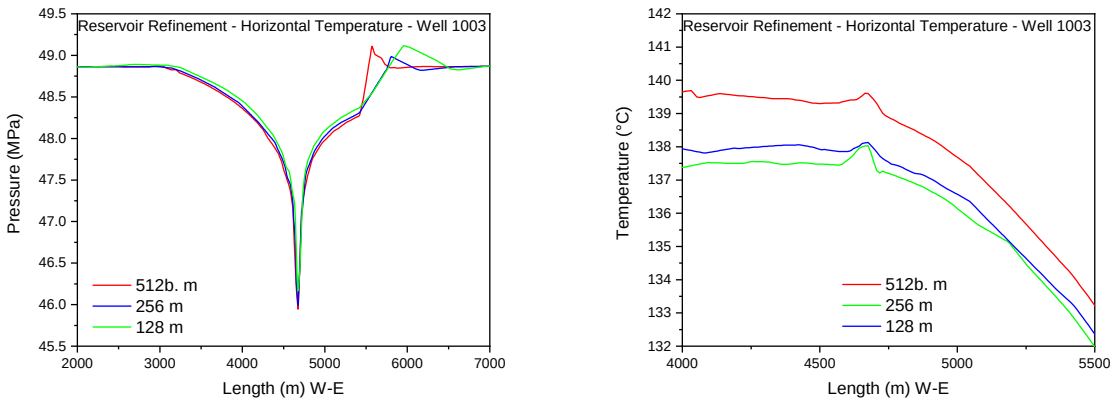

(a) . **(b)** .

Figure 23 – Sensitivity analysis of the reservoir. Horizontal temperature and pressure in the Producer well.

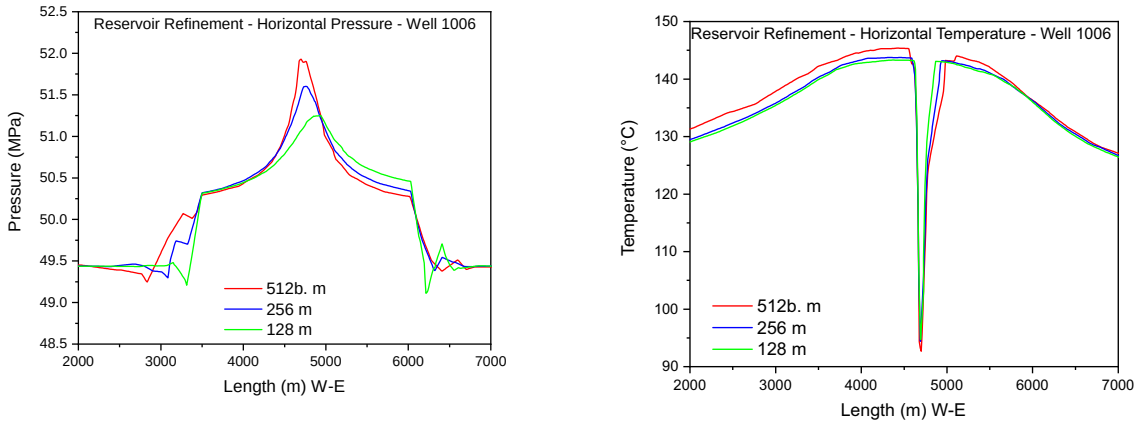

(a) . **(b)** .

Figure 24 – Sensitivity analysis of the reservoir. Horizontal temperature and pressure in the Injector well. The ”tip” of the curves are the injection points.

Model Name	Connected Res.	Isolated Res.	Faults	Borders	Tops	Well	N° Tetrahedrons
16 m	512	1024	512	1024	1024	16	102174
8 m	512	1024	512	1024	1024	8	137714
4 m	512	1024	512	1024	1024	4	204998

Table 10 – Well refinement. (Values in meters)

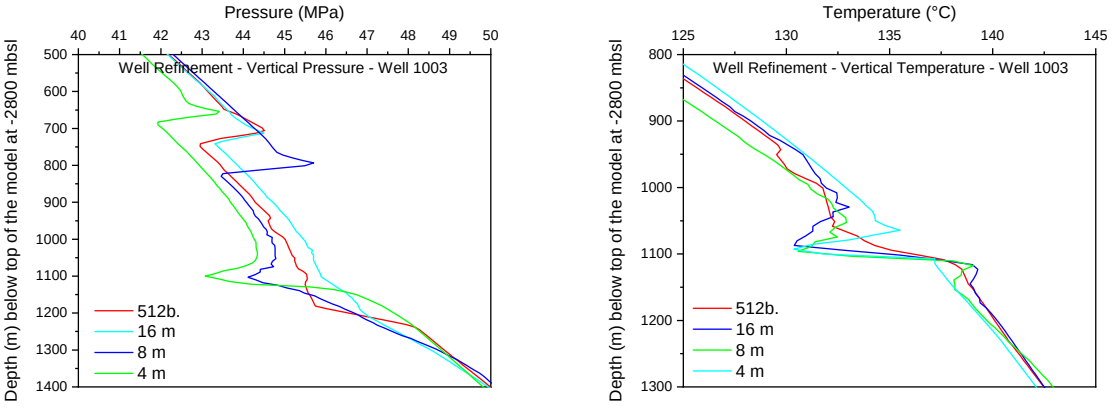

(a) . **(b)** .

Figure 25 – Well Sensitivity analysis . Vertical pressure and temperature in the Producer well.

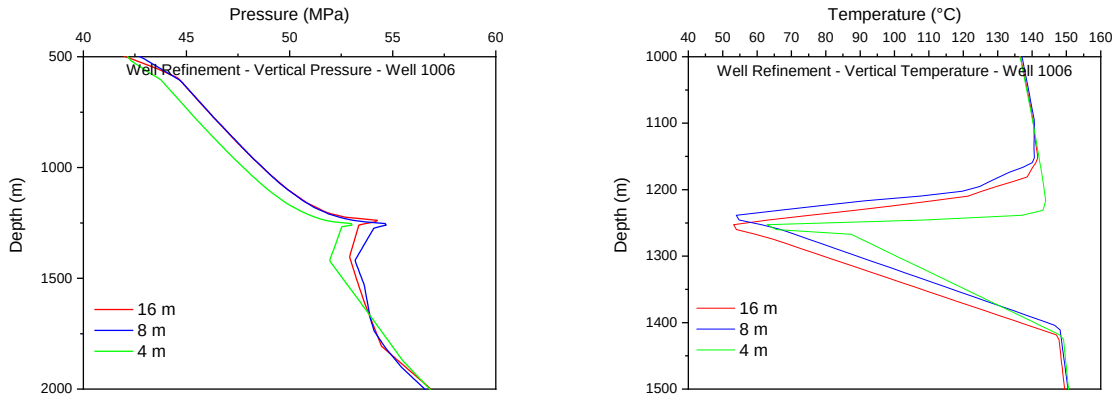

(a) . **(b)** .

Figure 26 – Sensitivity analysis of wells. Vertical pressure and temperature in the Injector well.

Model Name	Connected	Isolated	Faults	Small Fault	Borders	Tops	Well	N° Tetra-hedrons
512 m	512	1024	512	512	1024	1024	32	58839
128 m	512	1024	512	128	1024	1024	32	107911
64 m	512	1024	512	64	1024	1024	32	251854

Table 11 – Small Fault refinement.

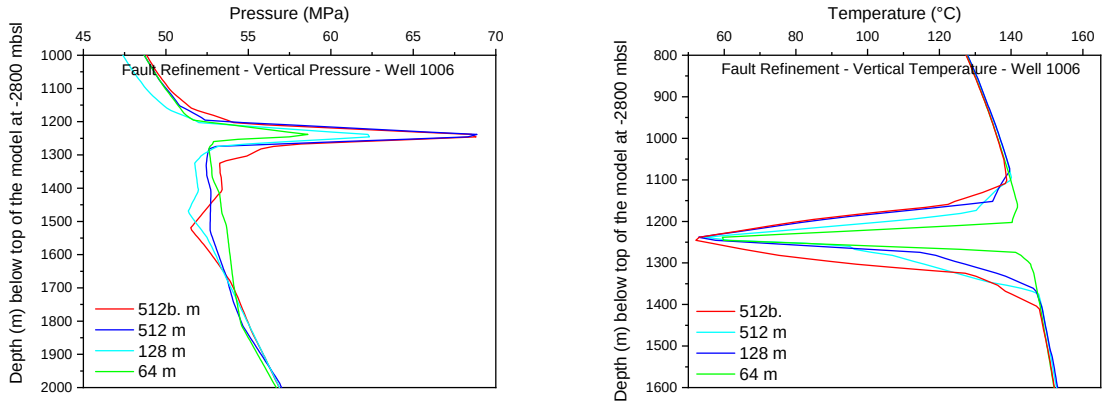

(a) . **(b)** .

Figure 27 – Sensitivity analysis of the small fault. Vertical pressure and temperature in Injector well.

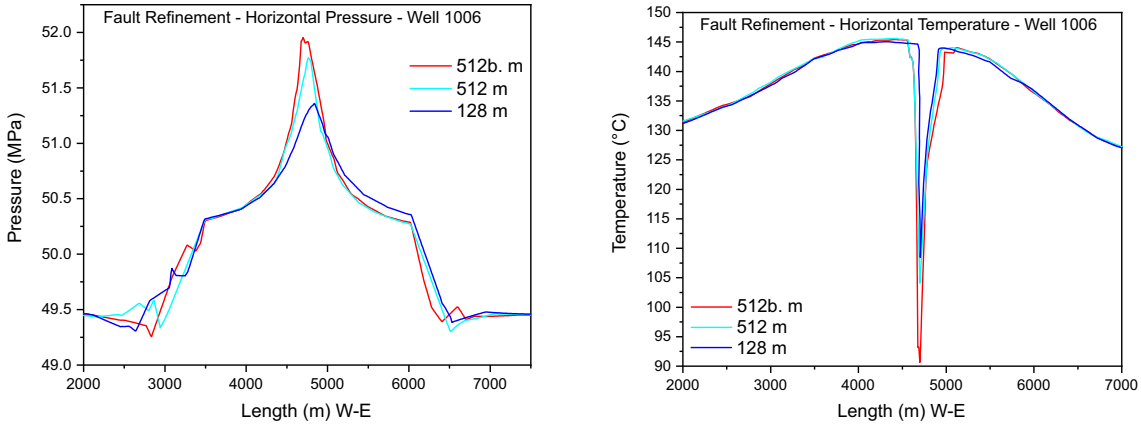

(a) . **(b)** .

Figure 28 – Sensitivity analysis of the small fault. Horizontal pressure and temperature in Injector well.

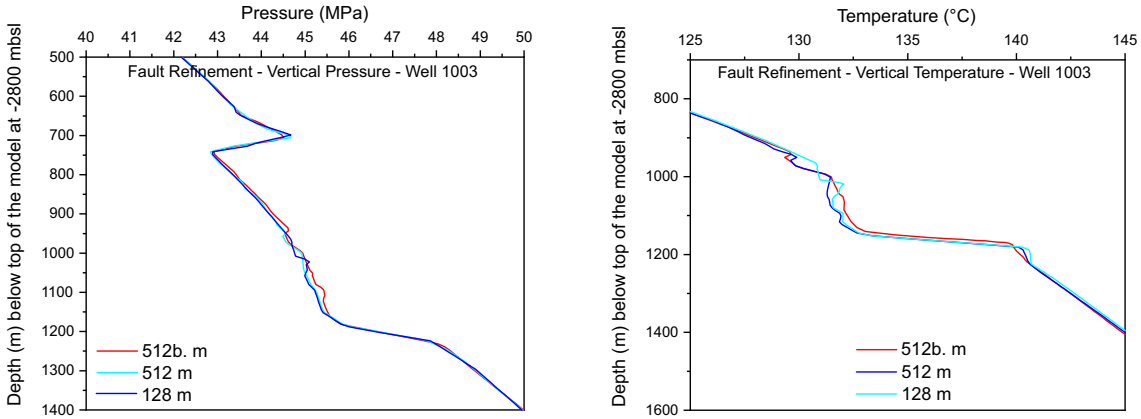

(a) . **(b)** .

Figure 29 – Sensitivity analysis of the small fault. Vertical pressure and temperature in Producer well.

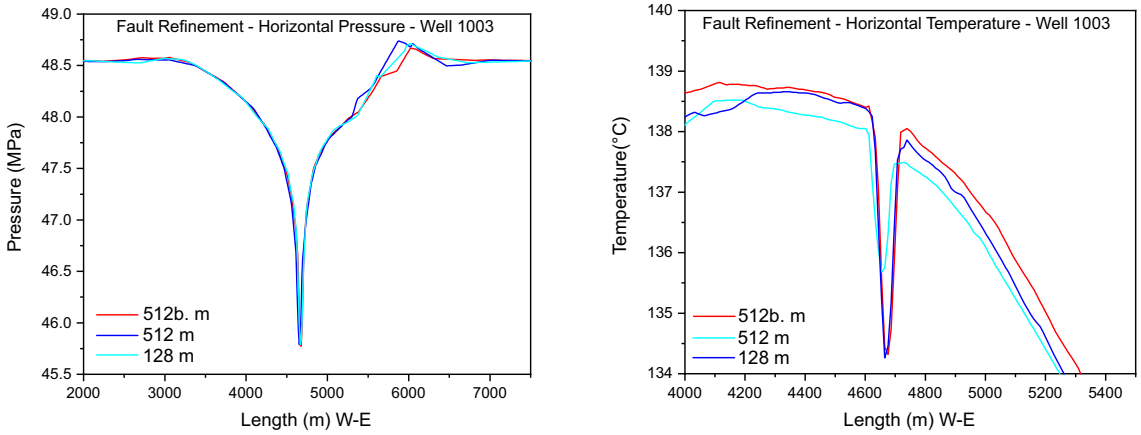

(a) . **(b)** .

Figure 30 – Sensitivity analysis of the small fault. Horizontal pressure and temperature in Producer well.

Model Name	Connected Res.	Isolated Res.	Faults	Small Fault	Borders	Tops	Well	N° Tetrahedrons
384 m	384	1024	384	128	1024	1024	16	208126

Table 12 – Selected grid refinement.

The finally chosen model converges to the results and it is able to be run on a normal personal computer. This final model includes an optimized amount of tetrahedrons for the reservoir, faults, and wells. On the other hand, the size of the tetrahedrons in the isolated part of the model (reservoir, basement and sealant cap) are much bigger, not interfering with the precision of the calculus.

In Figure 31, final pressure and temperature values after 1.e8 sec vs N° of tetrahedrons in the model is plotted. Since a true value was not available to verify the convergence of the results, the stability of the results in a given range was used as a criterion for selecting the most appropriate model. Computational time was also a key parameter in choosing the most suitable refinement mesh. In Figure 31a green points are simulations done in the presence of the Small Fault. For the red ones, the Small Fault was no present. Well 1006 is located a side of the Small Fault. Figure 31b is possible to observe the Final Model (black icon) inside the general trend. Well 1003 (Well C) is far enough from the fault, so it is not influenced by it.

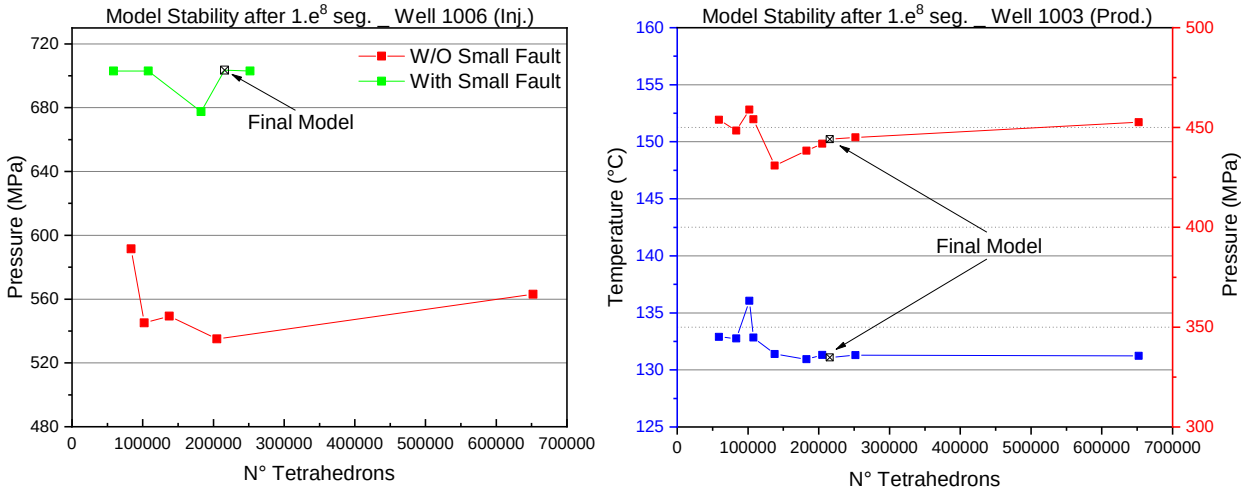

(a) **(b)**

Figure 31 – Selected refinement compared with other refinement models.

6.4 Calibration

Equivalent water flow rate calculation

In 2009 a well test was made in Well A. During this test, in production and in stop condition values of temperature and pressure were taken. This test was used to match iteratively the FEM with the real well behaviour during the shut-in and the following build-up period.

All the properties previously defined have been kept constant, with the exception of the reservoir and Small Fault permeability tensors. In this model Well A crosses the small fault.
The build-up Test done in Well A have produced gas, and a small amount of water, and condensable hydrocarbons. With the aim of making the comparison between the model (one-phase flowing) and the test (two-phase flowing), gas production has to be converted to a liquid production.
To simulate the depletion effect, gas and liquids FVF (formation volume factor) at reservoir temperature and pressure has to be calculated. The specialized software PROSPER (Petroleum Experts Limited) was used to calculate conversion factors under reservoir conditions.

Interpolated values of FVF and equivalent averaged rate of liquids production in Appendix B. Reservoir pressure of 34.927 MPa and temperature of 130℃ are the reservoir conditions during well-test production conditions.
By the time of the test, the well has been flowing for 2 years and 9 months. The cumulative production during this period was later calculated as a constant flow rate. Production is normally measured at the entrance point of the separator facilities. Finally, the FVF of each phase was introduced and a final rate in reservoir conditions was calculated.

Phase	Gas	Oil	Water	Total m^3/s (Res)
Accumulated Prod.	2729297374.91	366577.49	29952.05	
Caudal [m^3/d] (Sup)	2737509.90	367.68	30.04	
Caudal [m^3/s] (Sup)	31.6841	0.0043	0.0003	
FVF [m^3/m^3]*	0.0043	1.5137	1.0565	
Caudal [m^3/s] (Res)	0.1334	0.0064	0.0004	0.14

Table 13 – Calculation of the water constant rate at reservoir conditions, which corresponds to the addition of gas, water and condensate production.

The value of 0.14 m^3/s at reservoir conditions will be introduced in the FEM in order to find the permeability tensor needed to match with the registered pressure changes by the time production was stopped as part of the Build-up Test.

Reservoir pressure calibration

In the reservoir gas, condensate and water phase are hydraulically connected. Completion of Well A allows the entire reservoir interval production. The gas cap in the Macueta structure has a transitional Gas-Condensate and Condensate-Water contact due to strong capillary pressures effects. Density values calculated together with the FVF have ben also compared with the fluid gradient obtained during the well test.
The difference of pressure inside the well and in the reservoir will be analysed. The pressure inside the well responds to the gas column plus the counter-pressure at the well head, while reservoir pressure is controlled by the fluids inside the reservoir. In the case of the FEM, this pressure is represented by the water hydrostatic column. In Figure 32 trajectory of Well A is also plotted. Both curves share the same production node,so they have the same pressure value.

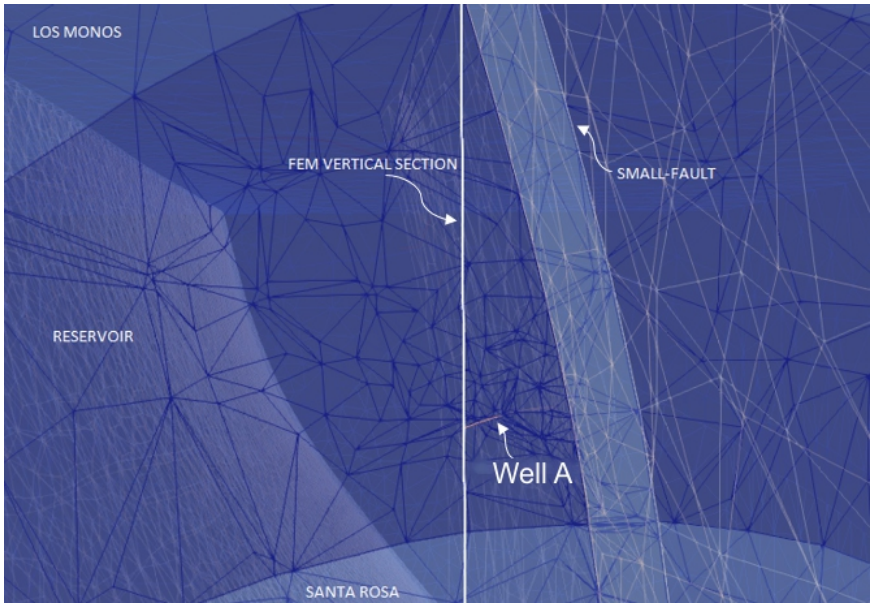

Figure 32 – Schematic representation of the shared node, where the pressure of the reservoir and well are the same.

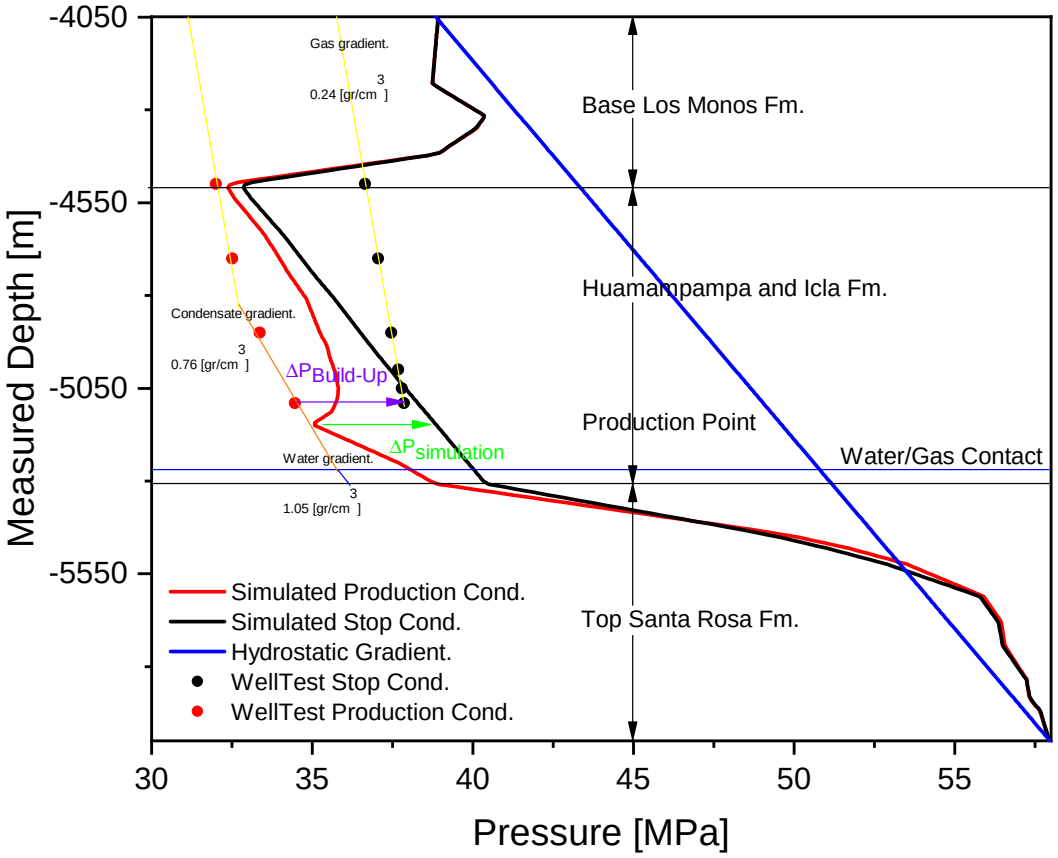

Figure 33 – Graphical method to match the well test real data (dynamic and static gradient pressures) with FEM simulation in Well A.

Figure 33 shows in black, for stop conditions, and in red, for production conditions, how the pressure behaves the pressure inside the reservoir in a vertical pressure profile (simulated case). The curved red line of pressure has a peak where the production point of the simulated well allows fluid enter to the well (simulated completion). This ”peak” is in contact with the line which connected the red dots (well test production condition), meaning that reservoir is in contact with the well conditions (production node). The same is valid for the stop condition. The arrows in violet and in light green have the same length, which means that the same difference of pressure for both, the real and the simulated case has been reached.

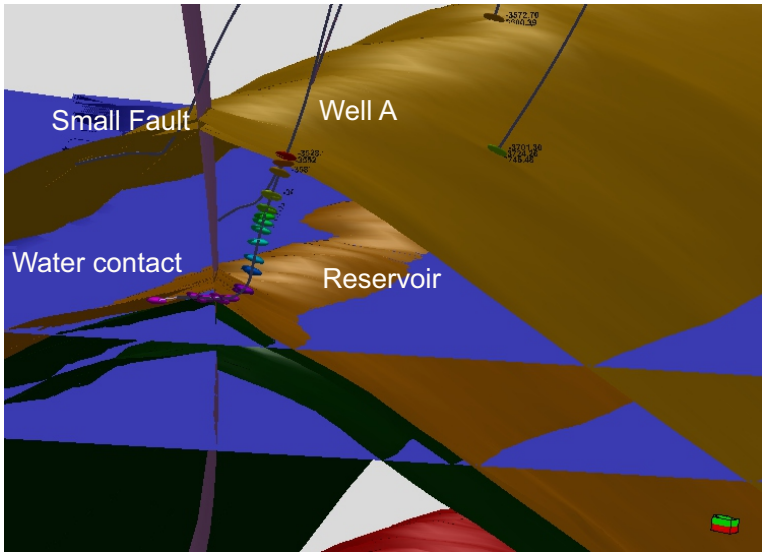

Figure 34 – Interpreted water contact in the San Alberto field and extrapolation to the Macueta Field. (Navia Vargas, 2017)

Despite Well A has their completion above this level, capillarity forces are strong enough to generate a water transition zone. Temperature changes between the FEM and the well test changes just a little for the period of the matching procedure. Then temperature matching was not taken into account.
As was mentioned, the lower face of the faults has the particularity of having an improved directional permeability due to the existence of fractures connectivity. This fact was included as a characteristic of the materials which represents the fault in the FEM.

6.5 Simulated scenarios.

Different schemes of production injection have been chosen. Those schemes includes Well A (Northernmost position in the field), Well B (in the middle of the field) and Well C (in the southernmost position). The scenarios consists, in Four well-doublet (two coupled cases) and six three-spot patterns. In the case of well-doublets, Well A is always present as an injector, commuting later in the same coupled case to a producer well. Well A injects or produces depending on the case in the vicinity of the small fault. In the case of the three-spot patterns, a variety of schemes of production injection covers a wide spectrum of possibilities, which later allowed a comparison from the energetic point of view.

List of simulated cases.

In Table 14 the cases to be simulated are presented. Simulations are performed considering a constant water (production) injection rate. The injection temperature will be 50℃ and the simulation time is 39.3 years.

Case	Well	Type	Q [l/s]	Case	Well	Type	Q [l/s]
Case 1_1	Well A	Injector	10	Case 3_1	Well C	Producer	-10
	Well C	Producer	10		Well B	Producer	-10
Case 1_2	Well A	Producer	-10		Well A	Injector	20
	Well C	Injector	10	Case 3_2	Well C	Injector	10
Case 2_1	Well A	Injector	10		Well B	Injector	10
	Well B	Producer	-10		Well A	Producer	-20
Case 2_2	Well A	Producer	-10	Case 4_1	Well C	Injector	10
	Well B	Injector	10		Well B	Producer	-20
					Well A	Injector	10
				Case 4_2	Well C	Producer	-10
					Well B	Injector	20
					Well A	Producer	-10
				Case 5_1	Well C	Injector	20
					Well B	Producer	-10
					Well A	Producer	-10
				Case 5_2	Well C	Producer	-20
					Well B	Injector	10
					Well A	Injector	10

Table 14 – List of cases to be simulated. Four well-doublet and six three-well patterns.

Main components of the model.

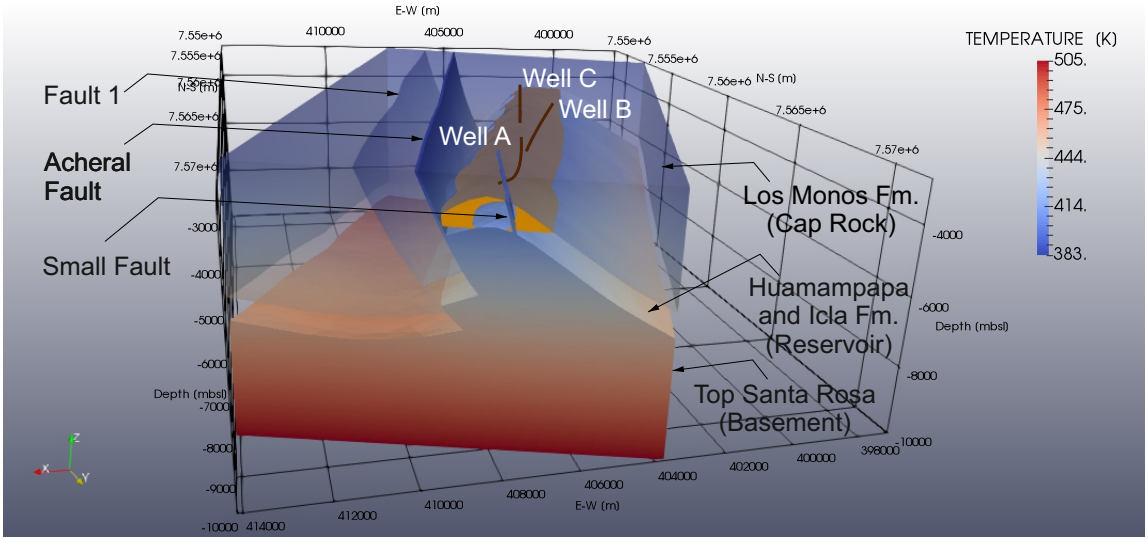

Figure 35 – All main components in the geothermal model.

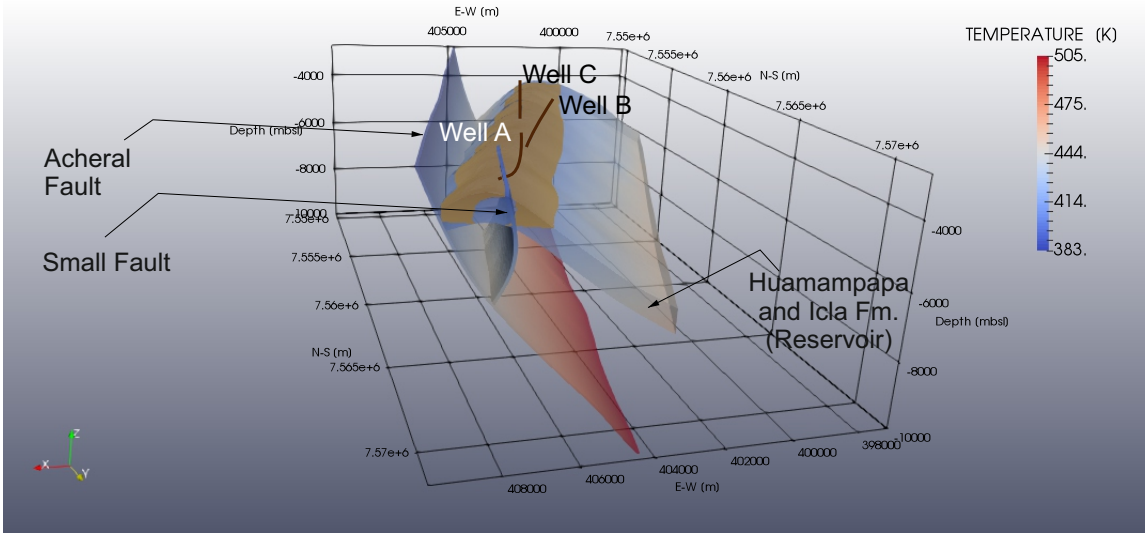

Figure 36 – Components of the geothermal model which later will affect the flow pattern.

Results of the simulations. BHT.

A summary of the simulated BHT (Bottom Hole Temperature) are presented here. Well A, B and C have been compared in separated graphs. In Well A, the following flow rates have been used $Q_{3-2} = -20\ l/s$, $Q_{1-2} = Q_{2-2} = Q_{4-2} = Q_{5-1} = -10\ l/s$.

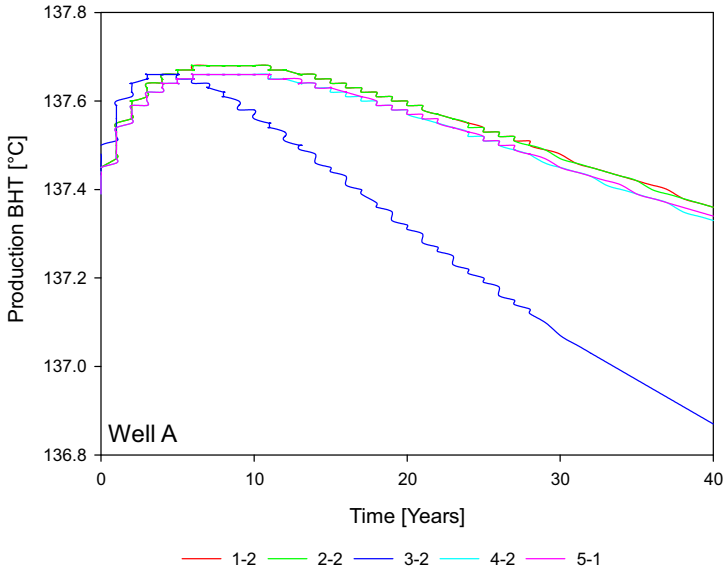

Figure 37 – Well A _ BHT values for the simulated cases.

Well B. The following flow rates have been used $Q_{4-1} = -20\ l/s$, $Q_{2-1} = Q_{3-1} = Q_{4-1} = -10\ l/s$.

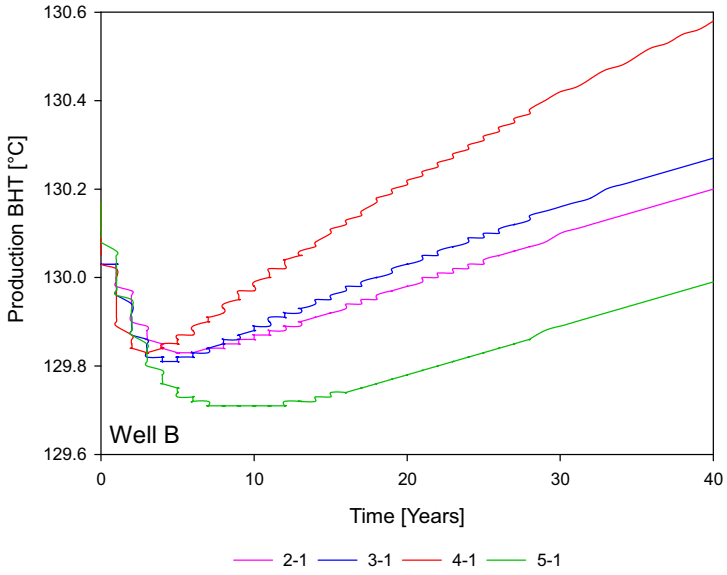

Figure 38 – Well B _ BHT values for the simulated cases.

Well C. The following flow rates have been used $Q_{5-2} = -20\ l/s$, $Q_{1-1} = Q_{3-1} = Q_{4-2} = -10\ l/s$.

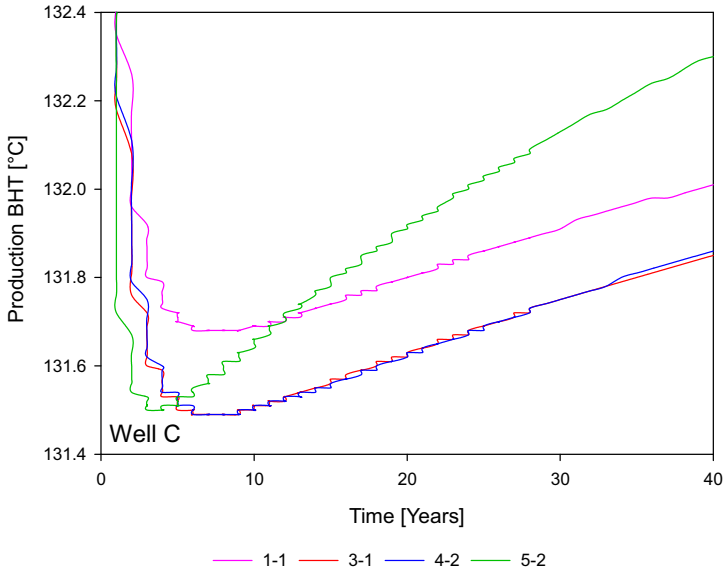

Figure 39 – Well C _ BHT values for the simulated cases.

Wells A, B and C doesn't show markedly difference of BHT Temperatures. These differences are in the order of one degree. In the Figure 40 can be seen a comparison between the three wells. The main reason for the diversity in BHT is due to the difference in depth of each production point. Completion points are located in Well A= -4056.9 m, Well B= -3702.9 m and Well C= -3982.0 m. In any case, are meters below sea level.

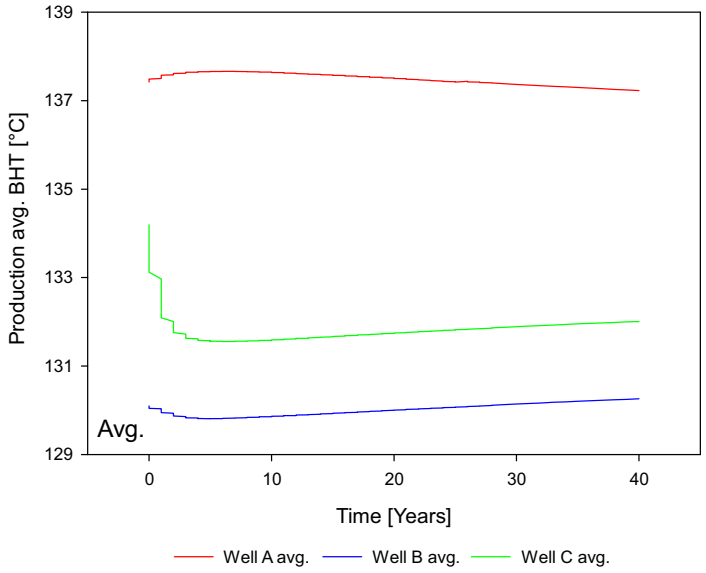

Figure 40 – Comparison of the three well´s average BHT.

As a result of the difference in BHT temperatures, it could initially be expected that the best case would be that involving the production of Well A.

Productivity Index

The productivity index relates the (injection) production flow rate to the difference in reservoir pressure and dynamic flowing pressure. The evolution of this index depends on the inherent properties of the reservoir (permeability anisotropies, fractures, and faulted zones) as well as the interference between the wells.
The injected water will be more or less effective to maintain the Average Reservoir Pressure $(\overline{Pr})$ in presence of those mentioned anisotropies. The drawdown pressure $\Delta P_{dd} = \overline{Pr} - P_{wf}$, where P_{wf} is the pressure at the bottom of the hole in the (production) injection point, is adjusted automatically during the simulation in order to keep the (production) injection rate as a constant value. In the case of a production well, if the $\overline{Pr}$ increment reached is not enough then P_{wf} has to decrease the necessary to maintain the ΔP_{dd}. In a real case, more energy must be expended on the ESP (Electric Submersible Pump) to overcome the pressure losses to the downstream nodes.
The above analysis applies also to the injection case. The $\overline{Pr}$ will make more or less difficult water injection, consequently, the P_{wf} must increase also energy consuming to maintain the injection rate constant.
In Figures 41 to 43 show productivity indices of production (a) and injection (b) for the different cases.

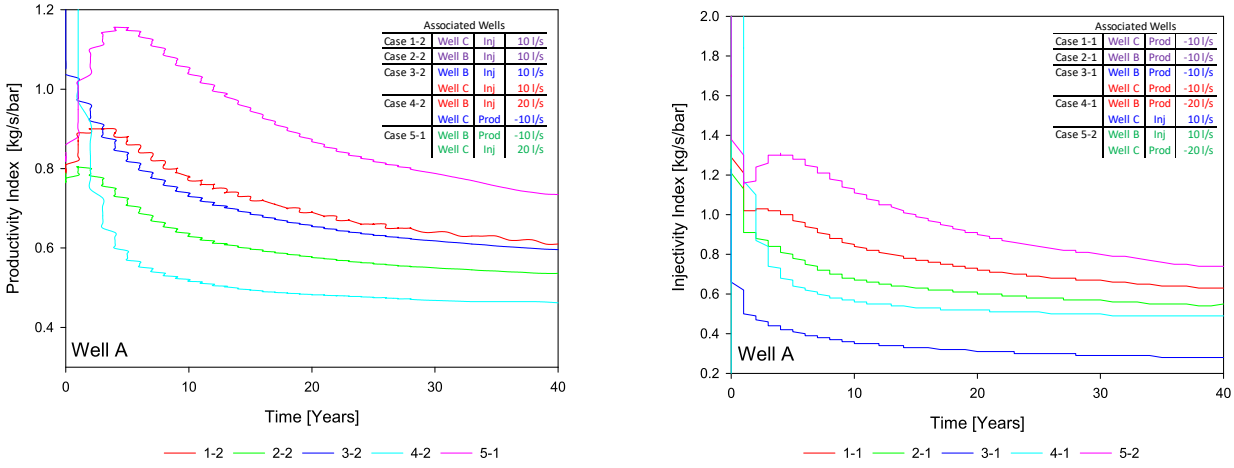

(a) **(b)**

Figure 41 – Well A _ Productivity and Injectivity Index

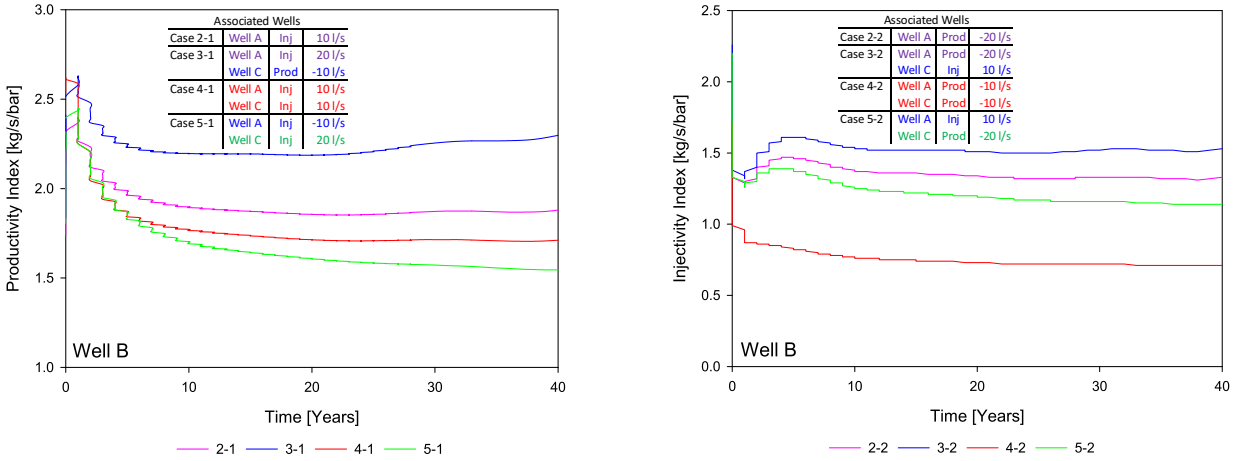

(a) **(b)**

Figure 42 – Well B _ Productivity and Injectivity Index

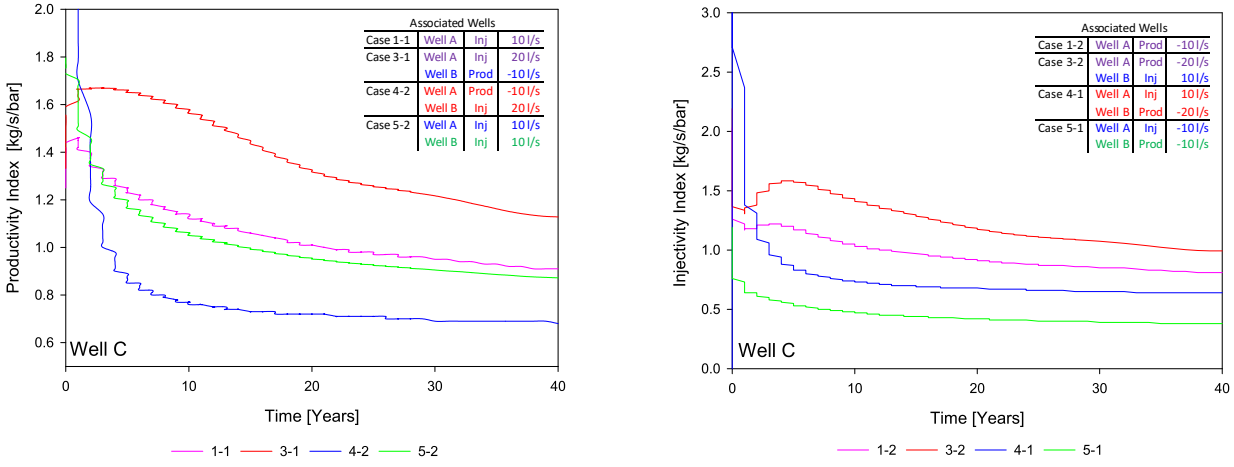

(a) **(b)**

Figure 43 – Well C _ Productivity and Injectivity Index

The radial diffusivity equation is introduced here to indicate how boundary effects affect the resulting Productivity Index. The pseudo-steady state flow is a flow regime that occurs in bounded (closed) reservoirs after the pressure transient has reached all its boundaries. This includes not only the case of physically bounded reservoirs but also the case of a well interfered by another well (e.g. Producer to producer).
For the pseudo steady-state flow condition, the Productivity Index is as follows, see Equation 18.

$$J = \frac{Q}{\overline{Pr} - P_{wf}} = \frac{k.h}{886.7\mu \left[ln\frac{r_e}{r_w} - \frac{3}{4} \right]} \tag{18}$$

Where r_e is the external radius [m], r_w is the wellbore radius [m], k is the matrix permeability in [mD], h is the net formation thickness [m], and μ is water viscosity [cp]. Has to be mentioned that "J" Productivity index, is not just $J \propto \frac{1}{(lnr_e - lnr_w)}$, also depends on the shape of the drainage-area geometry, here only a qualitative analysis of this aspect is made. If $\ln r_e$ is small, $\overline{Pr}$ a time after starting production will decrease, because of that, P_{wf} have to counteract this effect to meet the necessary ΔP_{dd}. This effect provoke that "J" decreases, because ΔP_{dd} final is bigger than ΔP_{dd} initial.

A closer look at Figures 41a and 41b , for example, point out that exist for Well A the possibility to get different values of Productivity and Injectivity indexes depending on the case. In particular in Case 3-2, which is the top energy producer (-20 l/s water with 137.5℃ (410.5 K) BHT), however, is not indeed the case in which the productivity is maximized. On the other hand, injectivity in Figure 42b and 43b depict the injectivity of the two injector wells associated to case 3-2. Those wells can be seen in the highest position in both Figures. The calculus of the Net Energy of the Geothermal Cycle has to consider the energy balance of produced vs consumed energy during the process of collecting geothermal energy.

The Figure 44 shows the position of the $\overline{Pr}$ observation points, borehole trajectories and their (production) injection points P_{wf}, the small fault and the relative magnitude of the permeabilities. This will be useful to better understand the evolution of the pressures. The brown horizontal surface in Figures 44a and 44b are also used in later figures as a reference depth to later compare different pressure values.

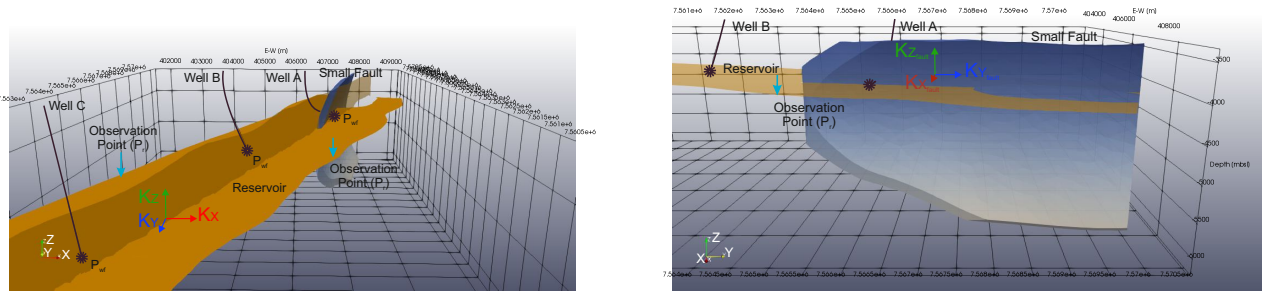

(a) **(b)**

Figure 44 – Observation and production (injection) points. The magnitude and direction of the permeabilities are shown here.

In reference to the Case 3-2 the following can be sustained.

(a) Well A has ↓J (Productivity) because r_e is small (Figure 41a)

This fact can be explained because the small fault in principle acts as a barrier reducing the volume to be initially drained ($K_y >> K_x)_{fracture}$. This is the connected volume by fractures in the X direction of the matrix. The P_{wf} has to decrease to keep the targeted rate of water, while $\overline{Pr}$ is partially kept by injection in Wells B and C, but in a lesser extent. So that ΔP_{dd} increases and "J" decreases ($Q = J.\left(\overline{Pr} - P_{wf}\right)$). Later, the pressure diffuses passing through and laterally the small fault, contacting a larger volume of the reservoir (See Figure 51).

(b) Well B has ↑J (Injectivity) with positive and negative r_e superposition effects (Figure 42b)

The effect of the contiguous Well C creates a barrier to the diffusion of the pressure in south direction, aditionally the effect of $K_{yMatrix} < K_{xMatrix}$ conducts the flux in direction to the flanks. By the contrary, in North direction, the drawdown pressure of the reservoir caused by Well A is helped by the Small Fault, which creates a short cut that diffuses the pressure, so that $P_{wf\,\text{Injection}}$ decreases. ΔP_{dd} decreases and "J" increases ($Q = J.\left(P_{wf} - \overline{Pr}\right)$). This observation corresponds to the principle of superposition, which indicates that the total pressure at each point in a reservoir is the sum of the pressure (drops) increments at that point caused by the (production) injection in each of the wells in the reservoir.

(c) Well C has ↑J (Injectivity),r_e superposition effects does not affect to much $\overline{Pr}$ (Figure 43b)

Well B creates a barrier for the diffusion of the pressure in direction to the North. Nevertheless, $\overline{Pr}$ continues decreasing, consequently $P_{wf\,\text{Injection}}$ decreases proportionally maintaining the desired water injection rate. So that, "J" increases ($Q = J.\left(P_{wf} - \overline{Pr}\right)$).

The Productivity and Injectivity indexes are not enough to show how ΔP_{dd} adapts itself to keep the (production) injection water rate as a constant. In Figures 45a to 50b an analysis of the $\Delta\overline{Pr}$, ΔP_{wf}, $\Delta(\Delta P_{dd})$ along the life of the project (Note: all the increments have been referred to the 1st year of production) is presented. These diagrams show the contribution of each pressure. Their derivatives $\frac{\delta\Delta\overline{Pr}}{\delta t}$ and $\frac{\delta\Delta P_{wf}}{\delta t}$ curves show the changes of slope which represent the evolution of the pressure in the radius of investigation as along it moves through the reservoir reaching their boundaries.

Graphs of $\Delta\overline{Pr}$, ΔP_{wf}, $\Delta(\Delta P_{dd})$ vs time and $\frac{\delta\Delta\overline{Pr}}{\delta t}$, $\frac{\delta\Delta P_{wf}}{\delta t}$ vs time

To illustrate the results a comparison of the potential difference between Case 3-2 and Case 5-2 was made. In these cases, production comes through a single well, these wells are located in the opposite extremes of the model (in case 3-2 is well A, in case 5-2 well C).
Special attention must be paid to the "cyan" curve, this represents the $\Delta(\Delta P_{dd})$. In case of the derivative curves, the gap between the "0 ordinate" and the black and the violet curve respectively are the remaining increments before to reach a constant value of pressure. The slope of the violet curve, indicated in ordinates, gives a qualitative idea of the imposed energy to meet the desired ΔP_{dd}.

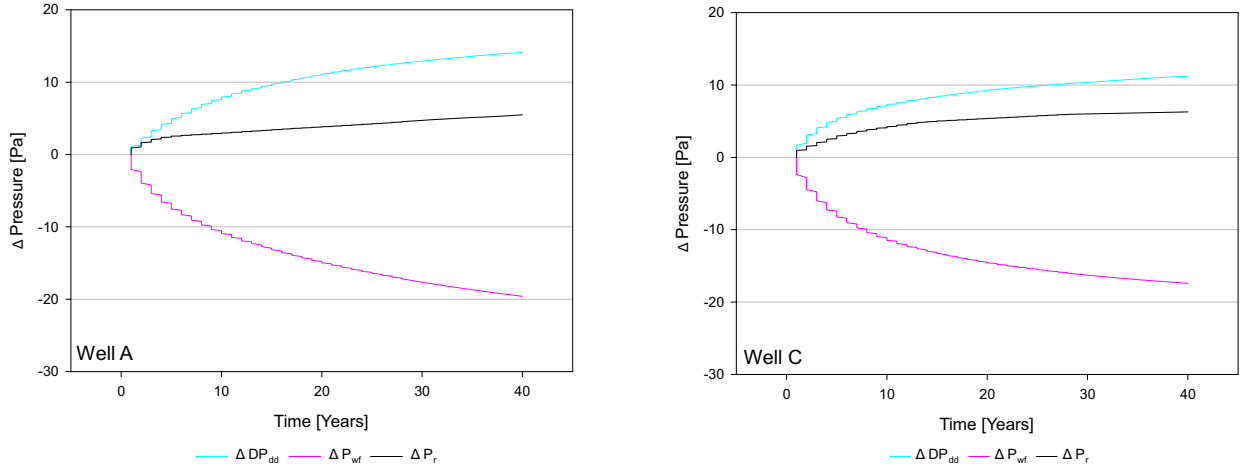

Figure 45 – $\Delta(\Delta P_{dd})$ evolution. Producers (a) Well A Case 3-2 and (b) Well C Case 5-2

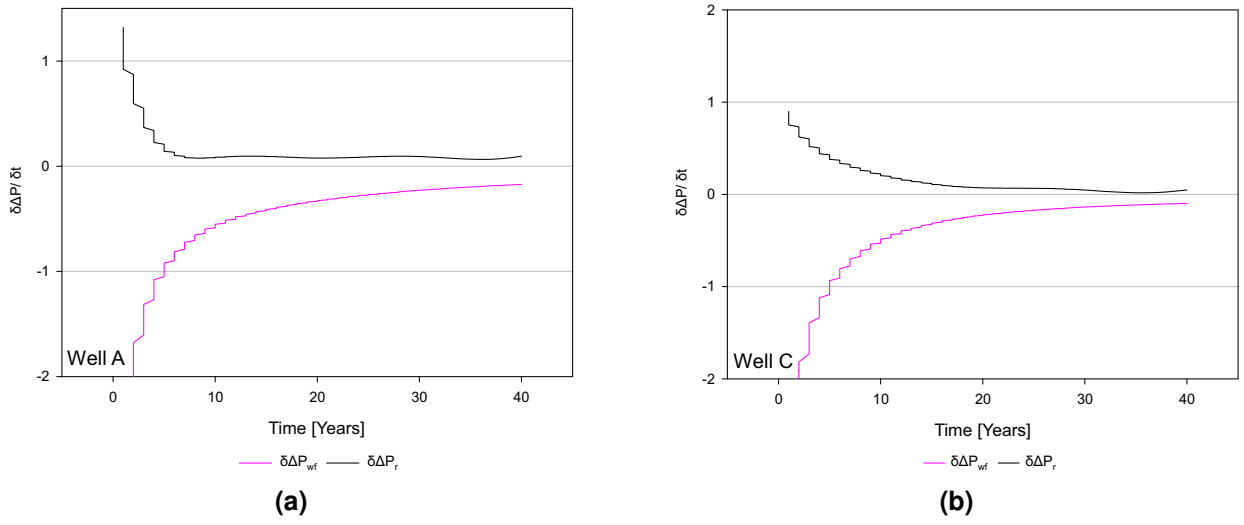

Figure 46 – $\frac{\delta \Delta P_{wf}}{\delta t}$ evolution. Producers (a) Well A Case 3-2 and (b) Well C Case 5-2

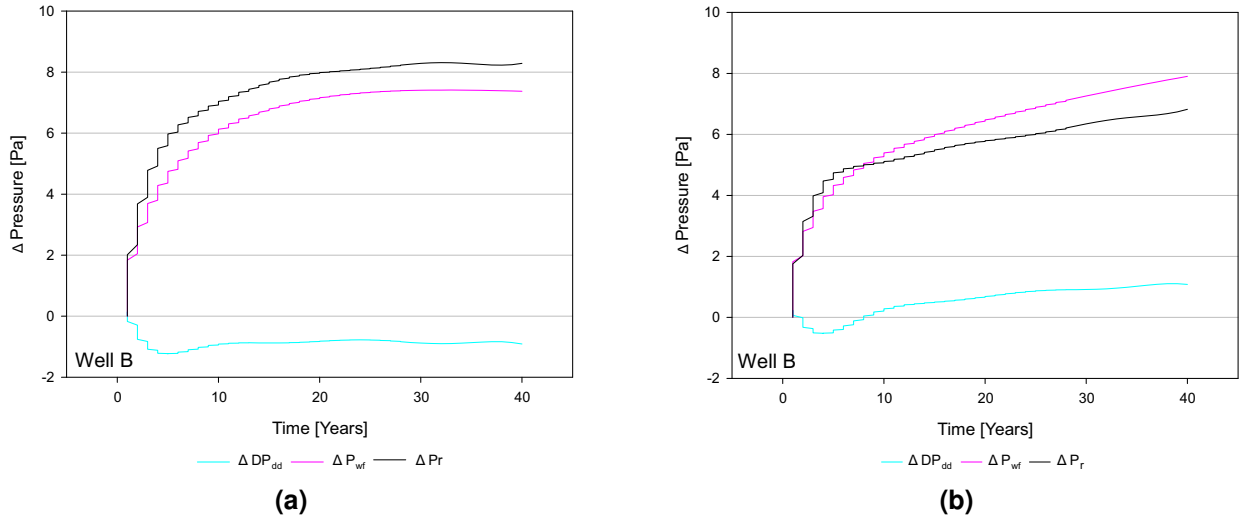

Figure 47 – $\Delta(\Delta P_{dd})$ evolution. Injectors (a) Well B Case 3-2 and (b) Well B Case 5-2

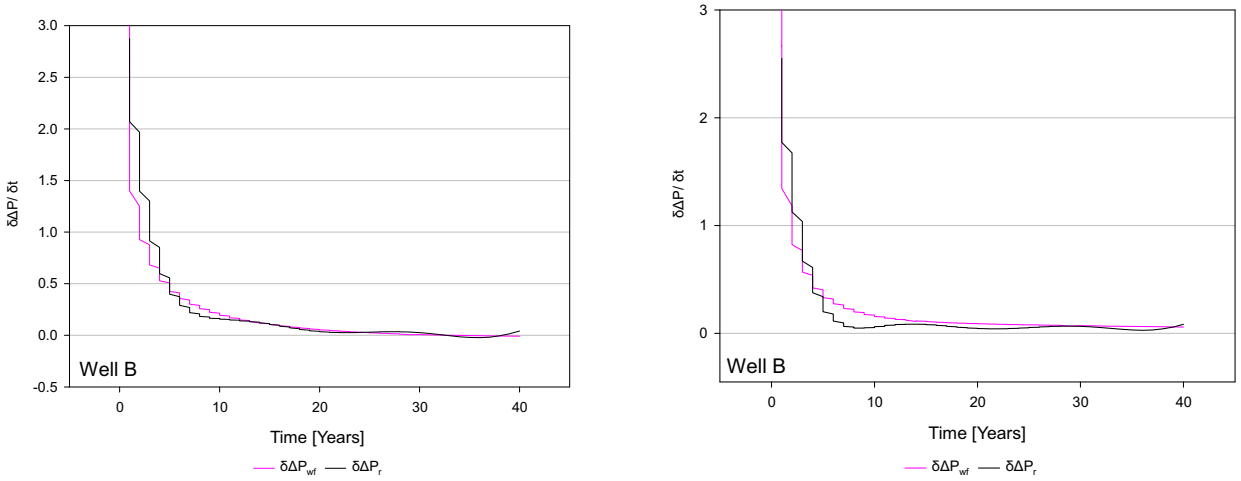

Figure 48 – $\frac{\delta \Delta P_{wf}}{\delta t}$ evolution. Injectors (a) Well B Case 3-2 and (b) Well B Case 5-2

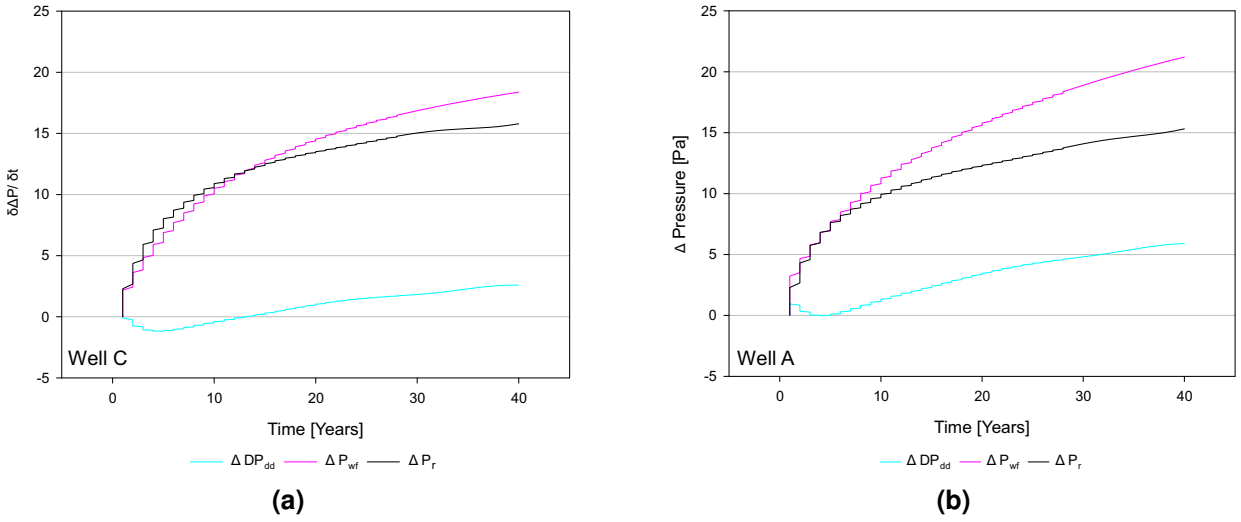

Figure 49 – $\Delta(\Delta P_{dd})$ evolution. Injectors (a) Well C Case 3-2 and (b) Well A Case 5-2

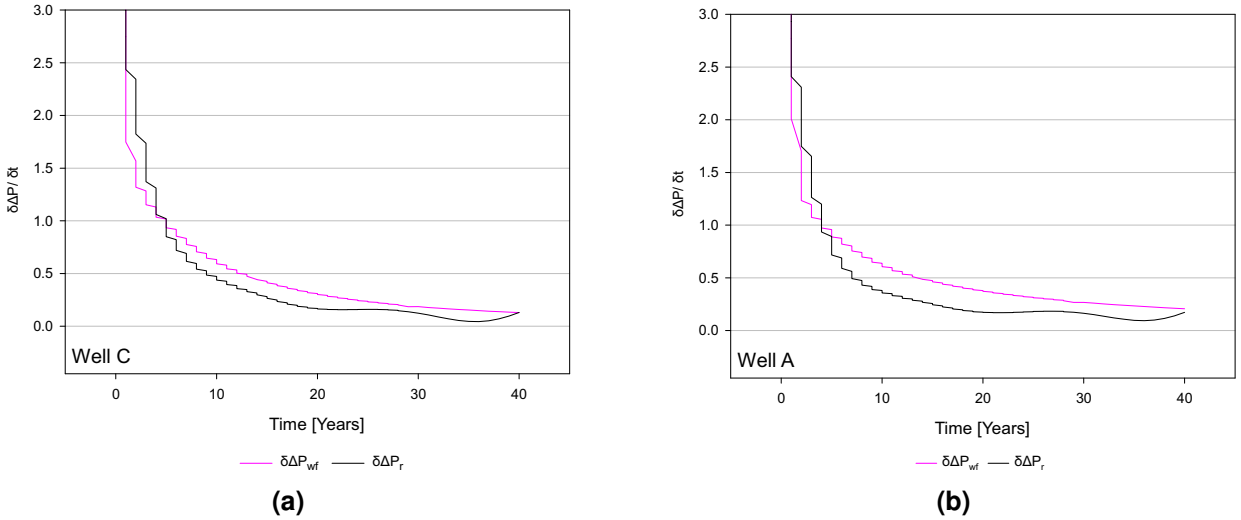

Figure 50 – $\frac{\delta \Delta P_{wf}}{\delta t}$ evolution. Injectors (a) Well C Case 3-2 and (b) Well A Case 5-2

In Figure 47a $\Delta(\Delta P_{dd})$ falls below 0 Pa, the reason for this is that the $\overline{Pr}_{re}$ is bigger than the pressure inside by the channel of low pressure which connects Well B, Small Fault and Well A. The production rate of Well A is twice as high as the injection rate in Well B. In addition, the completion of Well B is structurally in a higher position than the completion of Well A, so that gravitational forces help directing water from the injector to the producer. Figure 49b also indicates that ΔP_{wf} has increased more than in Figure 49a, meaning that more energy is consumed.

Streamlines

The Open-Source Paraview multi-platform data analysis was used to visualize streamlines. The figures 54 to 53 show the peculiarities in the flow pattern of cases 3-2 and 5-2, which complement the previous analysis. The streamlines are colored according to the flux velocity. The time the streamlines are plotted corresponds to the end of the simulation (40 years).

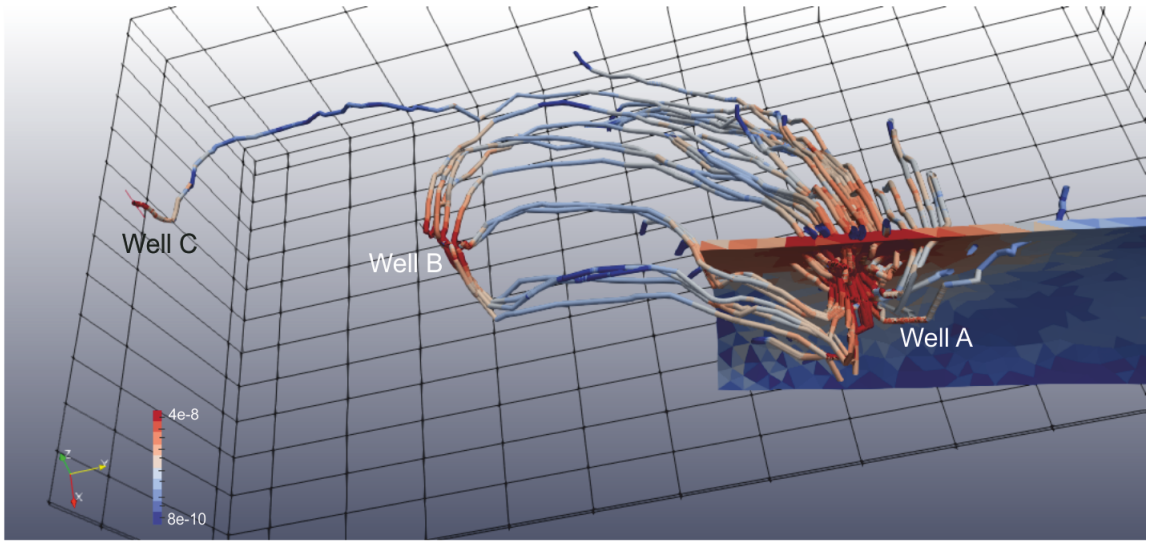

Figure 51 – Plan view. Steamlines _ Well A3-2 _ Producer.

Case 3-2 Well A. $\Delta P_{wf\,\text{Production}}$ increases because the restriction caused by the Small Fault. This fact can be observed in Figure 45a compared with Figure 45b. The auxiliary figures 46a and 46b show that in the Case 3-2, where water is produced near to the Small Fault, the spent energy is bigger than in Case 5-2 Well C. This smaller consume is showed in Figure 46b, where the 0 slope reference and the pink curve are close one to each other.

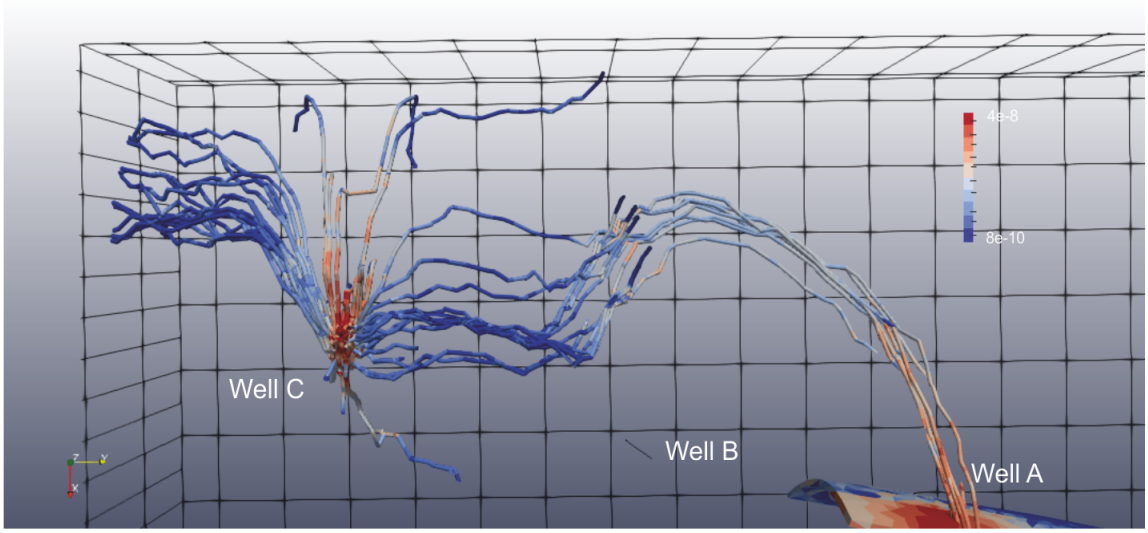

Figure 52 – Plan view. Steamlines _ Well C3-2 _ Injector.

Case 3-2 Well C. Water that comes from this well has no major difficulties to overcome the pressure barrier-effect exerted by the Well B (injector). This fact will be seen in Figure 53. Water from Well C, goes around it and finally meets the high permeability path created by natural fractures perpendicularly to the axis of the anticline, from the flank to the hinge, where the Small Fault is located.

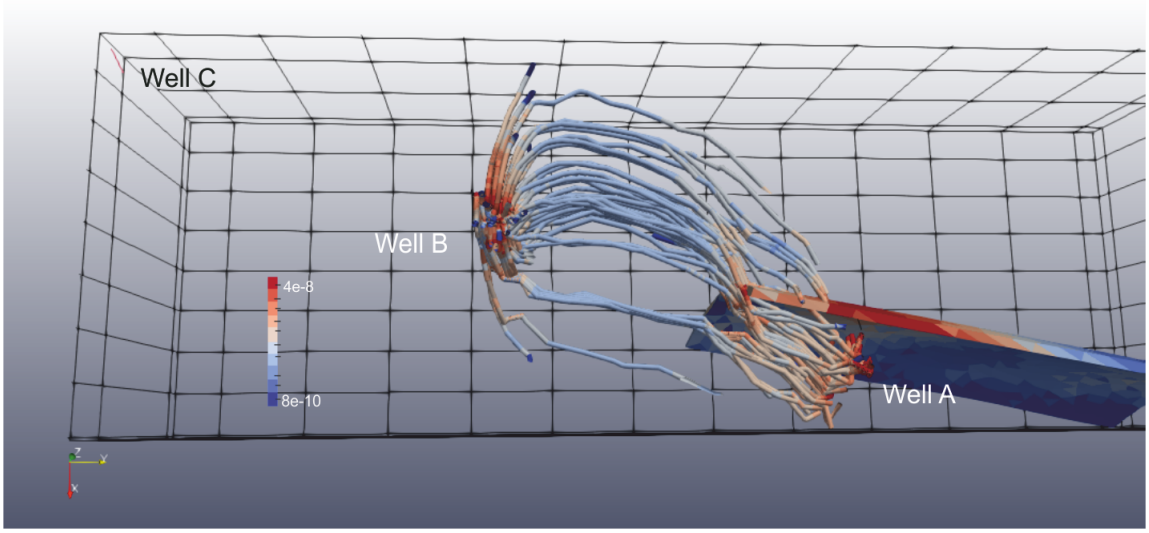

Figure 53 – Steamlines _ Well B3-2 _ Injector.

Case 3-2 Well B. streamlines goes direct to the Small Fault and some of them directly to the Well A (producer). This direct connection was previously mentioned and is the reason why Figure 47a shows that $\Delta P_{wf\,\text{Injection}}$ remains lower than in Figure 47b. In Figure 56 the behaviour of the streamlines is characterized by not finding a direct connection with Well C.

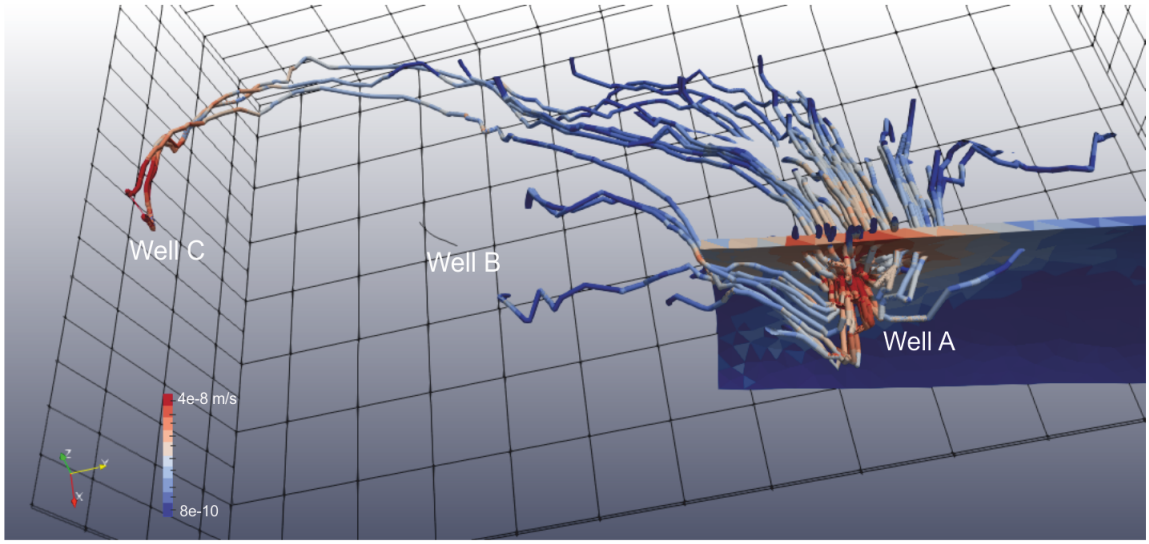

Figure 54 – Plan view. Steamlines _ Well A5-2 _ Injector.

Case 5-2 Well A. This image shows high-speed streamlines near Well A, which runs through a small area to the Small Fault. Behind the small fault, a larger area is affected, where later the streamlines slow down. This restriction makes that $\Delta P_{wf\,\text{Injection}}$ spent on inject increases. The colors in the small fault indicate fluid movement.

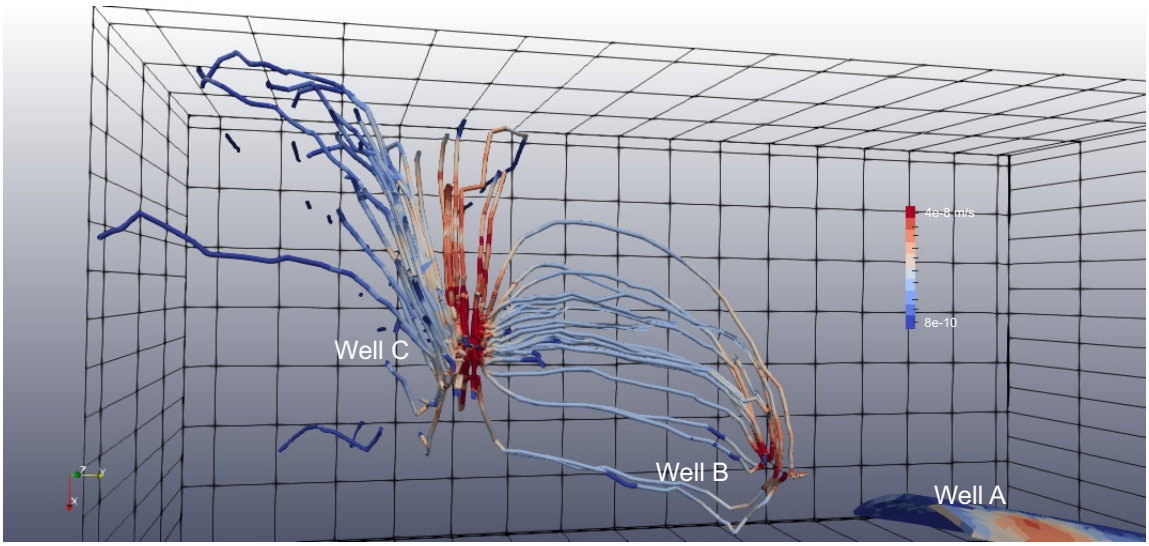

Figure 55 – Plan view. Steamlines _ Well C5-2 _ Producer.

Case 5-2 Well C. $\Delta P_{wf\,\text{Production}}$ has no restrictions to the water-flux, so that pressure diffuses along the fractures in direction to the flanks. Later, water arrives coming from Well B and A, as can be seen in this figure and in Figure 54.

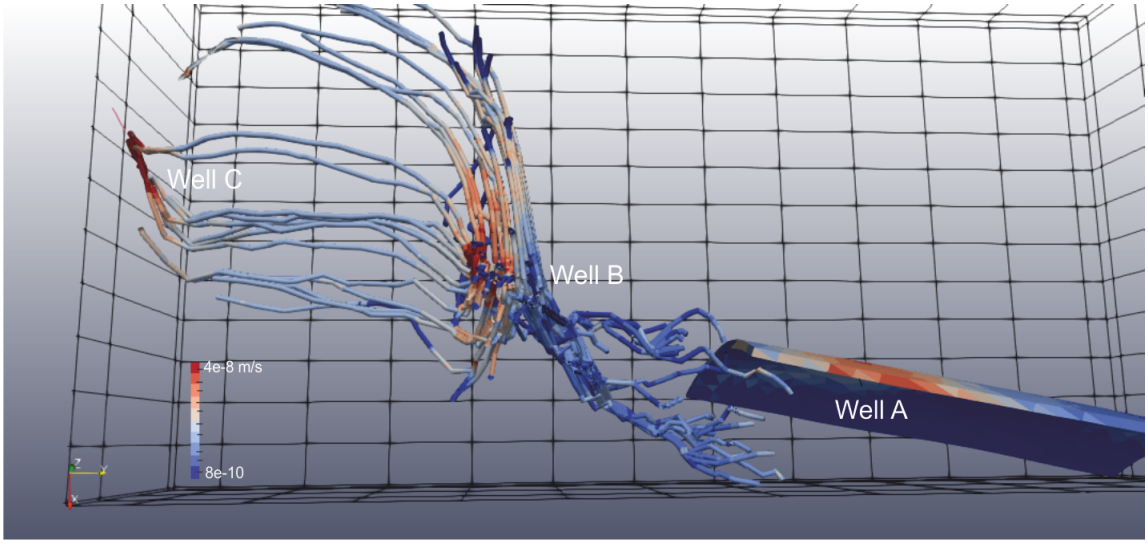

Figure 56 – Plan view. Steamlines _ Well B5-2 _ Injector.

Case 5-2 Well B. The streamlines coming out from the Well $B_{Injector}$ diffunds first in direction to the flanks and later in direction to the Well $C_{Productor}$.

Different arrangements of (injection) production, for the wells A, B and C.

Case 3-2 will be compared with the Case 4-1. Case 4-1 consist also of one producer and two injection wells. Figures 57 to 64 will depict how the volume of rock around the producer wells changes their temperature an pressure values. The temperature and pressure change was calculated as the difference in absolute values between the start of the simulation, the next 7 years and the end of the simulation.

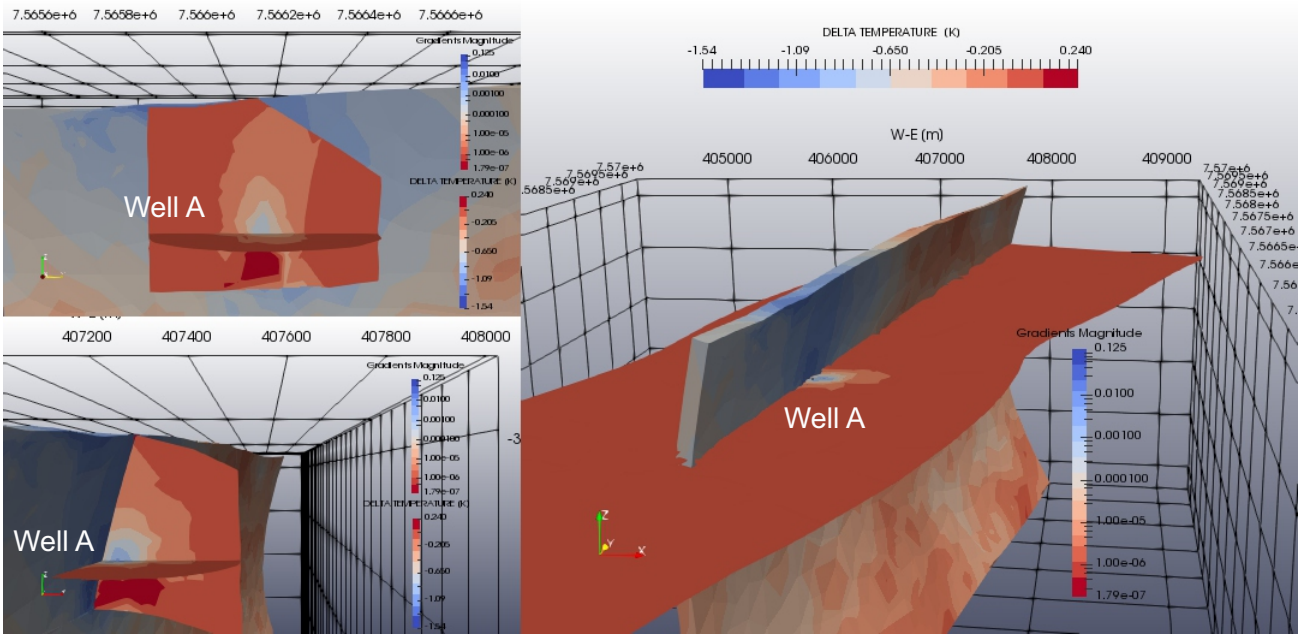

Figure 57 – Well A3-2 _ Producer _ ΔTemperature from 0 to 7 years

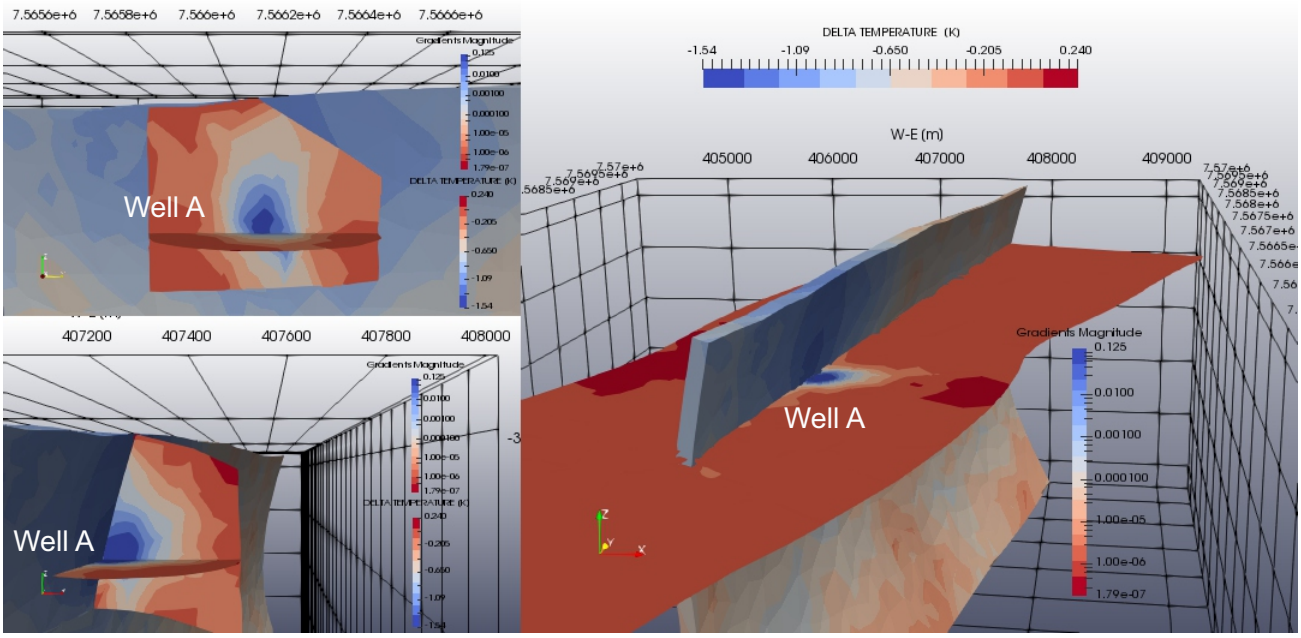

Figure 58 – Well A3-2 _ Producer _ ΔTemperature from 7 to 40 years.

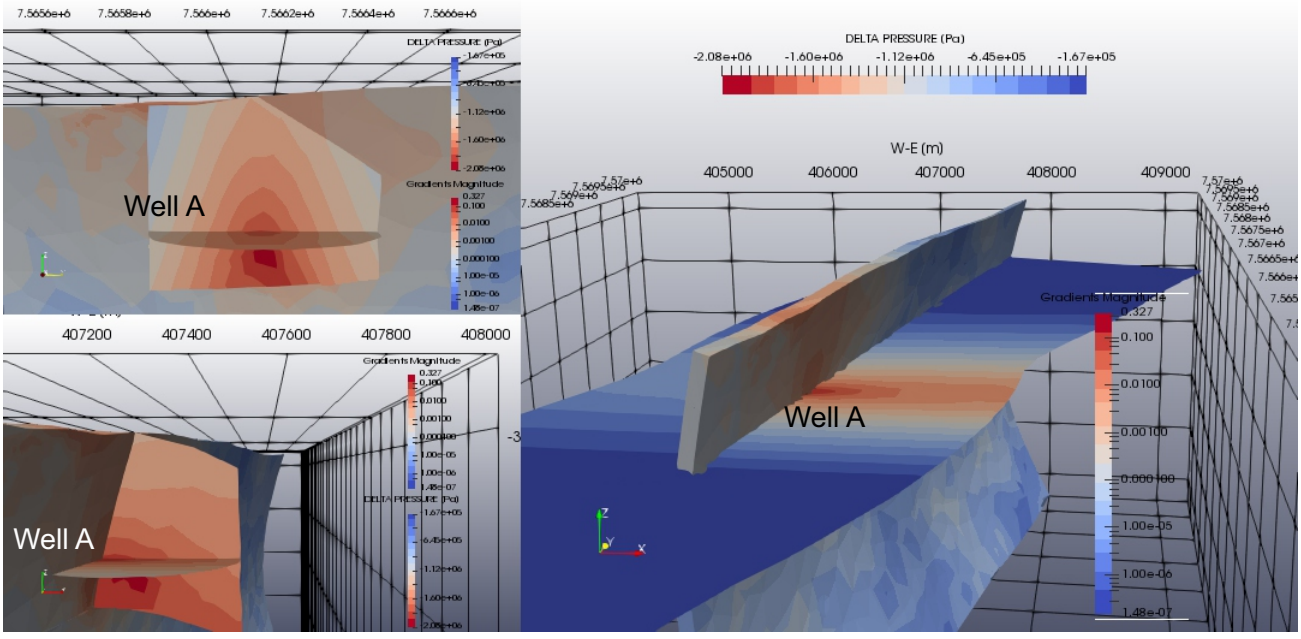

Figure 59 – Well A3-2 _ Producer _ ΔReservoir Pressure from 0 to 7 years

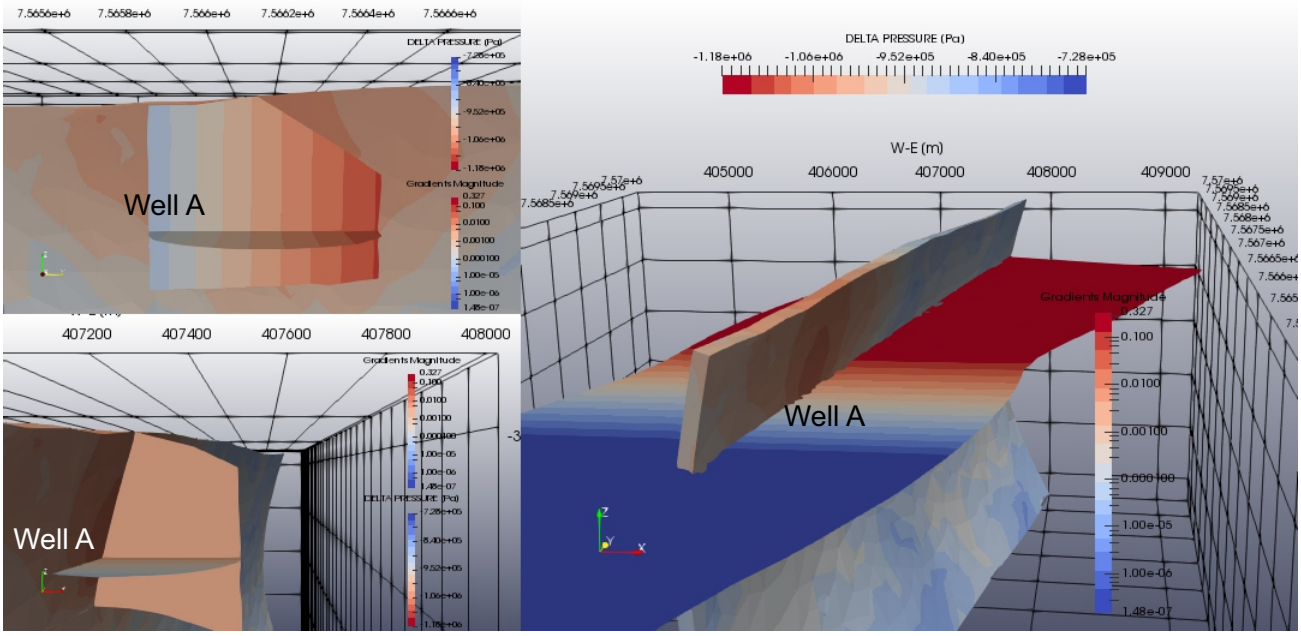

Figure 60 – Well A3-2 _ Producer _ ΔReservoir Pressure from 7 to 40 years

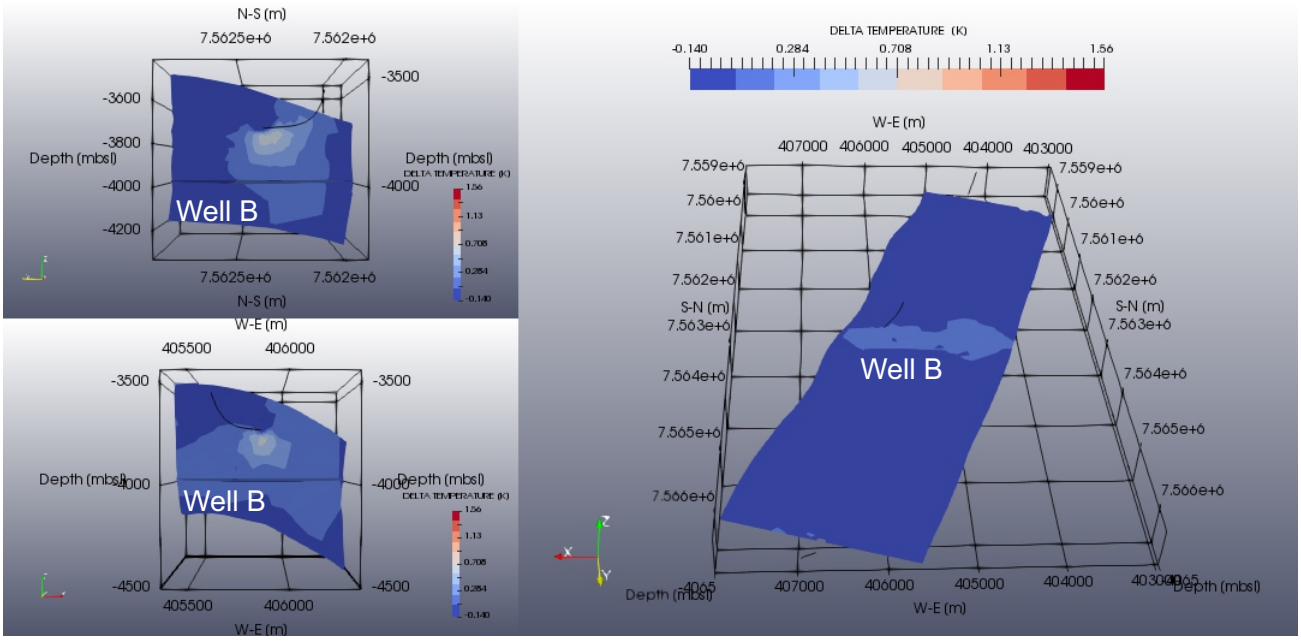

Figure 61 – Well B4-1 _ Producer _ ΔTemperature from 0 to 7 years

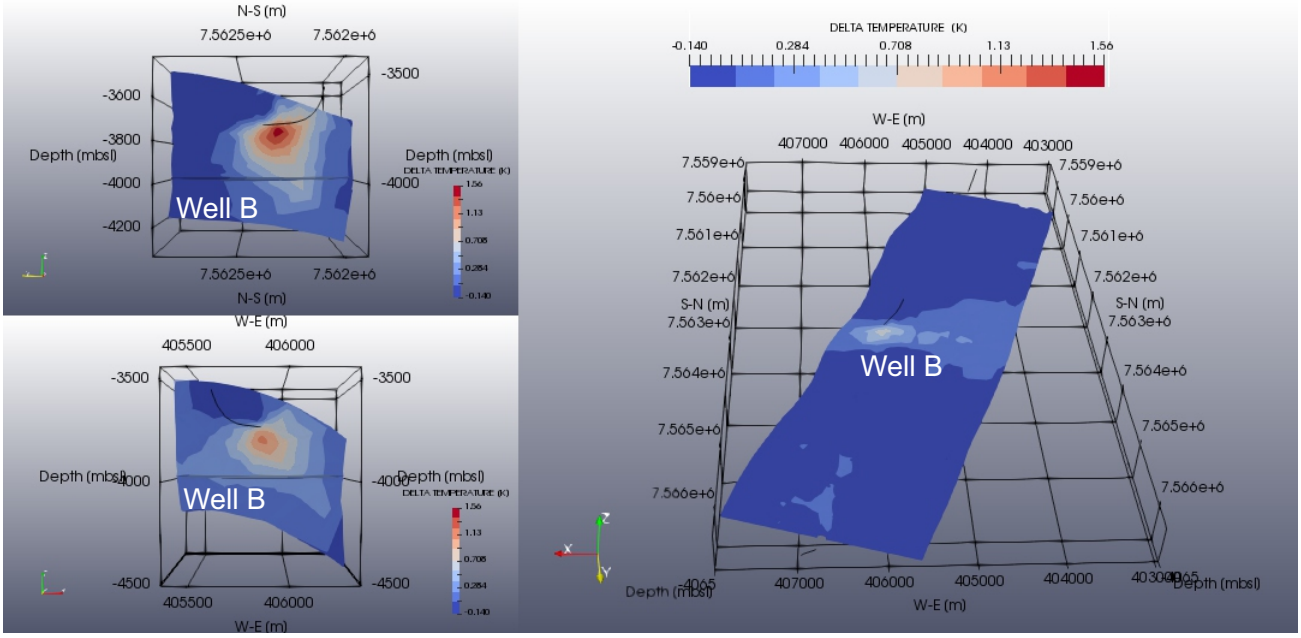

Figure 62 – Well B4-1 _ Producer _ ΔTemperature from 7 to 40 years

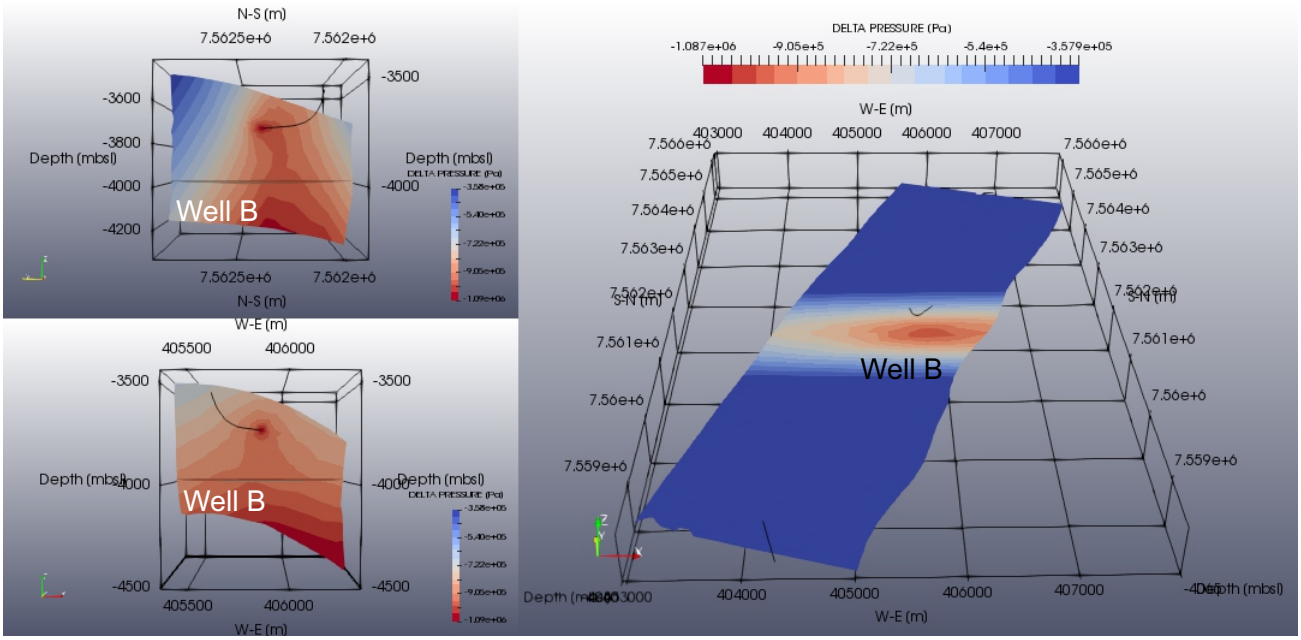

Figure 63 – Well B4-1 _ Producer _ ΔReservoir Pressure from 0 to 7 years

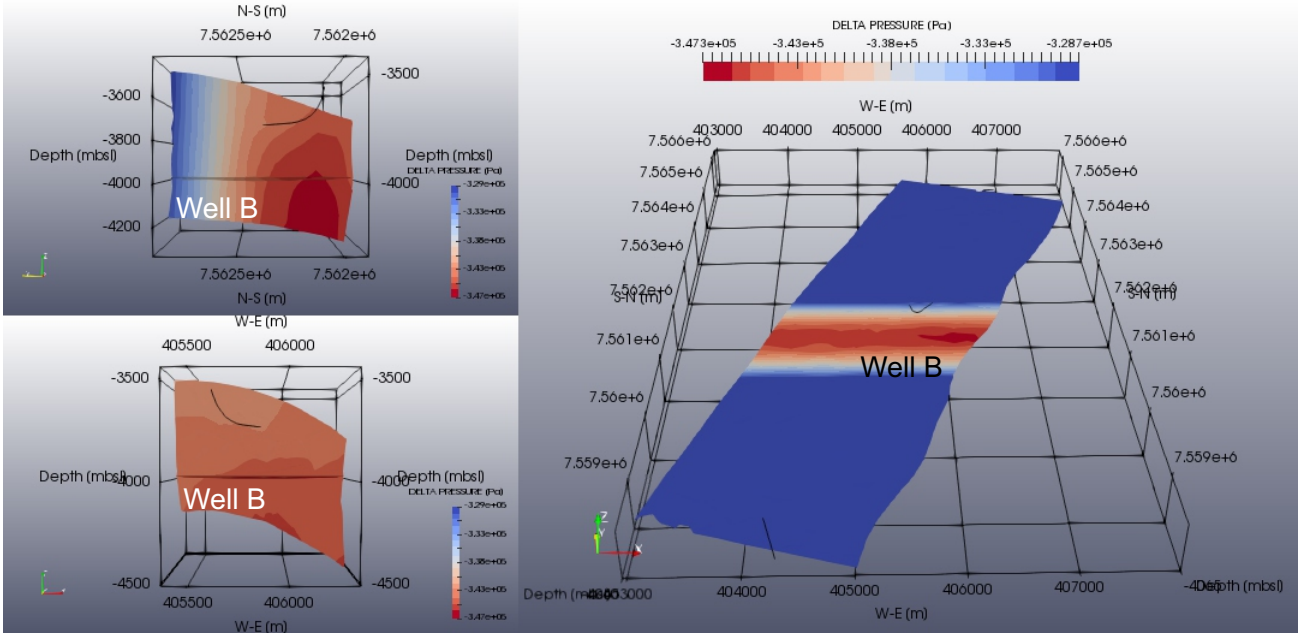

Figure 64 – Well B4-1 _ Producer _ ΔReservoir Pressure from 7 to 40 years

Well A locates its completion at 5147 m TVD, Well B has its completion located at 4764 m TVD, and Well C at 5047 m TVD. The difference in the placement of the suction point affects their performance. In B4-1, convective effects later supply it hotter water from deeper positions inside the reservoir as can be seen in Figure 64. In Figure 59 on the other hand, seems that water comes from the upper part of the reservoir, helped by the vertical enhanced permeability given by the small fault.

7 Performance of the geothermal cycle

Until now, the useful energy used to move fluids into the reservoir has been considered. Energy consumption depends on how difficult it is to produce or inject. The difficulties arise when the barrier to the diffusion of the pressure are present (faults, permeability heterogeneities, and well to well interferences). Equation 18 better explains this fact better.

The energy expenditure on the geothermal cycle, beyond the movement of fluids in the reservoir, dues to the fluid pressure losses along the wellbore, as well as due to the conversion of thermal energy into usable energy at the surface.

Two specialized tools have been used to calculate, first the fluid flow behavior through the wellbore, second the production of useful energy. In order, both WellboreKIT and GESI simulation results will be presented.

7.1 Heat losses in the wellbore

Calculus of the dynamic WHT and WHP with WellboreKIT

The results obtained from WellboreKIT are the following. For more details about WellboreKIT see Appendix C. Vertical lift performance and their temperature variation are presented for every producer well.

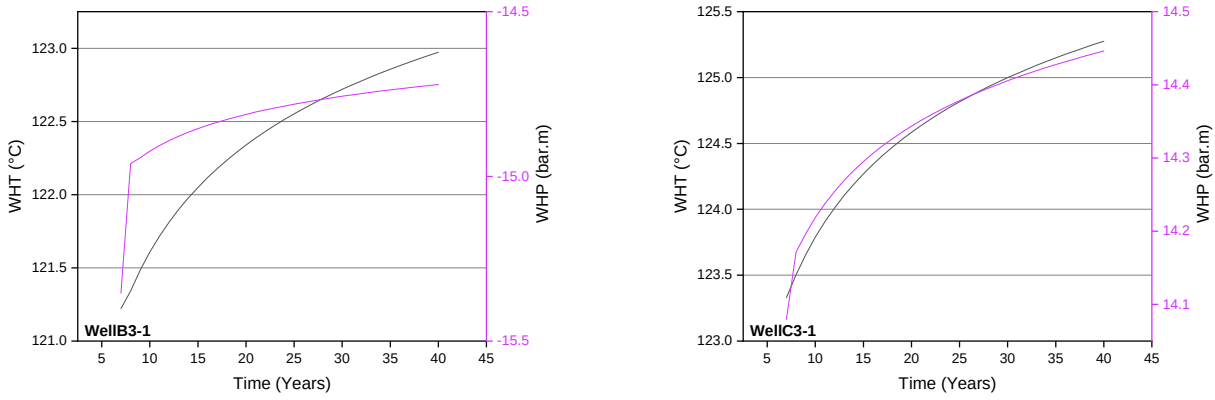

Figure 65 – WHT and WHP of Well B3-1 and Well C3-1

Well B3-1. TEMPERATURE: $BHT_{avg.}$= 129.3 ℃, $BHT_{max.}$= 129.7 ℃, $BHT_{min.}$= 129.2 ℃, Δ $BHT_{max.}$= 0.46 ℃, Δ $BHT_{1yr\text{-}40yr}$= -0.24 ℃. PRESSURE: $BHP_{avg.}$= 457.9 bar.m, $BHP_{max.}$= 462.8 bar.m, $BHP_{min.}$= 457.2 bar.m, Δ BHP= 5.52 bar.m.

Well C3-1. TEMPERATURE: $BHT_{avg.}$= 131.6 ℃, $BHT_{max.}$= 134.2 ℃, $BHT_{min.}$= 131.5 ℃, Δ $BHT_{max.}$= 2.74 ℃, Δ $BHT_{1yr\text{-}40yr}$= 1.27 ℃. PRESSURE: $BHP_{avg.}$= 478.0 bar.m, $BHP_{max.}$= 488.6 bar.m, $BHP_{min.}$= 472.6 bar.m, Δ BHP= 16.06 bar.m.

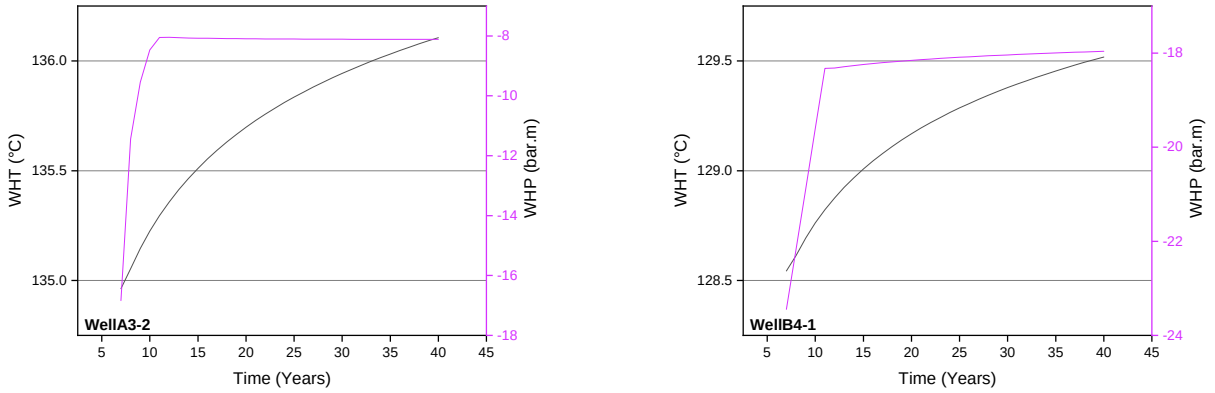

Figure 66 – WHT and WHP of Well A3-2 and Well B4-1

Well A3-2. TEMPERATURE: $BHT_{avg.}$= 137.4 ℃, $BHT_{max.}$= 137.7 ℃, $BHT_{min.}$= 136.9 ℃, Δ $BHT_{max.}$= 0.79 ℃, Δ $BHT_{1yr\text{-}40yr}$= 0.64 ℃. PRESSURE: $BHP_{avg.}$= 471.9 bar.m, $BHP_{max.}$= 496.0 bar.m, $BHP_{min.}$= 464.9 bar.m, Δ BHP= 31.04 bar.m.

Well B4-1. TEMPERATURE: $BHT_{avg.}$= 130.1 ℃, $BHT_{max.}$= 130.6 ℃, $BHT_{min.}$= 129.8 ℃, Δ $BHT_{max.}$= 0.75 ℃, Δ $BHT_{1yr\text{-}40yr}$= -0.56 ℃. PRESSURE: $BHP_{avg.}$= 449.0 bar.m, $BHP_{max.}$= 461.3 bar.m, $BHP_{min.}$= 446.9 bar.m, Δ BHP= 14.32 bar.m.

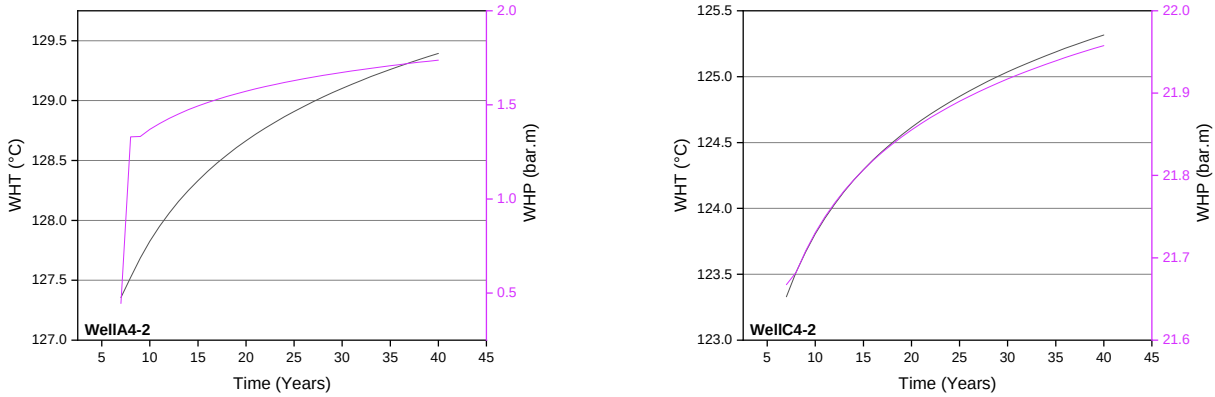

Figure 67 – WHT and WHP of Well A4-2 and Well C4-2

Well A4-2. TEMPERATURE: $BHT_{avg.}$= 137.6 ℃, $BHT_{max.}$= 137.7 ℃, $BHT_{min.}$= 137.3 ℃, Δ $BHT_{max.}$= 0.33 ℃, Δ $BHT_{1yr\text{-}40yr}$= 0.13 ℃. PRESSURE: $BHP_{avg.}$= 489.8 bar.m, $BHP_{max.}$= 496.0 bar.m, $BHP_{min.}$= 489.6 bar.m, Δ BHP= 6.36 bar.m.

Well C4-2. TEMPERATURE: $BHT_{avg.}$= 131.6 ℃, $BHT_{max.}$= 134.3 ℃, $BHT_{min.}$= 131.5 ℃, Δ $BHT_{max.}$= 2.77 ℃, Δ $BHT_{1yr\text{-}40yr}$= 1.29 ℃. PRESSURE: $BHP_{avg.}$= 485.5 bar.m, $BHP_{max.}$= 488.6 bar.m, $BHP_{min.}$= 485.0 bar.m, Δ BHP= 3.61 bar.m.

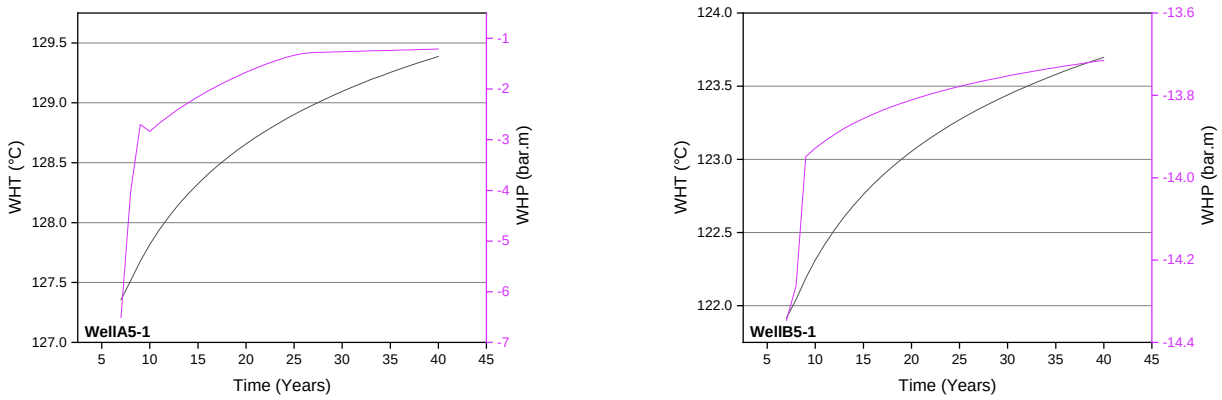

Figure 68 – WHT and WHP of Well A5-1 and Well B5-1

Well A5-1. TEMPERATURE: $BHT_{avg.}$= 137.6 ℃, $BHT_{max.}$= 137.7 ℃, $BHT_{min.}$= 137.3 ℃, Δ $BHT_{max.}$= 0.33 ℃, Δ $BHT_{1yr\text{-}40yr}$= 0.13 ℃. PRESSURE: $BHP_{avg.}$= 482.8 bar.m, $BHP_{max.}$= 496.0 bar.m, $BHP_{min.}$= 475.7 bar.m, Δ BHP= 20.25 bar.m.

Well B5-1. TEMPERATURE: $BHT_{avg.}$= 129.8 ℃, $BHT_{max.}$= 130.2 ℃, $BHT_{min.}$= 129.7 ℃, Δ $BHT_{max.}$= 0.47 ℃, Δ $BHT_{1yr\text{-}40yr}$= 0.07 ℃. PRESSURE: $BHP_{avg.}$= 458.6 bar.m, $BHP_{max.}$= 462.8 bar.m, $BHP_{min.}$= 457.1 bar.m, Δ BHP= 5.73 bar.m.

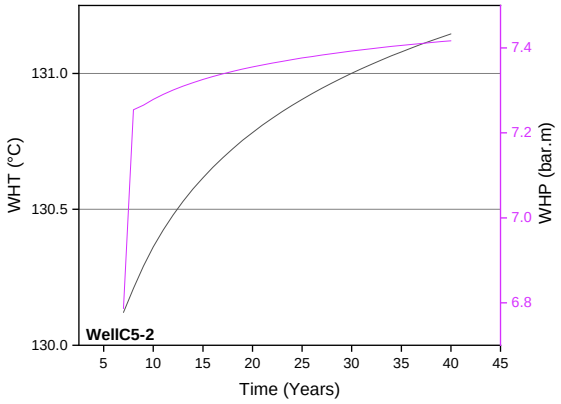

Figure 69 – WHT and WHP of Well C5-2

Well C5-2. TEMPERATURE: $BHT_{avg.}$= 131.8 ℃, $BHT_{max.}$= 134.3 ℃, $BHT_{min.}$= 131.5 ℃, Δ $BHT_{max.}$= 2.76 ℃, Δ $BHT_{1yr\text{-}40yr}$= 0.23 ℃. PRESSURE: $BHP_{avg.}$= 470.0 bar.m, $BHP_{max.}$= 488.6 bar.m, $BHP_{min.}$= 465.3 bar.m, Δ BHP= 23.34 bar.m.

All values of Δ $BHT_{1yr\text{-}40yr}$ were measured between the first year of production and the 40th year. These values indicate that the wells were in a cooling process throughout their life, with the exception of wells B4-1, B3-1 and B2-1, whose BHT has increased by about one degree. This can be seen in the Figures 62 and 64. It is possible to observe how the Well B pressure

drops in the vertical direction and sucks water from the deeper part of the reservoir.
In the previous Figures 69, 66b and 66a it can be seen that WHT changes are on the order of one degree (in accordance with the water production rate of 10 l/s for the first and 20 l/s for the second). Simulations were performed by setting an average BHT as a reference (this was possible because the temperature variation is on the order of two degrees throughout the productive life of the project).

7.2 Production of useful energy

ORC-Process simulation with GESI (GEothermal SImulation)

The simulation software GESI is a Matlab® based software. This software can calculate Gross and Net power, besides the efficiency of the conversion. For more details about GESI see Appendix D.
Since GESI can use a variety of working fluids for their calculations, propane (IUPAC C3H8) was selected for its low price and availability at the Campo Duran refinery near Macueta Field (90 km).
Because of the precision of the data set introduced to the GESI, calculus made here will roughly indicate the order of magnitude of the Power able to be generated. Sensibilities to the wellhead temperature have not been performed.

The results of GESI after 30 years of production are listed in the table 15. WHT from the WellboreKIT was used as input values. (Dif) is the power needed to move the working fluid through the ORC−Process.

Cases	WHT [℃]	Net [KWe]	Gross [KWe]	Dif [KWe]
B3-1	122.7	375.5	467.3	91.8
C3-1	125.0	416.8	518.7	101.9
A3-2	135.9	603.0	750.4	147.4
A4-1	129.4	493.9	614.7	120.8
A4-2	129.1	489.2	608.8	119.6
C4-2	125.0	417.8	520.0	102.2
A5-1	129.1	489.1	608.7	119.6
B5-1	123.4	388.6	483.7	95.0
C5-2	131.0	521.8	649.4	127.6

Table 15 – Net and Gross values of KWe calculated with GESI.

7.3 Energy Output

The amount of energy consumed in the geothermal cycle was roughly calculated. To compare the simulated cases, the main energy expenditure was divided into four main groups.

(a) Water production.

Was considered the $P_{wf\,\text{Production}}$ calculated with the OpenGeoSys + or - (depends on the case) the difference with the output of WellboreKit. The output of WellboreKit takes as boundary condition an average value of BHP (during the productive time of the well) and gives as result WHP that changes due to changes in temperature in the near wellbore along its productive life. Finally, as a target pressure at the inlet point of the ORC a pressure of 25 bar.m was required. The needed pressure to reach this point also comes from the pump installed in the well. For this exercise was assumed the utilisation of Electro Submersible Pumps (ESP). The amount of energy calculated in this process is useful energy, but losses involved has to be considered. According to the experience in operation, a value of three can be used as correction factor BID (2011) and Forero and Caicedo (2016) . This correction factor has made three times bigger the calculated pumping energy for each complete case.

(b) Water injection.

As in the water production, in the water injection analysis the $P_{wf\,\text{Injection}}$ was considered as the useful energy spent. A factor of three corrects the final result to obtein the total amount of energy involved in the injection process. See BID (2011) for more details related to the calculus of efficiency of the pumping system and friction losses.

(c) Thermal losses by conduction in the wellbore.

As was calculated with the WellboreKit, the difference of temperature in between BHT and WHT, depends on the production rate. In each case was calculated the Geothermal Power (KWt) either at the bottom hole and at the wellhead as well. The difference represents the amount of thermal energy lost through conduction to the near wellbore. This value later was affected by the efficiency of the thermal-electrical conversion obtained from the ORC (which depends on the considered case).

(d) Surface Operation

The Operation of the ORC-Process involves the use of peripheral devices that consume energy. All those devices are included in the calculus of GESI (e.g. pump which moves the working fluid from the condenser to the interchanger).

As was published ”Optimization of Electric Energy Consumption in Marginal California Oilfields” by Klein (2003) in page 4-2, can be expected a distribution of the electric power consumption, in this particular field, in Fluids Production (55.3%), Water Injection (26.4%) and surface operation of (18.3%). The Power sharing observed through the calculus made for Macueta Field has pointed out a different situation. In the Macueta case, power sharing depends on the feasibility to inject or produce almost at the same extent. It is important to remark, that in the oil field industry depleted zones are used to inject (even those are used for seepage of fluids in general or for secondary recovery of oil), sometimes water conformance has to be improved to counteract against the action of a ”thief zone”. To cope with the ”voidage replacement ratio”, a large amount of water from lakes and rivers is normally used. In a Geothermal Project to ensure a closed cycle

of the injected water is a key aspect. Injectivity in the geothermal industry cannot be assumed as high as in the petroleum industry.
Friction losses are related with the rate of production, diameter and roughness of the tubing. All the cases have the same completion and the only variable parameter is water rate of production. For the different cases can be observed different values of $P_{wf\,\text{Production}}$, but in general terms, exist a marked difference in between the wells that produce 20 l/s, in comparison with the sum of both 10 l/s together. This effect partially compensates the advantage obtained because of the smaller thermal losses by conduction across the wellbore.

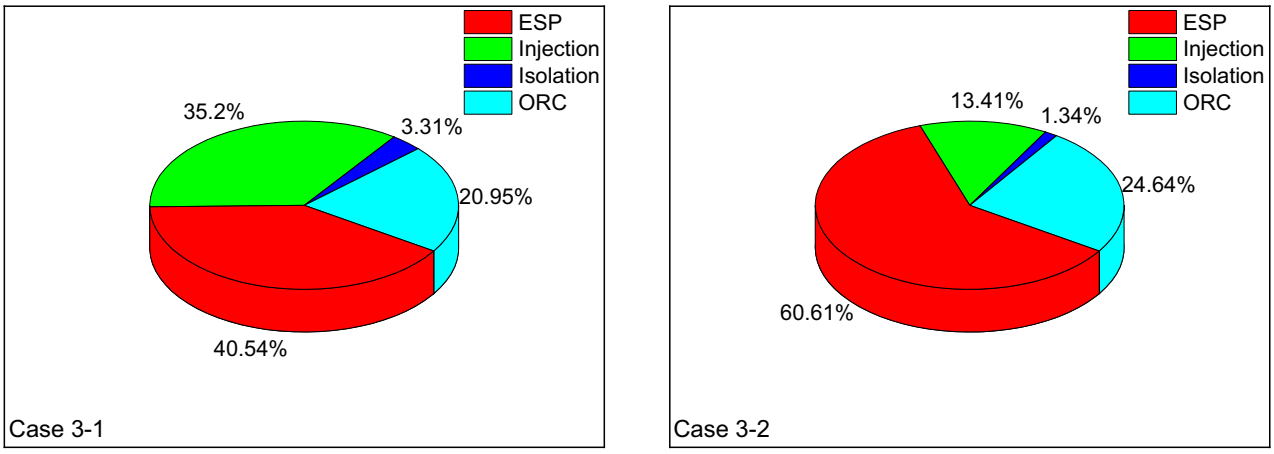

(a) **(b)**

Figure 70 – Power consumed in the Geothermal cycle _ Cases 3-1 and 3-2

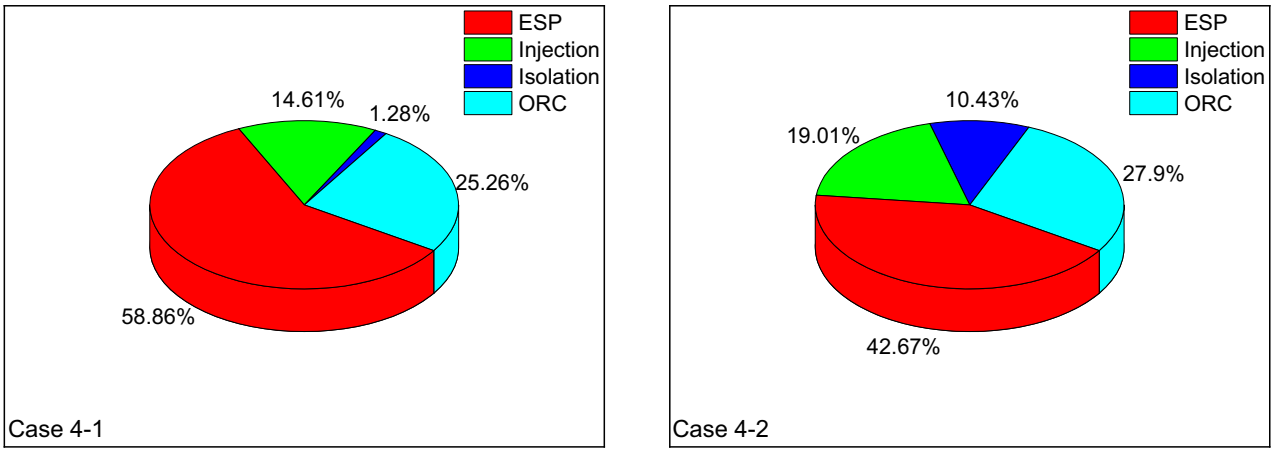

(a) **(b)**

Figure 71 – Power consumed in the Geothermal cycle _ Cases 4-1 and 4-2

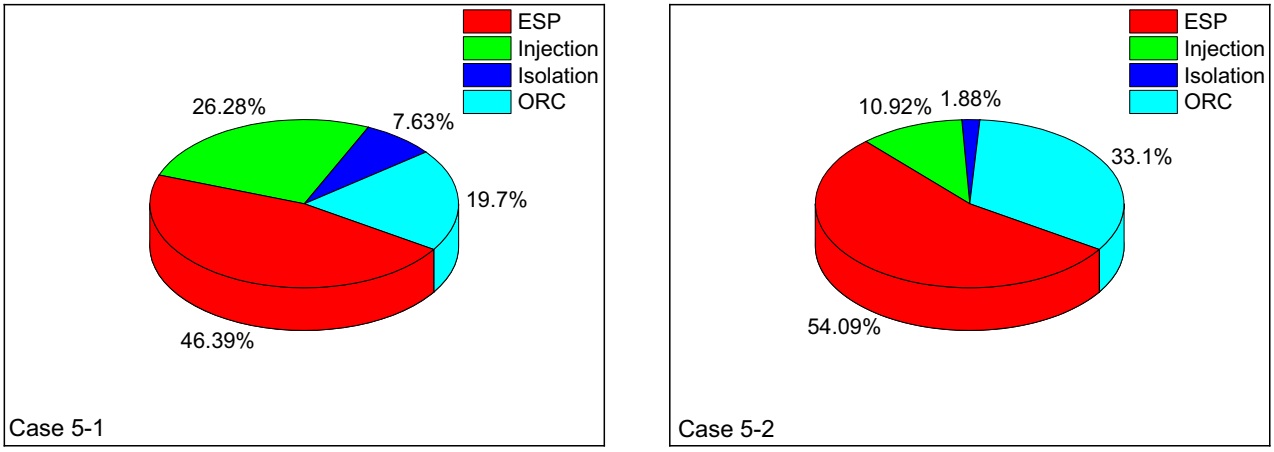

Figure 72 – Power consumed in the Geothermal cycle _ Cases 5-1 and 5-2

Power balances and efficiencies of the geothermal cycle

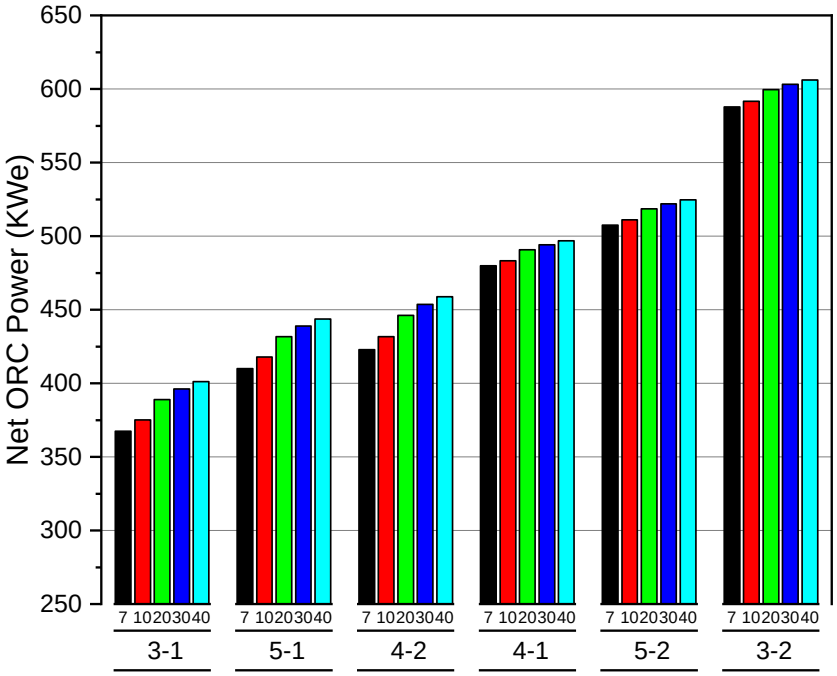

Figure 73 – Net ORC Power (KWe)

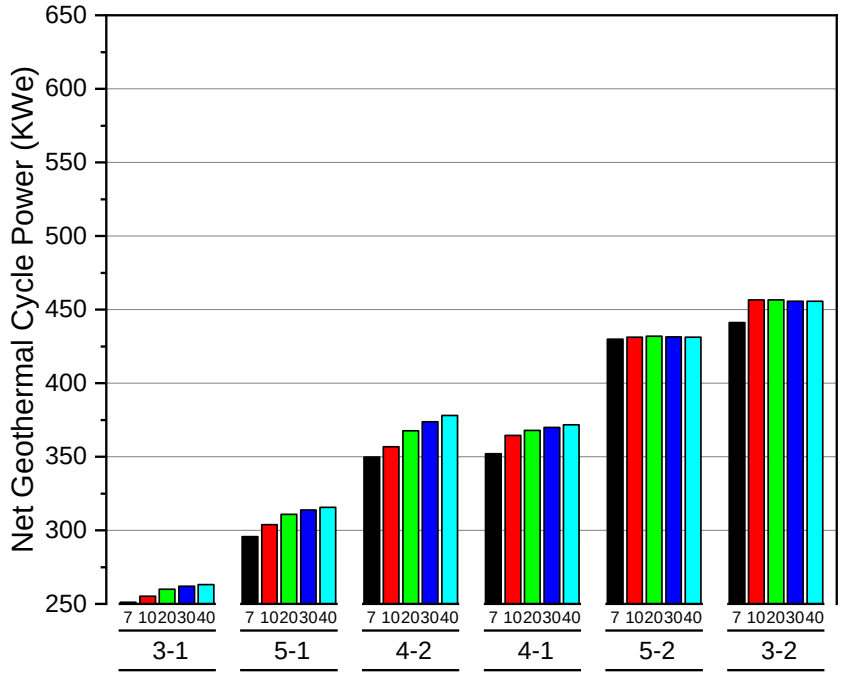

Figure 74 – Net Geothermal Cycle Power (KWe)

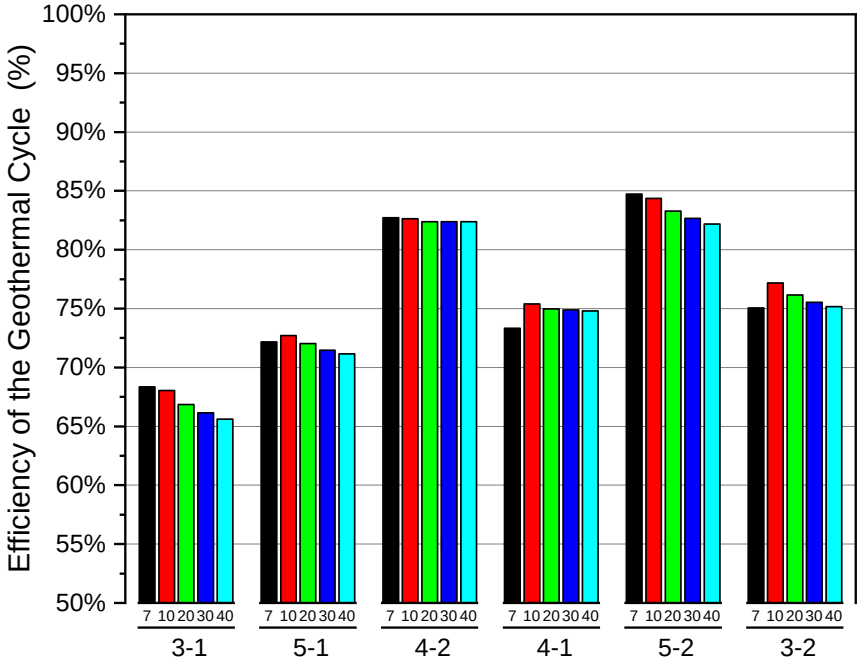

Figure 75 – Efficiency of the Geothermal Cycle (%)

8 Discussion

Is presented in Figure 74 the production and injection pattern of Case 3-2, the one which maximizes the net power of the geothermal cycle. This finding correlates with the fact that the combination of water flow rate and the higher temperature of the water in Well A improve the energy production. The magnitude of the result presented here can be considered as the most optimistic approach.
Figures 70a to 72b show the relative weight of the four main energy consumes in the geothermal cycle. In Figure 75 case 4-2 show the influence of the well pattern on the performance of the cycle. In this case pressure in Well A does not decrease excessively, whereas Well B experiences a free-flow effect. The presence of the Small-Fault acts as a shortcut from south to north. The faulted zone allows water to pass orthogonally through the natural fractures of the matrix. It cannot be identified any cold water channelization in this process, thus suggesting that this particular case is intersting at the noment of considering the energy cost to maintain the geothermal cycle running.
The reservoir modeling makes it possible to visualize how the pressure diffuses along the reservoir and how the wells between them interfere, see Figures 55 to 53. The streamlines show the low-velocity zones in which flow is stacked due to the interaction between wells, additionally to the presence of reservoir heterogeneities. All these interactions are the key factors that define the efficiency of the energy expended to enable the geothermal heat recovery. This is something that would be refined if there is a definite detailed heterogeneity analysis of the rock.

Recommendations

- Investigate the maximum flow which makes the production of geothermal energy profitable.

  If the water flow rate increases, the order of merit of the simulated scenarios could change, because the pressure losses due to fluid flowing increases exponentially.

- Perform two-phase simulations.

  It is very important to better understand the mixed gas-water production, which is the most prevalent production situation under real operative conditions.
  The mixing of water and gas could improve the production through a natural gas lift. High production rates can be achieved, at the same time produced gas could be sold.

- Consider the lateral variation of the petrophysical properties of the matrix.

  Type II (perpendicular to axis) fractures, are more dominant in the axis, and became less important in the flanks, where type I (parallel to the axis) dominates.
  A variation of the permeabilities configuration could create a more complex water flux pattern, that could also alter the energetic requirements for the geothermal cycle.

9 Conclusion and outlook

The Macueta field has been modeled as a middle-temperature geothermal reservoir to find the potential use of the hot water produced together with gas and condensate. The conversion of heat into usable energy to balance the energy requirement for gas compression has encouraged the O&G company PAE to support this thesis.
To ensure the profitability of geothermal energy production in the Macueta field, the main energy consumptions were identified in order to later search for an optimal production/injection scheme which minimizes the energy expenditures of the cycle.
Chapter 3 described the geological features of the folded and thrust belt and the detachment faults that configure the anticline in which the Macueta field is located. A compressive environment has configured a naturally fractured reservoir and a very thick cap-rock described in Chapter 4. Particularly in this Thesis, the "Small fault" has the property of allowing the flux along it, but with the restrictions imposed by its low permeability. In Chapter 5 a summary of the geological models from the Argentine and Bolivian side was done. The abnormally high productivity and WHT of Well A, in real operation conditions, departs greatly in comparison with the rest of the wells. Later, with support for a new seismic 3D interpretation of southern San Alberto Field on Bolivia's side, the Small Fault was sketched into the northern part of Macueta Field. With the open-source software MeshIt an optimized meshing procedure was performed, which ensures a high density of the calculation points in the reservoir interval, the three selected wells and the small Fault. In Chapter 6, the initial values of permeability in the reservoir and the small fault, have been calibrated to match the expected behavior observed during the Build-Up Test done in Well A. A temperature profile for the T-H model was calculated using real data of the thermal properties of the rock (Mud-log) and the heat flux density extracted from the work of Moretti et al. (1996). Later in Chapter 6.3, a sensitivity analysis of the meshing procedure helped to find the optimal model discretization that provides a compromise solution between computational time and accuracy. The Thermo_Hydraulical numerical modelization was carried out with the open-source OpenGeoSys software for water as a single-phase. To calibrate the model, historical gas and liquid production were converted to water, simulating the production effect until the time the well test was performed. In chapter 6.5 the Productivity Indexes and the Graphs of $\Delta\overline{Pr}$, ΔP_{wf}, $\Delta(\Delta P_{dd})$ vs time and $\frac{\delta\Delta\overline{Pr}}{\delta t}$ and $\frac{\delta\Delta P_{wf}}{\delta t}$ vs time, especially these last graphs provide a visual interpretation of the variation of energy expended along the productive lives of the wells. Finally, several scenarios have been simulated in this chapter, with the aim of finding the differences from the energetic point of view, when water is mobilized through the reservoir. The differences were quantified in Chapter 7, WellboreKIT code was used to calculate the heat and pressure losses in the borehole. The production of useful energy was calculated using GESI code. With the energetic calculus of the four main parts of the geothermal cycle, the ranking of the scenarios has shown their dependence on the proper choice of the well pattern. Each simulated scenario holds its own and distinctive energy consumption profile. However, profiles should change as the production rate increases. A right reservoir management should assure the selection of the most advantageous well pattern which makes feasible the geothermal energy production.

10 Acknowledgement

During the time I've been working on this thesis, I feel I've been training more than my geoscience skills. Organizational and temporal solutions were critical as it was also important to learn quickly the new software packages that I need. I know that the efforts were more than productive. It was a great opportunity to learn about these important tasks and tools before leaving the academic environment.

I must thank for the achievement of such amount of complex tasks to the expert guidance of my supervisors Dr. Jörg Meixner, Dr. Sebastian Held and Dr. Silvia Barredo. They were very precise every time I asked them for their suggestions. Besides my supervisors, I would like to express my sincere gratitude to Prof. Dr. Thomas Kohl for providing me advice, a place, and resources, to write my thesis in the Institut für Angewandte Geowissenschaften (AGW). It was an honor for me to share this chance with the "AGW Team".

My sincere thanks also go to Herr Prof. Dr. Martin Gabi and Frau Prof. Dr. Cecilia Smoglie, whose trust has helped me a great deal in achieving my goals in the time I spent on this Double Master.

I would like to thank Patricio Garcia Bes and the company he represents Pan American Energy (PAE) for his time and for helping me get the data I needed from Macueta Fields. To Mariela Bernedo (PAE) and Miguel Angel Navia (YPFB) who have helped me with the required data and answering all the questions I made to them.

I thank my colleague in AGW Fabian Limberger. We spent many hours at office, and I get from him a lot of support in different areas. I would also like to thank Dr. Carola Meller for her willingness to accept the topic I proposed, and for her support, when I started to take the first steps in my work.

Last but not least, I would like to thank my father Juan Anibal Sosa, my mother Miriam Massaro, my brothers and sister (Diego, Romina y Agustin). And of course, my girlfriend Maria Garcia, who shares with me the good and bad moments, I will never forget her support in difficult times.

References

Amengual, R. (2009). Estudio de aptitud ambiental, proyecto camino troncal en macueta. Technical report, Hi, Geo, Ma Estudios Ambientales.

BID (2011). Evaluación de sistemas de bombeo de agua. *Manual de eficiencia energética*, page 55. Banco Interamericano de Desarrollo.

Böttcher, N., Watanabe, N., and Kolditz, O. (2015). *OpenGeoSys Tutorial Basics of Heat Transport Processes in Geothermal Systems*. Helmholtz Centre of Environmental Research - UFZ, 6th edition. Page 14-16.

Cacace, M. and Blöcher, G. (2016). A software for three dimensional volumetric meshing of complex faulted reservoirs. *Environmental Earth Sciences*, 74:5191 – 5209.

Cohen, M. (2002). Caracterizacion del sistema de fracturas naturales de los campos san pedrito y macueta. *Revista Asociacion Geologica Argentina*, 60(4).

Colletta, B., Letouzey, J., Soares, J., and Specht, M. (1999). Detachment versus fault-propagation folding: insights from the sub-andean ranges of southern bolivia. *Thrust Tectonics Conference*, pages 106–109. Royal Holloway, University of London,.

communications with PAE, P. (2017). Registro de presion y temperatura de fondo. Macueta Norte field - 2009.

Di Pasquo, M. (2002). The crassispora kosankei cystoptychus azcuyi palynozone of the upper carboniferous tupambi formation, tarija basin, northern argentina. *Review of Palaeobotany and Palynology*, 118:47–76.

Diaz Martinez, E. (1996). Síntesis estratigráfica del carbonífero de bolivia. *Memorias del 12 congreso geologico de Bolivia*, 12:355–367.

Disalvo, A. & Villar, H. (1999). Los sistemas petroliferos del area oriental de la cuenca paleozoica noroeste, argentina. *IV congreso Exploracion y Desarrollo Hidrocarburos*, I(83-100).

Forero, G. and Caicedo, O. (2016). Análisis de alternativa de generación de energía para el campo payoa. page 29.

Girardi, A., Cohen, M., and E., K. (2002). Integrated multidicipline approach lead to a recent success in naturally fractured reservoir - the macueta experience. *SPE Gas Technology Symposium*. SPE-75944-MS.

Gonzalez, B. (1950). Algunos problemas geologicos de las sierras pampeanas. *Revista de la Asociacion Geologica Argentina*, 5(81-110).

Hernandez, R., Echevarria, L., Allmendinger, R., Reynolds, J., and Jordan, T. (2002). Las faja plegada y corrida subandina del noroeste argentino. secuencia de precrecimiento y crecimiento, geometria estructural y tiempo de evolucion de los andes. *V Congreso de Exploracon y Produccion de Hidrocarburos.* Actas digitales, trabajos tecnicos, Mar del Plata.

Huanca Pongo, J., Poma Mamani, E., Murillo del Castillo, V., Machaca Herrera, R., Valdez ramirez, L., and Navia Vargas, M. (2017). San alberto - itau field static model. YPFB-Corporacion.

Husson, L. and Moretti, I. (2002). Thermal regime of fold and thrust belts: an application to the bolivian sub andean zone. *Tectonophysics*, 345:253–280.

Iñigo, J. F. P. (2009). Structural model and fracture analyses for a major gas emplacement in devonian sandstones of the subandes. Master's thesis, University of Texas at Austin.

Inigo, J. F., Laubach, S. E., and Hooker, J. N. (2012). Fracture abundance and patterns in the subandean fold and thrust belt, devonian huamampampa formation petroleum reservoirs and outcrops, argentina and bolivia. *Marine and Petroleum Geology*, 35(1):201–218.

Isaac, B. (1988). Uplift of the central andean plateau and bending of the bolivia orocline. *Journal Geophysical Research*, 93:3211–3231.

Klein, G. (2003). Optimization of electric energy consumption in marginal california oilfields. pages 4–2.

Kley, J., Monaldi, C., and Salfity, J. (1999). Along-strike segmentation of the andean fore-land: Causes and consequences. *Tecnophysics*, 301:75–94.

Luquez, J., Hofmann, C., and Constantini, L. (2002). *Los Reservorios de las Formaciones Santa Rosa, Icla y Huamampampa. En Rocas Reservorio de las Cuencas Productivas de la Argentina .* 50 Congreso de Exploracion y Desarrollo de Hidrocarburos. page 683-697.

Marshall, L. G. and Sempere, T. (1991). The eocene to pleistocene vertebrates of bolivia and their stratigraphic context: a review. fosiles y facies de bolivia. *Revista Tecnica de YPFB*, 12:631–652.

MinEM (2017). Volumenes de hidrocarburos_reportes graficos. Ministerio de Energía y Minería.

Moretti, I., Baby, P., Mendez, E., and Zubieta, D. (1996). Hydrocarbon generation in relation to thrusting in the sub andean zone from 18 to 22grads, bolivia. *Petroleum Geosciencies*, 2:17–28.

Moretti, I., Labaume, P., Sheppard, S. M., and Boulegue, J. (2002). Compartmentalisation of fluid flow by thrust faults, sub-andean zone, bolivia. *Tectonophysics*, 348:5–24.

Navia Vargas, M. A. (2017). Personal communication.

Nusiaputra, Y. Y. (2017). *Coupled Hydraulic, Thermal and Chemical Simulations for Geothermal Installations*. phdthesis, Bauingenieur, Geo und Umweltwissenschaften des Karlsruher Instituts fur Technologie (KIT).

Pesce, A. (2015). Argentina country update. *Segemar*.

Ramos, V. & Folgeras, A. (2009). Andean flat-slab subduction through time. *Laboratorio de Tecto´nica Andina, Universidad de Buenos Aires – CONICET*.

Ramos, V. (1999). Los depositos sinorogenicos terciarios de la region andina. *Geologia Argentina, Instituto de Geologia y Recursos Minerales*, 29(22):651–682.

Rebay, G., Barrenechea, J., Requena, E., and Rocha, A. (2001). San alberto and san antonio. two new gas and condensate giant fields in bolivia. *Petrobras*, pages 37–49.

Rodgers, J. (1971). The taconic orogeny. *Geological Society of America*, 5:1141–1178.

Starck, D. (1995). Silurian-jurassic stratigraphy and basin evolution of northwestern argentina. *Petroleum Basins of South America.*, 62:251–268.

Starck, D., Constantini, L., and Schulz, A. (2002). Analisis de algunos aspectos geometricos y evolutivos de las estructuras de la faja plegada subandina del norte de argentina y sur de bolivia. *INGEPET 2002 (EXPR-3-DS-40)*.

Starck, D., Gallardo, E., and Schulz, A. (1992). La discordancia precarbonica en la porcion argentina de la cuenca de tarija. *Boletin de Informaciones Petroleras*, 30(3):2–11.

Suarez Soruco, R. and Diaz Martinez, E. (1996). Lexico estratigrafico de bolivia. *Revista Tecnica YPFB*, page 227. Cochabamba.

Vetter, C. (2011). Parameterstudie zur simulation von niedertemperatur kreisprozessen. *KIT SCIENTIFIC REPORTS 7585*.

Vetter, C. (2014). Thermodynamische auslegung und transiente simulation eines überkritischen organic rankine cycles für einen leistungsoptimierten betrieb. *KIT SCIENTIFIC REPORTS 7674*, page 52.

Vistalli, M. (1999). Cuenca siluro-devonica. *Congreso Geologico Argentino*, 14:168–184.

Appendix

A Thermal conductivities

Thermal conductivities in Table 16 have been taken from the available literature. These averaged thermal conductivities were calculated taking into account the percentage of different rock types described in each interval. Finally, the geometric-mean model was used to correct the average thermal conductivities due to the presence of interstitial water in the poral space.
The average thermal conductivity of each formation (right side of Table 16) was used to perform the simulation. Values below the bottom of the hole were taken from the related bibliography.

Lithology	Thermal Cond.	Units	Formation	Porosity	Units
Shale	1.4	W/m.K	Weathering zone	0.20	m^3/m^3
Claystone	1.6	W/m.K	Las Peñas	0.15	m^3/m^3
Reddish claystone	1.6	W/m.K	Tarija	0.15	m^3/m^3
Mudstone	1.4	W/m.K	Tupumbi	0.15	m^3/m^3
Silty-Claystone	2.09	W/m.K	Iquiri	0.15	m^3/m^3
Reddish Silty-Claystone	2.09	W/m.K	Los Monos	0.1	m^3/m^3
Siltstone	2.3	W/m.K	Huamampampa	0.03	m^3/m^3
Reddish Siltstone	2.3	W/m.K	Icla	0.03	m^3/m^3
Sandy Siltstone	2.66	W/m.K	Santa Rosa	0.03	m^3/m^3
Sanstone	3.5	W/m.K	Baritu	0.02	m^3/m^3
Mecaceus Sandstone	3.17	W/m.K	Lipeon	0.01	m^3/m^3
Coarse sandstone	3.17	W/m.K	Zapla	0.01	m^3/m^3
Conglomerate	2.9	W/m.K			
Diamictite	3.3	W/m.K			
Reddish diamictite	3.3	W/m.K			
Quartcite	4.4	W/m.K			

Table 16 – Thermal conductivities and porosities of the rocks in the borehole.

B Reservoir fluids properties and Build-Up Test

Reservoir fluids were characterized. PVT data is presented in the following Table.

PVT Data

Reservoir fluids have been characterized in laboratory.

Fluid Properties		Units	Reservoir param.		Units
Gas gravity	0.5523	sp. gravity	Reservoir press.	40	MPa
Condensate to gas ratio	0.00022	m^3/m^3	Reservoir temp.	135	℃
Condensate gravity	0.82507	rel.density			
Water to gas ratio	0.000155	m^3/m^3	Phase	FVF	Units
Water salinity	220000	ppm	Water	1.0565	m^3/m^3
			Condensate	1.5137	m^3/m^3
			Gas	0.0043	m^3/m^3

Table 17 – PVT data and reservoir parameters used for calculations.

Well Test data

A well test was done in Well A (Mac.x-1001 bis). This well was stabilized at a constant flow rate of 2.0 Mm3/d during 28 hours, then the dynamic gradient was measured. In the Stop Condition, the well was for 60 hours stopped, afterward the static gradient was measured.

Production Conditions						Stop Conditions					
Depth		Press.		Temp.		Depth		Press.		Temp.	
-50	m	22.304	MPa	100.30	℃	-5090	m	37.864	MPa	135.23	℃
-1500	m	25.403	MPa	113.63	℃	-5050	m	37.795	MPa	134.48	℃
-3000	m	28.721	MPa	124.49	℃	-5000	m	37.685	MPa	133.79	℃
-4500	m	31.964	MPa	132.62	℃	-4900	m	37.468	MPa	132.21	℃
-4700	m	32.517	MPa	133.60	℃	-4700	m	37.052	MPa	129.65	℃
-4900	m	33.373	MPa	134.78	℃	-4500	m	36.650	MPa	126.30	℃
-5090	m	34.461	MPa	135.86	℃	-4000	m	35.596	MPa	119.76	℃
						-3000	m	33.384	MPa	105.91	℃
						-2000	m	31.138	MPa	92.68	℃
						-1000	m	28.830	MPa	63.91	℃
						-50	m	26.560	MPa	41.81	℃

Table 18 – Well Test data _ Pressure and Temperature.

C WellboreKIT

The WellboreKIT code calculates the thermal, hydraulic and chemical (THC) behaviour during the (de-) pressurization of a two-phase (aqueous and non-aqueous) multi-component geothermal system in deep wells. It is a reactive wellbore simulator established in collaboration with European Institute for Energy Research (EIFER). The code is developed in coupled Elmer-Python-PHREEQC open-source platform and can simulate transient mass flow, pressure, temperature, and chemical species concentration and saturation profile. A sequential coupling between transport and (de-) compression with heat transfer of geothermal fluid-rock

formation is implemented by using operator splitting method. For more detailed information about WellboreKIT, the Phd. dissertation of (Nusiaputra, 2017) can be consulted.

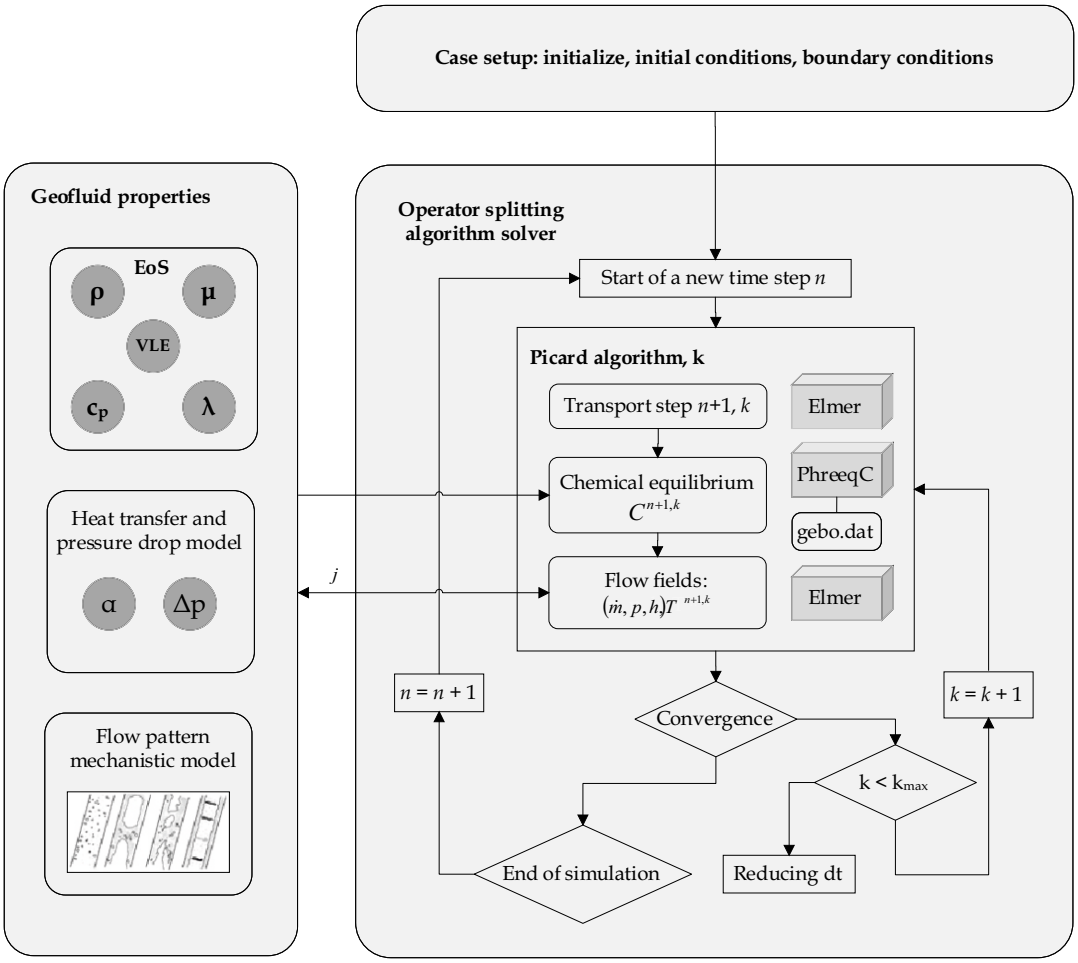

Figure 76 – WellboreKIT Numerical procedure calculation

D GESI

The GESI code is used to model and simulate ORC and Kalina power plant processes with a geothermal heat source. This software optimizes a thermodynamic processes according to the selected state of the fluid and vapour parameters at the entrance point of the cycle.
The program make calculations over a cycle like the one sketched in Figure 78b, the results are the integral quantities that describe the system thermodynamically. They serve to classify and compare various circuit components, working fluids or boundary conditions. For more detailed information about GESI, the work of (Vetter, 2011) can be consulted. The calculation process for the heat exchanger is shown in Figure 77.

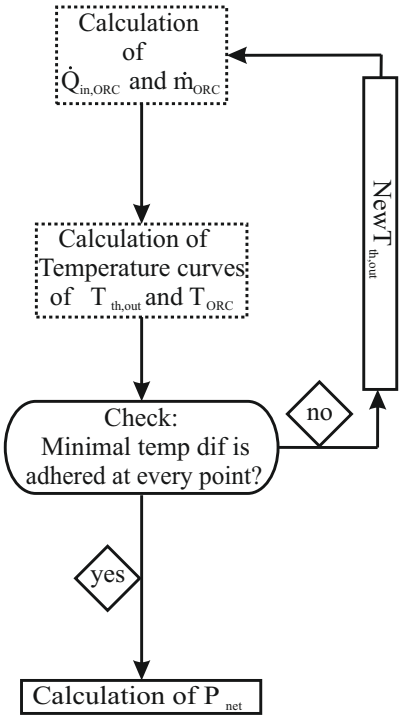

Figure 77 – Iterative pattern for the heat exchanger (Vetter, 2011)

Parameters used to set the calculation in GESI are presented here. For simplicity, in the present thesis was considered an air-cooled ORC without regenerator. The working fluid as it was mentioned is Propane. This fluid allows real efficiencies of conversion in the order of 9% to 11% which are concordant with the results obtained by Vetter (2014)(page 52).

Overview of the boundary conditions of the simulations performed

In Table 20 the needed parameters to run a simulation with GESI are listed.
The environmental characteristic of Macueta field has been provided by the Macueta Field operator Pan-American Energy. Table 19.

	J	F	M	M	J	J	A	S	O	N	D	avg.
Temp avg.(℃)	22,8	22,1	21,1	18,5	13,3	13,0	14,7	17,0	20,3	21,5	22,5	18,6
Rel Hum.(%)	76,8	76,4	80,9	83,8	81,2	73,7	64,2	55,6	56,6	64,2	71,3	72,3
Wind (Km/h)	5,79	5,83	4,97	4,53	4,33	5,26	6,81	8,73	9,25	8,23	6,03	6,17

Table 19 – Environmental conditions of Macueta Field.

ORC-Process			**Cooling Air**		
Temperature of Condensation	30	℃	Inlet Temperature*	20	℃
Eficiency of the Pump _ η_{Pump}	0.7		Inlet Pressure	0.1013	MPa
Efficiency of the Turbine_ η_{Pump}	0.8		Relative Humidity	65	%
Min. Permissible Steam Cont.	0.9	%			
Geothermal Water			**Condensator**		
Inlet Temperature*, WHT	121.5-136.5	℃	$\Delta T_{\text{min}} Air, in$	5	K
Inlet Pressure, WHP	2.5	MPa	Pressure drop	0.02	MPa
Mass Flow*	10 or 20	kg/s			
Heat Exchanger					
$\Delta T_{\text{min}} Water, in$	10	K			
Pressure Drop	0.02	MPa	*Case dependant.		

Table 20 – Boundary conditions of the ORC Process and operating parameters.

ORC-Process Diagram

	Pres. [MPa]	Temp. [℃]	Enthalpy [KJ/Kg]	Entropy [KJ/KgK]	Dens. [Kg/m^3]	Quality
1	1.079	30	-362.47	-2.04	484.39	0
2s	4.02	32.23	-356.43	-2.04	490.27	Liquid
2	4.02	33.19	-353.85	-2.03	488.79	Liquid
3	4	100	12.91	-0.99	105.73	Vapor
4s	1.099	30.74	-41.93	-0.99	24.39	0.97896
4	1.099	32.71	-30.96	-0.95	23.59	Vapor

Table 21 – Working fluid cycle in the ORC process.

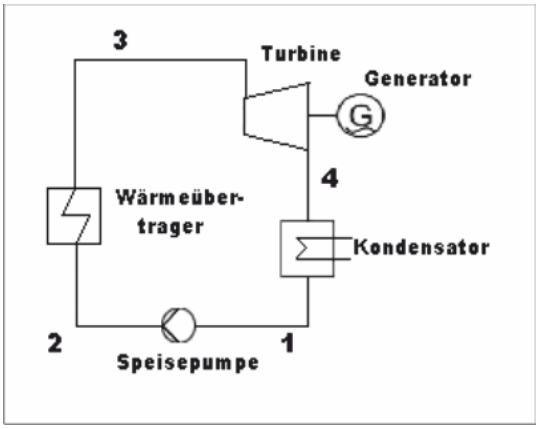

(a) Sketch of the ORG with out Regenerator.

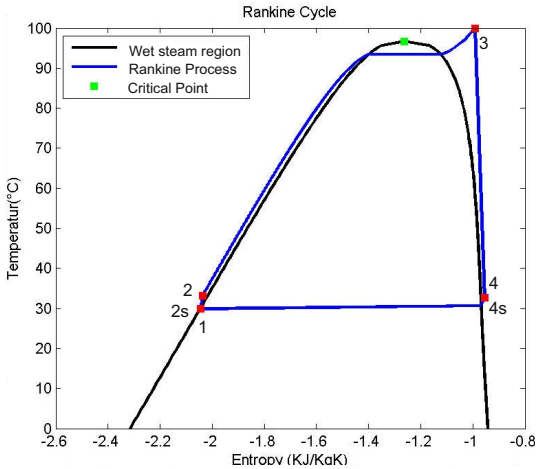

(b) Rankine process with Propane as working fluid.

Figure 78 – ORC component layout (a) and Temperature-entropy (T-s) diagram (b)